

AD-A040 683

ILLINOIS UNIV AT URBANA-CHAMPAIGN COORDINATED SCIENCE LAB F/G 20/12  
PROPERTIES OF SILICON IMPLANTED WITH ARSENIC THROUGH SILICON DI--ETC(U)  
JAN 77 D R MYERS  
R-756

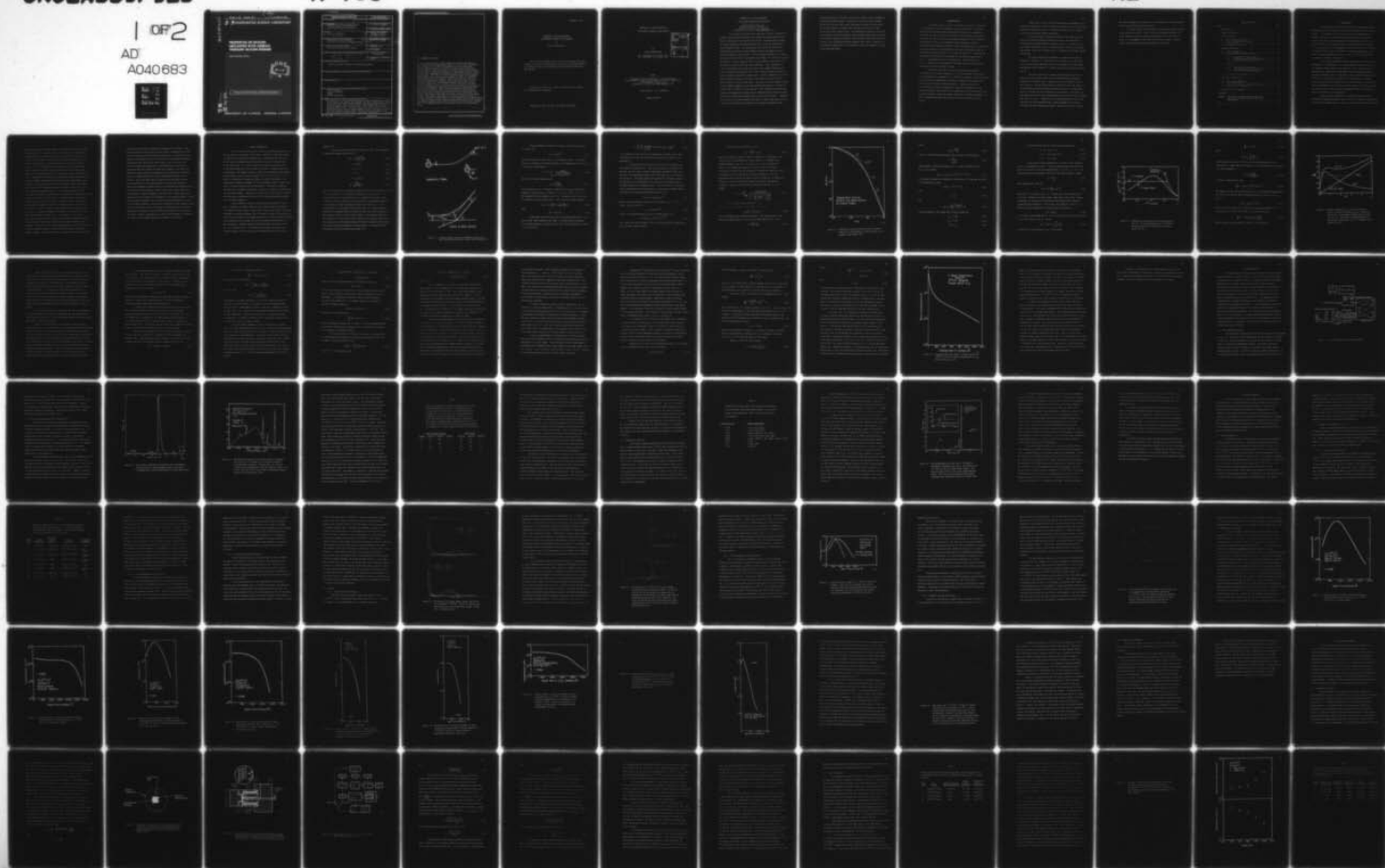
DAAB07-72-C-0259

NL

UNCLASSIFIED

1 OF 2


AD  
A040683



ADA 040683

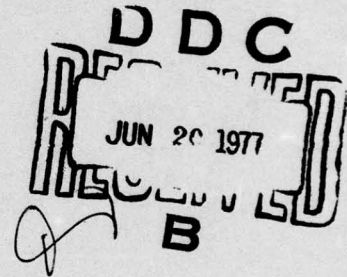
REPORT R-756 JANUARY, 1977

UILU-ENG 77-2203

 **COORDINATED SCIENCE LABORATORY**

# PROPERTIES OF SILICON IMPLANTED WITH ARSENIC THROUGH SILICON DIOXIDE

DAVID RICHARD MYERS



APPROVED FOR PUBLIC RELEASE. DISTRIBUTION UNLIMITED.

AD No. \_\_\_\_\_  
DDC FILE COPY

UNIVERSITY OF ILLINOIS - URBANA, ILLINOIS



UNCLASSIFIED

SECURITY CLASSIFICATION OF THIS PAGE (When Data Entered)

| REPORT DOCUMENTATION PAGE  |                       | READ INSTRUCTIONS<br>BEFORE COMPLETING FORM  |
|--|-----------------------|--|
| 1. REPORT NUMBER   | 2. GOVT ACCESSION NO. | 3. RECIPIENT'S CATALOG NUMBER  |
| 4. TITLE (and Subtitle)<br>(6) PROPERTIES OF SILICON IMPLANTED WITH<br>ARSENIC THROUGH SILICON DIOXIDE   |                       | 5. TYPE OF REPORT & PERIOD COVERED<br>(7) Technical Report                                     |
| 7. AUTHOR(s)<br>(10) David Richard Myers   |                       | 6. PERFORMING ORG. REPORT NUMBER<br>R-756, UILL-ENG-77-2203                                    |
| 9. PERFORMING ORGANIZATION NAME AND ADDRESS<br>Coordinated Science Laboratory<br>University of Illinois at Urbana-Champaign  |                       | 8. CONTRACT OR GRANT NUMBER(s)<br>(15) DAAR-07-72-C-0259,<br>NSF-DMR-73-02359                  |
| 11. CONTROLLING OFFICE NAME AND ADDRESS<br>Joint Services Electronics Program  |                       | 10. PROGRAM ELEMENT, PROJECT, TASK<br>AREA & WORK UNIT NUMBERS<br>(14) R-756, UILL-ENG-77-2243 |
| 14. MONITORING AGENCY NAME & ADDRESS (if different from Controlling Office)<br>(12) 149 P. (11) Jan 77   |                       | 12. REPORT DATE<br>January, 1977   |
|  |                       | 13. NUMBER OF PAGES<br>138   |
|  |                       | 15. SECURITY CLASS. (of this report)<br>UNCLASSIFIED   |
|  |                       | 15a. DECLASSIFICATION/DOWNGRADING<br>SCHEDULE  |
| 16. DISTRIBUTION STATEMENT (of this Report)<br><br>Approved for public release; distribution unlimited   |                       |  |
| 17. DISTRIBUTION STATEMENT (of the abstract entered in Block 20, if different from Report)   |                       |  |
| 18. SUPPLEMENTARY NOTES  |                       |  |
| 19. KEY WORDS (Continue on reverse side if necessary and identify by block number)<br>Ion Implantation<br>Arsenic in Silicon<br>Damage<br>Recoil Implantation  |                       |  |
| 20. ABSTRACT (Continue on reverse side if necessary and identify by block number)<br>The properties of silicon after annealing of arsenic implantations through silicon dioxide are studied, and compared with those resulting from arsenic implantations into bare silicon surfaces. Photoluminescence studies of radiation damaged silicon establish the 0.970 eV peak as arising from a carbon-dependent center. The same studies also confirm that the 0.790 eV luminescence arises from an oxygen dependent center, and suggest that this center may depend on carbon as well. With the oxygen dependence of the center responsible for the 0.790 eV luminescence established, it is possible |                       |  |

DD FORM 1 JAN 73 1473 EDITION OF 1 NOV 65 IS OBSOLETE

UNCLASSIFIED

SECURITY CLASSIFICATION OF THIS PAGE (When Data Entered)

097 700

## 20. ABSTRACT (continued)

to monitor the presence of excess oxygen in silicon by the presence of this peak in the recombination spectra of silicon after irradiation. Thus, observation of 0.790 eV luminescence from float zone grown silicon samples implanted with arsenic through silicon dioxide, and not from identical samples in which the silicon dioxide was chemically removed prior to arsenic implantation, is interpreted as direct evidence for the recoil implantation of oxygen into the silicon from the silicon dioxide layer. The effect of recoil-implanted oxygen on the transport properties of silicon implanted with arsenic to fluences of  $10^{15}\text{cm}^{-2}$  and  $5 \times 10^{15}\text{cm}^{-2}$  is then examined. Sheet resistivity and sheet Hall coefficient measurements following various annealing stages indicate identical recovery for through-oxide implants and for bare surface implants. Comparison of the impurity profiles obtained by secondary ion mass spectroscopy with free carrier profiles obtained by differential Hall effect measurements shows identical activation for through oxide and bare surface arsenic implants for both 600°C and 1000°C anneals. Additionally, mobility profiles obtained during the differential Hall effect measurements indicate mobility values for the bare surface and through oxide implants that agree with values expected for arsenic doped silicon. Measurements obtained in this study are consistent with the interpretation that residual damage seen for through oxide implanted samples is caused by random nucleation during the recrystallization of the implantation-induced amorphous layer, due to a reduction in the epitaxial regrowth rate of the implanted layer by the presence of excess recoil-implanted oxygen.

50 to the 15th power/sq cm

10 to the 15th power/sq cm

PROPERTIES OF SILICON IMPLANTED  
WITH ARSENIC THROUGH SILICON DIOXIDE

by

David Richard Myers

This work was supported in part by the Joint Services Electronics Program (U.S. Army, U.S. Navy and U.S. Air Force) under Contract DAAB-07-72-C-0259 and in part by the National Science Foundation under Grant DMR 73-02359.

Reproduction in whole or in part is permitted for any purpose of the United States Government.

Approved for public release. Distribution unlimited.

PROPERTIES OF SILICON IMPLANTED  
WITH ARSENIC THROUGH SILICON DIOXIDE

BY

DAVID RICHARD MYERS

B.S., University of Illinois, 1971  
M.S., University of Illinois, 1973

|                                 |   |
|---------------------------------|---|
| ACCESSION for                   |   |
| RTIS                            | White Section <input checked="" type="checkbox"/> |
| BDC                             | Buff Section <input type="checkbox"/>             |
| UNANNOUNCED                     | <input type="checkbox"/>                          |
| JUSTIFICATION                   |   |
| BY                              |   |
| DISTRIBUTION/AVAILABILITY CODES |   |
| Dist.                           | AVAIL. SUB. or SPECIAL                            |
| A                               |   |

THESIS

Submitted in partial fulfillment of the requirements  
for the degree of Doctor of Philosophy in Electrical Engineering  
in the Graduate College of the  
University of Illinois at Urbana-Champaign, 1977

Thesis Advisor: B. G. Streetman

Urbana, Illinois

PROPERTIES OF SILICON IMPLANTED  
WITH ARSENIC THROUGH SILICON DIOXIDE

David Richard Myers, Ph.D.  
Coordinated Science Laboratory and  
Department of Electrical Engineering  
University of Illinois at Urbana-Champaign, 1977

The properties of silicon after annealing of arsenic implantations through silicon dioxide are studied, and compared with those resulting from arsenic implantations into bare silicon surfaces. Photoluminescence studies of radiation damaged silicon establish the 0.970 eV peak as arising from a carbon-dependent center. The same studies also confirm that the 0.790 eV luminescence arises from an oxygen dependent center, and suggest that this center may depend on carbon as well. With the oxygen dependence of the center responsible for the 0.790 eV luminescence established, it is possible to monitor the presence of excess oxygen in silicon by the presence of this peak in the recombination spectra of silicon after irradiation. Thus, observation of 0.790 eV luminescence from float zone grown silicon samples implanted with arsenic through silicon dioxide, and not from identical samples in which the silicon dioxide was chemically removed prior to arsenic implantation, is interpreted as direct evidence for the recoil implantation of oxygen into the silicon from the silicon dioxide layer. The effect of recoil-implanted oxygen on the transport properties of silicon implanted with arsenic to fluences of  $10^{15} \text{ cm}^{-2}$  and  $5 \times 10^{15} \text{ cm}^{-2}$  is then examined. Sheet resistivity and sheet Hall coefficient measurements following various annealing stages indicate identical recovery for through-oxide implants and for bare surface implants. Comparison of the impurity profiles obtained by secondary ion mass spectroscopy with free carrier profiles obtained by differential Hall effect measurements shows



identical activation for through oxide and bare surface arsenic implants for both 600°C and 1000°C anneals. Additionally, mobility profiles obtained during the differential Hall effect measurements indicate mobility values for the bare surface and through oxide implants that agree with values expected for arsenic doped silicon. The measurements obtained in this study are consistent with the interpretation that residual damage seen for through oxide implanted samples is caused by random nucleation during the recrystallization of the implantation-induced amorphous layer, due to a reduction in the epitaxial regrowth rate of the implanted layer by the presence of excess recoil-implanted oxygen.

## ACKNOWLEDGEMENTS

The author wishes to express his deepest appreciation to Professor B. G. Streetman for his encouragement, support, and guidance. The author appreciates the foresight shown by Professor Streetman in the suggestion of this topic for study, as well as his efforts in facilitating its completion. Thanks are also due to all the past and present members of the Semiconductor Physics group at the at the Coordinated Science Laboratory for their cooperation and friendship, especially to Drs. John Noonan and C. G. Kirkpatrick for their expertise in photoluminescence and electron irradiations and for many helpful discussions; to Dr. P. K. Chatterjee and Mr. W. V. McLevige for the design and construction of the double a-c van der Pauw system; and to Dr. K. V. Vaidyanathan for useful conversations. Special thanks go to Mr. G. T. Marcyk for his measurement of the GDOS profiles, for many useful discussions, and for his sense of humor.

The author would like to express his deepest appreciation to Dr. Pradeep Shah of Texas Instruments, Inc. for his interest in this project, for his assistance in arranging the  $5 \times 10^{15} \text{ cm}^{-2}$  As implants at Texas Instruments, and for many useful suggestions, especially in regard to the examination of impurity redistribution by thermal oxidation. Thanks also are due to Dr. S. Watelski of Texas Instruments for sharing his knowledge of silicon etching techniques, particularly for his suggestion of the silicon planar etch. The author wishes to extend his deepest appreciation to Texas Instruments, Inc., whose invaluable assistance made possible the timely realization of this project.

Thanks to Mr. T. Leedy of the National Bureau of Standards for the ellipsometry measurements and for sharing his expertise in silicon processing. Additional thanks must go to Dr. K. Galloway of the NBS for his interest in the project and for many helpful discussions.

The author wishes to express his thanks to the Surface Analysis Group at the Materials Research Laboratory for their time and effort in developing the elemental profiles, especially to Dr. C. A. Evans, Jr. for his interest and advice; to Dr. P. Williams and Mr. V. DeLine for the SIMS measurements, and to Mr. W. Wadlin and Mr. R. Blattner for the Auger electron spectroscopy.

The author expresses his gratitude for useful discussions with Professor N. Holonyak, Jr. Thanks are due to Professor J. E. Greene and Mr. L. Wu for allowing the author access to the Dektak for the step height measurements, and to Professor G. Stillman for access to his deionized water supply.

The author would like to express his appreciation for the help given him by the technical staff of the Coordinated Science Laboratory throughout his graduate career. Thanks are due to the members of the CSL Machine Shop, to the CSL Electronics Shop, especially to Mr. Tom Casale for his invaluable assistance and unfailing good cheer, and to R. MacFarlane and Ms. G. Shuttke for their drafting skill and patience. The author also appreciates the efficiency and understanding of the CSL Photo Shop, especially that of Mr. R. Gladin. Thanks are due to the administrative staff of CSL, especially Mrs. Rose Schmidt and Mrs. Barbara Champagne, for helping to anticipate and avoid procedural problems. The author would like to thank

Mrs. Trudy Williams for her efficiency in the preparation of this manuscript, and for her good humor and unfailing calm.

The author wishes to acknowledge the loving moral support provided by his family and in-laws. Finally, and of the greatest importance, the author wishes to express his deepest appreciation for his wife, Janice; whose love, encouragement, and concern were constant sources of support during the most difficult and trying portions of this work.

## TABLE OF CONTENTS

| CHAPTERS   | Page |
|--|------|
| 1. INTRODUCTION.....   | 1    |
| 2. RECOIL IMPLANTATION.....  | 4    |
| 3. PHOTOLUMINESCENCE.....  | 28   |
| 3.1. Photoluminescence System.....   | 28   |
| 3.2. Silicon Luminescence and Defect<br>Identification.....  | 30   |
| 3.3. Oxygen Recoil Detection.....  | 36   |
| 4. ELEMENTAL PROFILING.....  | 42   |
| 4.1. Sample Preparation.....   | 42   |
| 4.2. Techniques for Elemental Profiling.....   | 43   |
| 4.2.1. Auger Electron Spectroscopy.....  | 43   |
| 4.2.2. Glow Discharge Optical Spectroscopy.....  | 45   |
| 4.2.3. Secondary Ion Mass Spectroscopy.....  | 46   |
| 4.3. Results.....  | 47   |
| 4.3.1. Auger Electron Spectroscopy.....  | 47   |
| 4.3.2. Glow Discharge Optical Spectroscopy.....  | 51   |
| 4.3.3. Secondary Ion Mass Spectroscopy.....  | 53   |
| 4.4. Comparison of Techniques.....   | 69   |
| 5. ELECTRICAL MEASUREMENTS.....  | 71   |
| 5.1. Experimental Procedure.....   | 71   |
| 5.2. Sheet Measurements.....   | 79   |
| 5.3. Carrier Concentration and Mobility Profiles.....  | 86   |
| 5.4. Discussion of Uncertainties.....  | 105  |
| 6. DISCUSSION AND CONCLUSIONS.....   | 116  |
| REFERENCES.....  | 125  |
| APPENDIX: Evaluation of Carrier Concentrations and<br>Mobilities through Differential Hall Effect<br>Measurements..... | 132  |
| VITA.....  | 138  |



## 1. INTRODUCTION

Ion implantation has evolved from an area of specialized research investigations into a technique routinely used throughout the semiconductor industry. Ion implantation as a process tool has many advantages over diffusion technology, including more accurate doping control and better lateral registration, lower temperature processing, better control of the depth and profile of the dopant impurities, and the potential for novel device structures [1,2]. The implantation dose can be accurately controlled from about  $10^{16} \text{ cm}^{-2}$ , which is equivalent in impurity concentration to the heaviest diffused predeposition, down to a dose of  $10^{11} \text{ cm}^{-2}$ , which has no counterpart in diffusion technology [2].

Silicon device technology provides an excellent illustration of the advantages of ion implantation. For many applications, arsenic would be a more desirable dopant impurity than phosphorus, due in large part to its lower diffusion coefficient [3], and hence lesser redistribution during subsequent processing steps. Unfortunately, arsenic diffusion technology is difficult [2], while arsenic implantation is fairly simple. High-dose arsenic implantations are commonly used to form buried layers, emitters for bipolar transistors, and for doping of contact regions [1,2], making arsenic the donor impurity of choice for many applications which were unrealistic prior to the advent of ion implantation.

Despite its many advantages, ion implantation would not have achieved its widespread popularity were it not for its excellent compatibility with the silicon planar process. The use of silicon dioxide layers for surface

passivation and selective area masking is an essential part of the silicon planar process [1]. Therefore, the discovery that arsenic implantations through the edges of tapered oxide layers lead to densely packed defect structures which cannot be removed by high temperature annealing [4] is a matter of great concern. In the experiment that led to this discovery, fluences of  $10^{15}$  to  $10^{16} \text{As}^+/\text{cm}^2$  were implanted into silicon substrates partially masked by islands of tapered oxide, and then the samples were annealed for 30 minutes at  $1000^\circ \text{C}$  to simulate the growth of an epitaxial layer. Examination of the samples by transmission electron microscopy then revealed a stable, high defect density region at the tapered edges of the oxide mask. Significantly, the annealing temperature used is considerably higher than the  $600^\circ \text{C}$  annealing normally required to restore the crystallinity of heavily implanted layers [1]. In the same study it was also discovered that identical disorder could be reproduced by implantations through uniformly thin oxides. In both cases, no residual damage could be seen in regions from which the silicon dioxide was removed prior to implantation. Because identical damage was seen for uniformly thin oxide layers, stress effects at the interface between the bare surface and the oxide edge could be ruled out. Instead, the damage was produced by the penetration of the arsenic beam through the oxide layer. As the arsenic ions penetrate the silicon dioxide layer, they suffer collisions with oxygen atoms and thus could potentially knock large concentrations of oxygen into the silicon substrate. This aspect of the problem was examined by Chu and co-workers [5] using the technique of helium ion backscattering to measure the extent of residual disorder. They discovered that implantations of arsenic and oxygen

into bare silicon surfaces reproduced the damage seen from arsenic implantations through thin oxide layers, and that arsenic implantations into bare silicon surfaces also lead to residual disorder [6]. The problem was later examined by transmission electron microscopy [7], which showed that arsenic implantations into bare silicon produced general lattice disorder, but that this disorder was significantly less and defects were more widely spaced than when both arsenic and oxygen were implanted. This study also showed that arsenic and oxygen implantations into bare silicon yielded the same type of damage as seen from arsenic implantations through silicon dioxide. Thus, while these results implicate recoiling oxygen atoms as being responsible for the residual damage, it has not been possible to identify the presence of oxygen recoils in the through-oxide implanted layers. While arsenic has been found to interact strongly with oxygen impurities in the annealing of radiation-damaged silicon [8], none of these studies have examined the role of arsenic in the formation of the residual defects. Finally, and of greatest importance, none of these studies have examined the effects of these residual defects on the electrical properties of the implanted layers. The aim of the present work is to examine the problems created by through-oxide arsenic implantation, and to contrast the properties of these layers with those of arsenic implantations into bare silicon surfaces, to determine the causes of this residual damage and the extent of its effects.

## 2. RECOIL IMPLANTATION

Much of the work reported here involves the interactions that occur when an energetic ion strikes a solid target. Analysis of these events leads to predictions of the depth an energetic ion will penetrate into the solid, and the extent of damage created by transfer of the ion's incident energy to the target atoms. It is also possible to estimate the energy and flux of recoiling target atoms, and to predict the erosion of target surfaces due to sputtering. This chapter provides a review of the assumptions and approximations needed to describe these processes, with specific application to the case of As implantation through  $\text{SiO}_2$  layers into silicon substrates. The comprehensive treatment by Sigmund [9] of the Lindhard, Scharff, Schiøtt (LSS) theory [10] forms the basis for this description. The theory is presently incomplete and is somewhat controversial, especially in regard to implantations into multilayer targets. Therefore our aim here will be to describe in general terms the physical mechanisms that occur and to develop reasonable estimates of ion and recoil behavior.

As an incident ion strikes a solid target and eventually comes to rest, it deposits its kinetic energy into the target through two mechanisms: 1) transfer of kinetic energy to target atoms in essentially elastic collisions (referred to as nuclear stopping); and 2) transfer of energy in the excitation of the orbital electrons of the target atoms, ions, or both (electronic stopping). These mechanisms occur simultaneously but are treated as being distinct for ease in analysis. Nuclear stopping, being conceptually the simpler of the two, will be treated first. We consider the ion-target collision as the classical problem of the ion's motion in the central field of the ion-atom

potential [9].

For the case of the target atom initially at rest, the conservation of energy and momentum require [11,12]

$$\tan \phi' = \frac{M_2 \sin \theta}{M_1 + M_2 \sin \theta} \quad (2.1)$$

$$\phi'' = \frac{\pi - \theta}{2} \quad (2.2)$$

$$E' = E - T \quad (2.3)$$

$$E'' = T \quad (2.4)$$

$$T = T_m \sin^2 \frac{\theta}{2} \quad (2.5)$$

$$T_m = \frac{4M_1 M_2}{(M_1 + M_2)^2} E \quad (2.6)$$

where  $M_1$  is the mass of the incident ion and  $M_2$  is the target atom mass;  $E$  is the ion's initial energy;  $T$  is the energy transferred in the collision;  $\phi'$  is the scattered angle of the projectile in the laboratory system with energy  $E'$  after the collision; and  $\phi''$  is the angle taken by the scattered particle in the laboratory system with energy  $E''$  after the collision, with  $\theta$  the scattering angle in the center of mass system (Fig. 2.1). Here electronic excitation is considered only as a source of energy loss, and is assumed to have negligible effect on the collision dynamics. The experience from ion-gas collisions in the keV region [13] is that electronic energy loss amounts to only a few percent of the energy transfer and thus is assumed to have a negligible effect on either the amount of energy transfer or the post-collision trajectories of the ion and recoiling target atom.



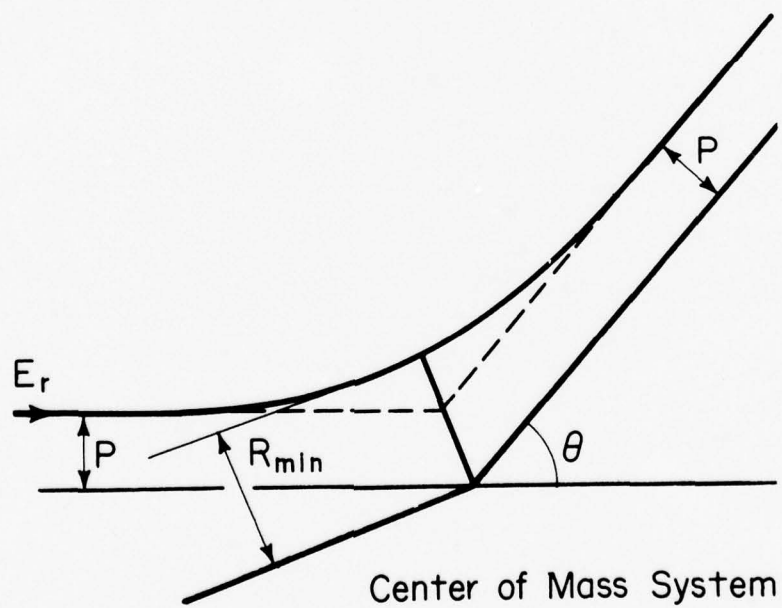
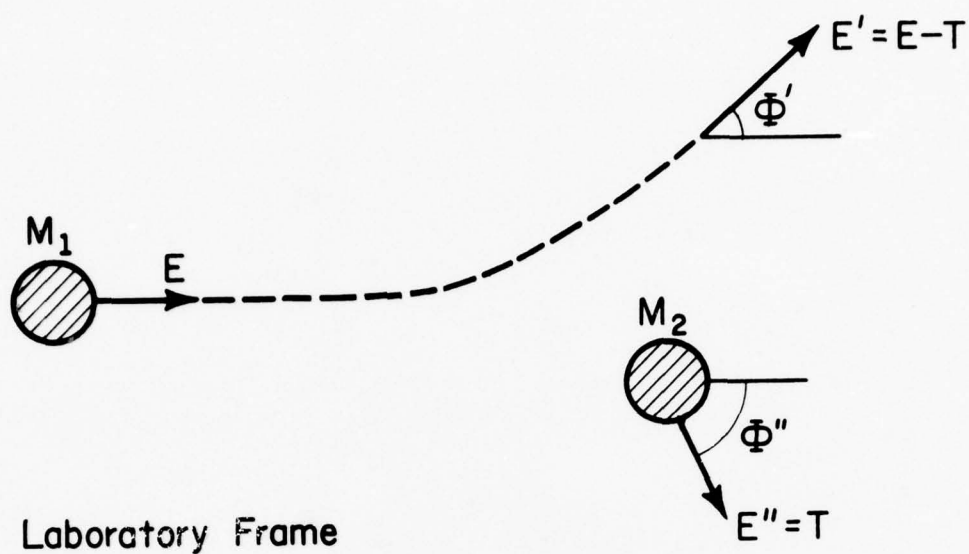


Figure 2.1. Two-body elastic collision in laboratory frame (top) and in center-of-mass system (bottom) (after Sigmund [9]).

Using trigonometric identities, the Eqs. (2.2) and (2.5) yield a more useful form

$$\cos \Phi'' = \left( \frac{T}{T_m} \right)^{1/2} \quad (2.7)$$

giving the trajectory of the recoil in the laboratory frame. To find the angle  $\theta$ , we integrate the potential between ion and target atom  $V(r)$  [11,12] in the center of mass system

$$\theta = \pi - 2p \int_{R_{\min}}^{\infty} \frac{dR/R^2}{\sqrt{1 - V(R) \left[ \frac{E_r}{E_r - p^2/R^2} \right]}} \quad (2.8)$$

where  $p$  is the impact parameter and

$$E_r = \frac{M_2 E}{(M_1 + M_2)} \quad (2.9)$$

is the particle energy in the center of mass system.  $R_{\min}$  is the minimum distance of approach (Fig. 2.1) determined by the zero of the radicand in the denominator of the integral in Eq. (2.8). Inversion of Eq. (2.8) yields the differential nuclear cross-section  $d\sigma(\theta)$  assuming azimuthal symmetry:

$$d\sigma = -2\pi p \frac{dp}{d\theta} d\theta \equiv \frac{-p}{\sin \theta} \frac{dp}{d\theta} d\Omega \quad (2.10)$$

where

$$d\Omega = 2\pi \sin \theta d\theta \quad (2.11)$$

Large angle collisions are a rarity at energies greater than 1 keV; thus, typical impact parameters are large. For these cases (the majority of all stopping events), we have [9]  $V(R)/E_r \ll 1$  and thus expansion in terms of  $V/E_r$  yields [14]

$$\theta \approx \frac{-p}{E_r} \int_p^\infty \frac{dR}{R} \frac{V(R)/dR}{\sqrt{1-p^2/R^2}} + \text{terms the order of } \left(\frac{V}{E_r}\right)^2 \quad (2.12)$$

It is important to note that this new expression is linear in  $V(R)$ ; thus, simultaneous collisions can be correctly described by the theory in this approximation.

To perform useful calculations, one must find an expression for the interatomic potential  $V(r)$ . Since accurate empirical potentials are available for only a few ion-target combinations, theoretical models are employed. The Thomas-Fermi model is most often used, due to its simplicity and generality. This model essentially considers the ion-target system as two Coulombic nuclei surrounded by an electron gas of variable density, considered uniform on a microscopic scale. From this picture of the atomic system, minimization of the total energy by a variational procedure leads to the Thomas-Fermi nonlinear differential equation [9,15].

$$\nabla^2 (V - V_0) = 4\pi\sigma_0 e (V - V_0)^{3/2} \quad (2.13)$$

where  $V$  is the electrostatic potential of the system,  $-eV_0$  is the Fermi energy, and  $\sigma_0$  is given by

$$\sigma_0 = .08533(ea)^{-3/2} \quad (2.14)$$

where  $a$  is the screening radius chosen by Lindhard et al. [10]

$$a = 0.8853 a_0 (Z_1^{2/3} + Z_2^{2/3})^{-1/2} \quad (2.15)$$

with  $Z_1$  and  $Z_2$  the atomic numbers of the ion and target nuclei, respectively, and  $a_0$  the Bohr radius ( $0.528 \text{ \AA}$ ).

The solution to this equation is then

$$V(r) = \frac{Z_1 Z_2 e^2}{R} \phi_0(R/a) \quad (2.16)$$

where  $\phi_0$  is a function found by numerical integration. Conveniently, the function  $\phi_0$  can be approximated by inverse powers of its argument over extended distances (Fig. 2.2). The form of Eq. (2.16) illustrates the utility of the Thomas-Fermi approach, in that the details of atomic structure do not enter into the calculations, and thus the theory can easily be extended to cover all possible ion-target combinations. The only changes that occur from one ion target system to another are in length scale (given by Eq. (2.15)), and the total number of electrons (determined by  $Z_1$  and  $Z_2$ ). Using Eq. (2.16) for the interatomic potential, Eq. (2.8) becomes

$$\theta = \pi - 2 \frac{p}{a} \int_{\frac{R_{min}}{a}}^{\infty} \frac{d(R/a)/(R/a)^2}{\sqrt{1 - \frac{Z_1 Z_2}{a E_r} \frac{\phi(R/a)}{R/a} - \frac{(p/a)^2}{(R/a)^2}}} \quad (2.17)$$

This expression can be simplified by approximating the potential of Eq. (2.16) by inverse powers of its argument (Fig. 2.2)

$$\phi_0(R/a) = \frac{k_s}{s} (a/R)^{s-1} \quad (2.18)$$

with  $s$  an integer and  $k_s$  a numerical constant. The expression for  $\theta$  then results by substituting Eq. (2.18) into the approximate form Eq. (2.12)

$$\theta = \frac{\gamma_s k_s}{\epsilon} \left(\frac{a}{p}\right)^s \quad (2.19)$$

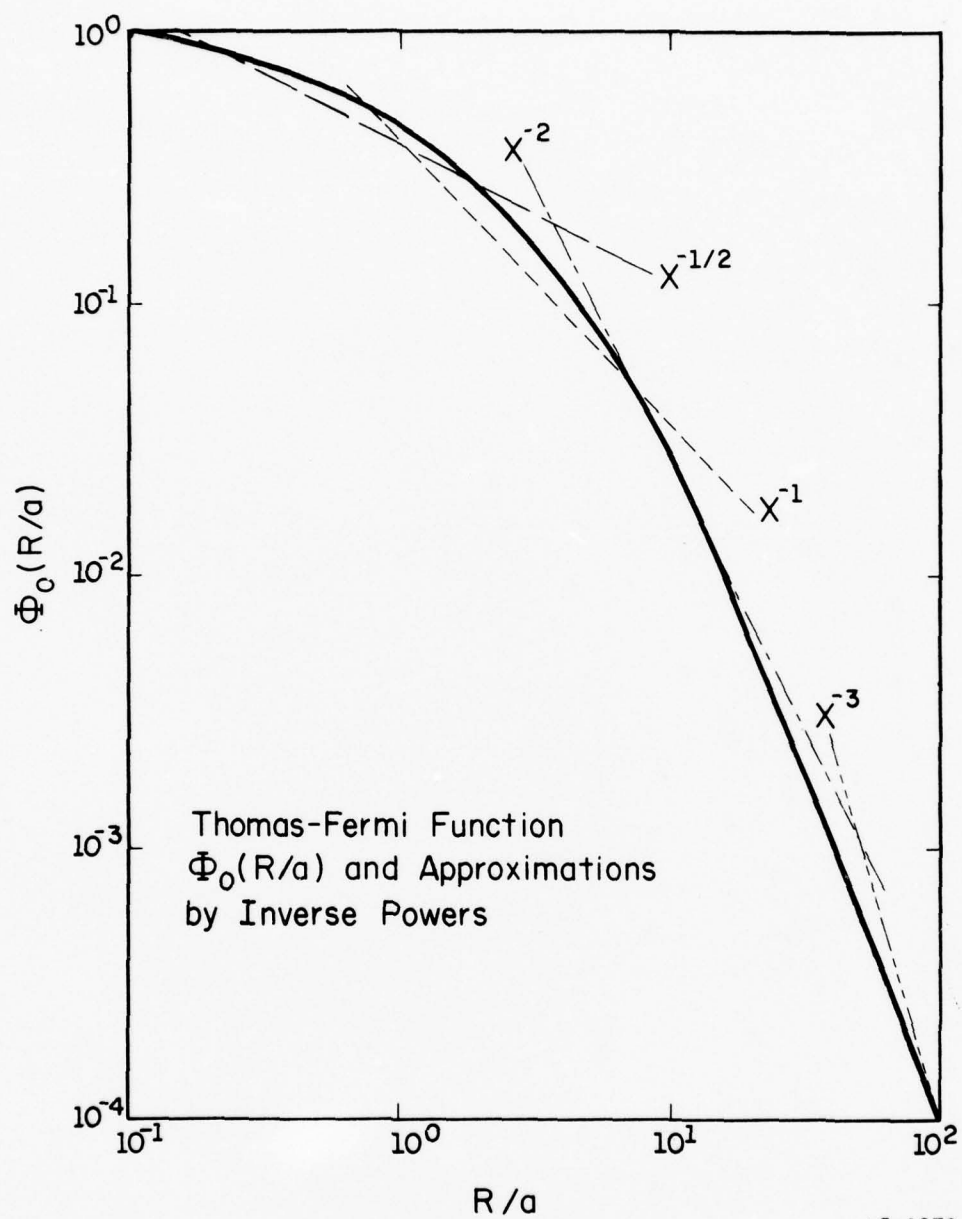


Figure 2.2. Thomas-Fermi screening function  $\Phi_0(x)$  for neutral atoms and its approximation by inverse powers of its argument (after Gombas [16]).



where

$$\gamma_s \approx \frac{1}{s} \sqrt{\frac{3s-1}{2}} \quad (2.20)$$

and  $\epsilon$  is a dimensionless scaling unit for the center of mass energy  $E_r$

$$\epsilon = \frac{aE_r}{Z_1 Z_2 e^2} \quad (2.21)$$

Having finally obtained an expression for  $\theta$ , we now can substitute into Eq. (2.10) to obtain

$$d\sigma(\theta) = (\text{constant}) a^2 \epsilon^{-2/s} \theta^{-1-2/3} d\theta \quad (2.22)$$

A more useful expression is obtained by substituting for  $\theta$  from Eqs. (2.5) and (2.6) assuming  $\theta$  is small:

$$d\sigma(T) = C \epsilon^{-m} T^{-1-m} dT \quad (2.23)$$

with

$$m = \frac{1}{s} \quad (2.24)$$

and

$$C = \frac{\pi}{2} \lambda_m a^2 \left( \frac{M_1}{M_2} \right)^m \left( \frac{2Z_1 Z_2 e^2}{a} \right)^{2m} \quad (2.25)$$

Fitting constants to the Thomas-Fermi function yields [16]

$$\lambda_{1/3} = 1.309 \quad (2.26)$$

$$\lambda_{1/2} = 0.327 \quad (2.27)$$

$$\lambda_1 = 0.5 \quad (2.28)$$

The approximations used for various energy intervals are:

$$m = 1/3 \quad \text{for } \epsilon \lesssim 0.2 \quad (2.29)$$

$$m = 1/2 \quad \text{for } 0.08 \lesssim \epsilon \lesssim 0.2 \quad (2.30)$$

$$m = 1 \quad \text{for } \epsilon \gtrsim 10 \quad (2.31)$$

To this point we have considered  $\sigma$  as a function of two variables,  $\epsilon$  and  $\theta$  (or equivalently  $E$  and  $T$ ). However, Lindhard et al. have shown [10] that to the validity of the power approximation, Eq. (2.18), the differential cross section can be considered a function of the single variable  $t$ , where

$$t = \epsilon^2 \frac{T}{T_m} \quad (2.32)$$

Thus Lindhard et al. [10] use

$$d\sigma = \pi a^2 \frac{dt}{2t^{3/2}} f(t^{1/2}) \quad (2.33)$$

where  $f(t^{1/2})$  is plotted in Fig. 2.3. The next step is to generalize from a collision between an ion and a single target atom to the case of a target consisting of a collection of atoms distributed randomly with a density  $N$  (atoms/cm<sup>3</sup>) over a depth  $\Delta x$ . For this case, the probability  $P$  for an ion to suffer a collision specified by a cross section  $d\sigma$  is given by

$$dP = N\Delta x d\sigma \quad (2.34)$$

for  $\Delta x$  small enough so that  $dP \ll 1$ . For an initial energy  $E$  with recoil energy  $T$ , the average energy loss  $\langle \Delta E \rangle$  is then

$$\langle \Delta E \rangle = \int T dP = N\Delta x \int_{T=0}^{T_m} T \frac{d\sigma}{dT} dT \quad (2.35)$$

In the limit of infinitesimal  $\Delta x$ , Eq. (2.35) becomes

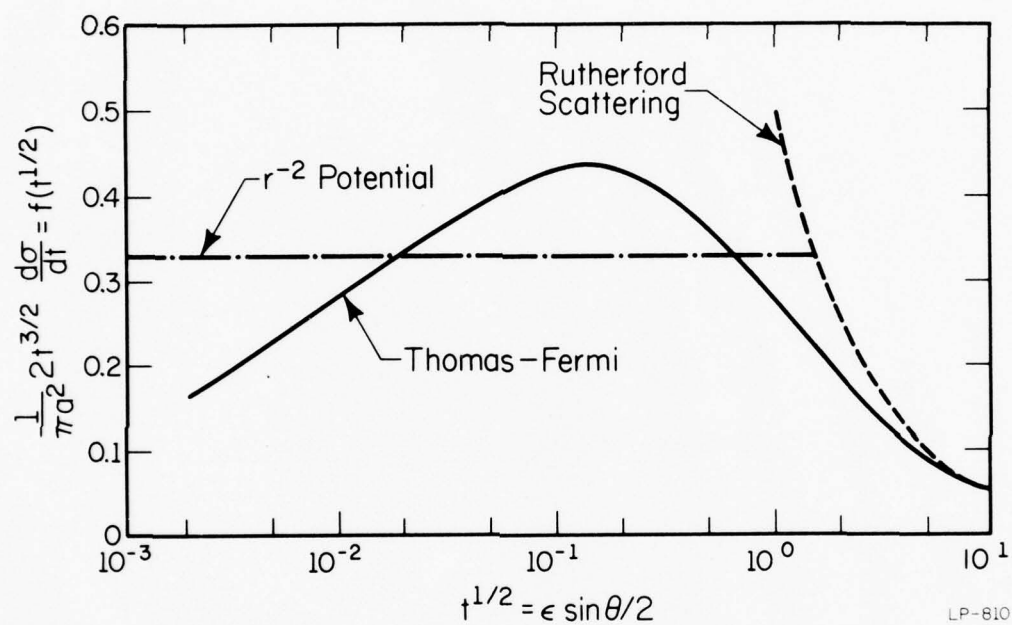


Figure 2.3. Differential cross section for elastic collisions  $f(t^{\frac{1}{2}})$  vs.  $t^{\frac{1}{2}}$ ; with approximation by  $r^{-2}$  potential and high energy limit of Rutherford scattering (after LSS [10]).

$$\frac{dE}{dx} = - N S_n(E) \quad (2.36)$$

where

$$S_n(E) \equiv \int_{T=0}^{T_m} T \frac{d\sigma}{dT} dT \quad (2.37)$$

We have implicitly used Eq. (2.32) to write total differentials for our cross section. Common usage is to employ Eq. (2.33) and introduce a dimensionless length parameter  $\rho$

$$\rho = N \pi a^2 \frac{4M_1 M_2}{(M_1 + M_2)} x \quad (2.38)$$

to obtain in dimensionless units

$$\frac{d\epsilon}{d\rho} = - S_n(\epsilon) = \int_0^{\epsilon} d(t^{1/2}) f(t^{1/2}) \quad (2.39)$$

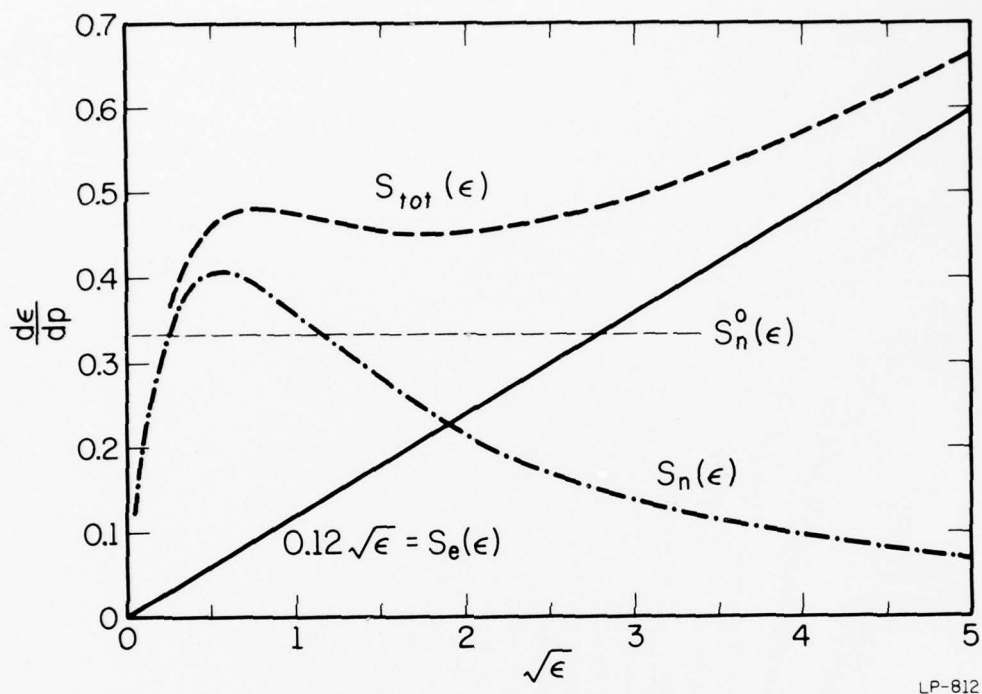
The behavior of  $S_n(E)$  can be seen from Fig. 2.4. Using the power approximation, Eq. (2.23), this equation can be integrated directly to yield, in terms of  $E$  vs.  $t$

$$S_n(E) = \frac{1}{1-m} C \gamma^{1-m} E^{1-2m} \quad (2.40)$$

For ions in the keV range, Eq. (2.30) provides the best approximation. For this case, Eqs. (2.25), (2.27), (2.30), (2.37) and (2.40) yield

$$\frac{dE}{dx} = - 1.308 \pi N a Z_1 Z_2 e^2 \frac{M_1}{M_1 + M_2} \quad (2.41)$$

where we recall that the subscript 1 refers to the incident ion.



LP-812

Figure 2.4. Nuclear stopping ( $S_n(\epsilon)$ ), electronic stopping ( $S_e(\epsilon)$ ), and total stopping ( $S_{tot}(\epsilon)$ ) in dimensionless units. The electronic stopping power is given for  $k = 0.12$ . Also shown is the approximation of the nuclear stopping power for a  $r^{-2}$  potential  $S_n^0(\epsilon)$ . (After LSS [10].)

Thus we have finally arrived at an analytic description of the elastic energy transfer during the ion-target collision. Naturally, this is the energy used to produce recoiling target atoms, and thus will be most important for estimation of recoil densities. The development of these expressions is rigorous within the assumptions made, and is firmly based on classical dynamics. It is important to note that quantum effects (i.e., deviations from classical mechanics) do indeed take place. These effects include purely electronic excitation, exchange scattering, and resonant charge transfer [17]; however, these effects typically amount to only a few percent of the energy exchange for ions with kinetic energies of 1 keV or greater.

We now consider electronic stopping for the case of implanted ions. For these conditions, the majority of target electrons are travelling much faster than the incident ion, so that the electrons cannot pick up any energy from direct collisions with the ion.

Earlier in this discussion it was pointed out that electronic excitation amounts to only a few percent of the energy transfer during nuclear collisions. However, the major contribution to electronic stopping occurs from those collisions in which the nuclei are far enough apart to prevent any appreciable transfer of kinetic energy, but in which some overlap of outer shell electrons can occur [9]. Since the differential cross section is proportional to the impact parameter (Eq. (2.10)), these collisions can assume a considerable statistical weight. There is no definitive theory on electronic stopping; therefore, we again concentrate on understanding the physical mechanisms rather than focusing on details of the computational procedure.



In the coordinate system of the ion, orbital electrons have a small drift velocity. Thus, when an electron is scattered by the moving ion [10], or is captured by the moving ion [18], a net momentum (which is proportional to the ion velocity) is transferred to this electron. According to these arguments, the energy lost by the ion would then yield a stopping power proportional to the ion's velocity

$$S_e = kv = kE^{1/2} \quad (2.42)$$

The value for the constant  $k$  depends on the model used; however, the common practice in compilations of range statistics is to use experimentally-determined stopping coefficients when available [19].

It should also be noted that when Hartree-Fock models are used for the ion-target combination, pronounced oscillations are found for the electronic stopping power as a function of the ion atomic number [20]. Such oscillations are not predicted by the simpler models mentioned above, but are observed experimentally [21] and have been included in compilations of range statistics [19]. Recent work [22] has shown, however, that their effects have been overestimated for random implants into silicon targets.

Having developed expressions for the nuclear and electronic stopping powers, we are now in a position to formulate the depth distribution of implanted ions. Along an incremental path length  $\Delta x$ , an incident ion suffers an energy loss due to nuclear and electronic stopping, given by [10]:

$$\Delta E = - N(S_n(E) + S_e(E))\Delta x \quad (2.43)$$

In the limit of vanishingly small  $\Delta x$

$$\frac{dE}{dx} = - N(S_n(E) + S_e(E)) \quad (2.44)$$

so that to a first approximation

$$R(\epsilon) = \int_{\epsilon}^0 \frac{dE}{dE/dx} = \int_0^{\epsilon} \frac{dE}{N(S_n(E))} \quad (2.45)$$

or in  $\epsilon$ - $\rho$  units

$$\rho(\epsilon) = \int_0^{\epsilon} \frac{d\epsilon}{S_n(\epsilon) + S_e(\epsilon)} \quad (2.46)$$

Unfortunately, the range travelled by an ion is not a physical observable, since the ion does not travel in a straight line from the target surface. Instead, the ion is deflected at an angle  $\theta$  each time it suffers a nuclear collision (Fig. 2.1a). Because the ions approach target atoms with a variety of impact parameters, we obtain a distribution of ion penetration depths, or equivalently, a probability distribution for the depths a particular ion can come to rest within the sample surface.

There are several approaches to the calculations of ion ranges, but none of these methods produce less than a 10 - 20% deviation from measured values [9]. Here we follow the method of Sigmund [9], which most easily allows the calculation of recoil densities. The method of Brice has also recently been modified to include the effects of recoiling target atoms [23]. Sigmund employs the concept of a final range distribution  $F(E, \bar{e}, \bar{r})$ , which is the probability that an ion with initial energy  $E$  directed along a unit vector  $\bar{e}$  will come to rest a (vector) distance from the point at which it encountered the sample surface ( $\bar{r} = 0$ ). Fairly straightforward arguments [9] yield the equation

$$\begin{aligned}
- \cos \psi \frac{\partial}{\partial x} F(E, \bar{e}, \bar{r}) &= N \int d\sigma \{ F(E, \bar{e}, x) - F(E-T, \bar{e}'x) \} \\
&+ NS_e \frac{\partial}{\partial F} F_T(E, \bar{e}, x)
\end{aligned} \tag{2.47}$$

where  $x$  is the depth measured normal to the target surface and

$$\cos \psi = \bar{e} \cdot \hat{x} \tag{2.48}$$

with  $\bar{e}'$  a unit vector in the direction of the scattered ion, and  $\hat{x}$  a unit vector in the  $x$  direction. Here we have already integrated the  $y$  and  $z$  dependence. This equation is basically a Taylor's series expansion, valid for terms linear in  $\partial x$ . For symmetry reasons [9], we have for arbitrary incident direction  $\psi$ :

$$F(E, \bar{e}, x) = F(E, \cos \psi, x) \tag{2.49}$$

together with the normalization

$$\int_{-\infty}^{\infty} dx F(E, \cos \psi, x) = 1 \tag{2.50}$$

where the integration extends over all space to include backscattered ions. We now have a compatible set of equations which can ideally be solved for the distribution of penetration depths.

Most calculations do not attempt to solve Eqs. (2.47) and (2.50), but rather expand these equations in terms of spatial moment  $F^n(E, \bar{e})$  over the depth distribution  $F(E, \bar{e}, \bar{r})$  [9,24]:

$$F^n(E, \bar{e}) = \int_{-\infty}^{\infty} dx x^n F(E, \bar{e}, x) \tag{2.51}$$

with  $F^0 = 1$ . This procedure yields

$$nF^{n-1}(E, \bar{e}) = N \int d\sigma \{ F^n(E, \bar{e}) - F^n(E-T, \bar{e}) \} \\ + N S_e(E) \frac{\partial}{\partial E} F^n(E, \bar{e}) \quad (2.52)$$

with  $F^0 = 1$ .

While the expansion, Eq. (2.46), relieves many computational difficulties, it must be noted that Eq. (2.46) requires knowledge of the previous  $F^n(E)$  to determine  $F^{n+1}(E)$ . This places great demands on the accuracy to which the previous coefficient must be obtained. It can be shown that the first moment yields the average penetration depth  $R_p$  [9] and a Gaussian-type distribution centered around  $R_p$  with a standard deviation or straggle (referred to as  $\sigma_p$ ). For many practical applications, the gaussian approximation is sufficient. For example, Marcyk and Streetman [25] have shown that the gaussian approximation describes the summation of  $B^+$  implantations at various energies into a common Si target.

Thus far we have described range distributions into an amorphous substrate of only one chemical species. To include compound substrates, a weighted average of the stopping powers of each element over their elemental density is performed. Thus  $SiO_2$  is modelled by a pseudo-element of atomic number 10 and atomic weight 20.0. An entirely different effect occurs for ions incident on single crystalline targets. This effect, referred to as "channelling" [26], occurs when an ion is incident upon (or scattered into) a path within a few degrees of a low index crystalline direction. For these ions, a collective steering effect from rows of target atoms repels the channelled ions and prevents them from suffering direct nuclear collisions. These ions thus travel further due to their more direct path, encountering

only electronic stopping. Since a randomly-oriented silicon substrate is driven amorphous by doses of  $\sim 10^{14}$  ions/cm<sup>2</sup> [27], it is possible that a significant fraction of the initial dose could become channelled before the implanted silicon undergoes an amorphous transition [28]. This phenomenon would then yield a tail near the end of the distribution. Since many of the properties of semiconductor devices, such as junction capacitance [28] and solar cell collection efficiencies [29], are sensitive to the shape of dopant distributions, channelling may be an important consideration. Simple methods of controlling or eliminating this effect could be of great technological importance.

We finally consider the problem of recoil implantation. As the incident ion encounters target atoms, it transfers some of its kinetic energy to the substrate atoms according to Eqs. (2.2), (2.4), and (2.5). At somewhat lower energies, the incident ion continues in a modified direction. Should the energy transfer be greater than the chemical energy binding the target atoms in place, the target atoms would proceed in the direction specified by  $\hat{\Phi}''$  (determined by Eq. (2.7)). These atoms travel a distance which depends on their energy loss in the target medium. Such primary recoils might then set other target atoms in motion due to further nuclear collisions, and so on.

To gain an understanding of the distribution of recoil-implanted atoms, one first considers the case of a densely-packed monomolecular layer on the surface of a silicon target. Such a situation could be approximated by hydrocarbon pump oil adsorbed onto a wafer surface in the target chamber of an ion implanter. Since the layer is only one molecule thick, electronic stopping can be neglected, and hence we only consider nuclear collisions.

Considering an  $^{75}\text{As}$  beam of 100 keV striking a  $^{12}\text{C}$  layer, we see from Eq. (2.6) that at most 48 keV of energy could be transferred to a carbon atom, for a direct collision ( $p = 0$ ). This would yield a penetration depth for the carbon atom of  $1118 \text{ \AA}$ , as estimated from projected range compilations [19], whereas the arsenic ion would only have a projected range of  $582 \text{ \AA}$ . However, this condition is only for the extremely unlikely event of a direct collision; more probably the incident beam will have a variety of impact parameters, which would yield a distribution of recoil energies with accordingly smaller projected ranges. Additionally, these lower energy recoils will travel at an angle to the surface, determined by Eq. (2.7), and thus would have shallower penetration depths measured normal to the sample surface. It is important to note that the amount of energy transfer depends on the ion-atom mass ratio. For the case of a nitrogen beam striking a carbon layer, the maximum energy transfer could be as large as 99%.

To estimate the recoil yield from a thin target into a substrate of a different material, Moline *et al.* [31] have developed a simple formalism to estimate recoil implantation yields for the case of a heavy projectile impinging on a lighter target. If the incident ion strikes a target atom a distance  $\xi$  from the target-substrate interface, this recoil can penetrate the substrate only if the range of the recoil projected normal to the target surface is greater than the distance to the interface.

Mathematically, if the collision transfers an energy  $T$  to the target atom, we consider the recoil only for the case where

$$R_p(T) \cos \phi'' \geq \xi \quad (2.53)$$



The total number of recoils  $n$  from depth  $\xi$  is then given by

$$\frac{dn}{d\xi} = N_t \int_{T_1}^{T_m} d\sigma T \quad (2.54)$$

where  $T_1$  is the minimum value of energy transfer for which Eq. (2.53) holds,  $N_t$  is the density of target atoms,  $T_m$  is defined by Eq. (2.6) and  $d\sigma(T)$  is the differential cross section for a collision with energy transfer  $T$ .

Using Eqs. (2.23), (2.25) and (2.30) to represent  $d\sigma(T)$ , Eq. (2.54) becomes

$$\frac{dn}{d\xi} = \frac{0.33\pi a^2 N_t}{\epsilon_1} \left[ \left( \frac{T_m}{T} \right)^{1/2} - 1 \right] \quad (2.55)$$

with  $a$  defined in Eq. (2.15) and  $\epsilon_1$  defined in Eq. (2.21). The use of Eq. (2.30) implies the approximation of the Thomas-Fermi screening function by a  $1/r^2$  potential. Moline et al. further approximate the stopping powers of the target for both the incident ion ( $S_1$ ) and recoil ( $S_2$ ) by constants (Fig. 2.4). With this approximation, we have

$$E_1 = E - (W - \xi)S_1 \quad (2.56)$$

where  $E$  is the incident ion energy,  $E_1$  the projectile energy at distance  $\xi$  from the target-substrate interface, and  $W$  the thickness of the target layer (i.e.  $\xi = W$  is the front surface of the target).

Using Eq. (2.56), Eq. (2.54) becomes

$$n = 0.33\pi a^2 N_t \frac{E}{\epsilon_1} \int_0^W \frac{u}{E_1} d\xi \quad (2.57)$$

where

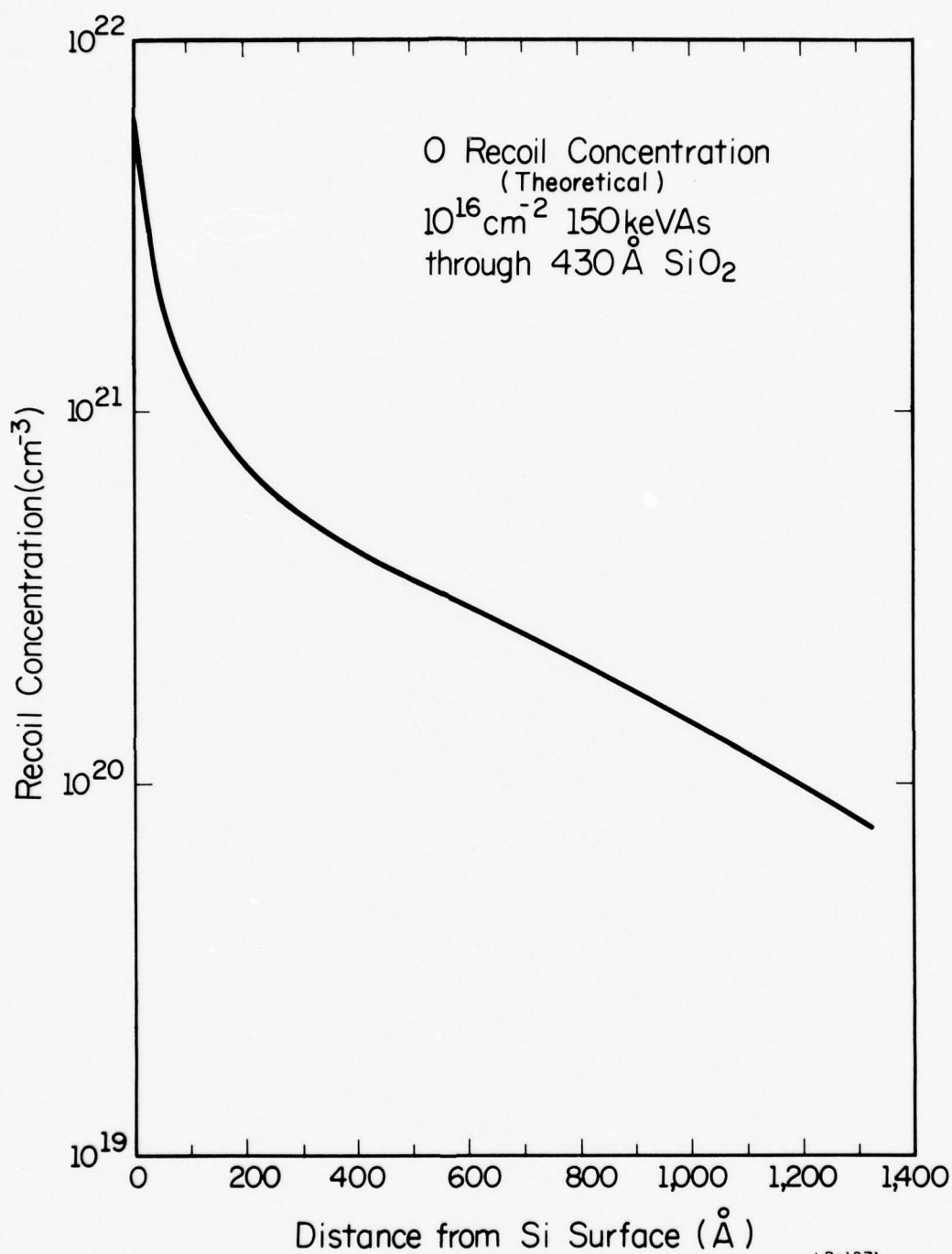
$$u = \begin{cases} \left[ \frac{\gamma E_1}{S_2} \right]^{1/3} - 1 & \text{for } \gamma E_1 > S_2 \xi \\ 0 & \text{otherwise} \end{cases} \quad (2.58)$$

with

$$\gamma = \frac{T_m}{E} . \quad (2.59)$$

The above equation is then numerically integrated to yield the recoil distribution. The results of the above approach for the case of 150 keV  $\text{As}^+$  implanted through 430 Å of  $\text{SiO}_2$  [7] are shown in Fig. 2.5. While the above approach has included a considerable number of approximations, it has been shown to be accurate within a factor of 2 for the implantation of oxygen from thin  $\text{SiO}_2$  layers on Si bombarded by  $\text{Kr}^+$  ions, and is expected to give at least an order of magnitude estimate for the case considered here.

As a final note, it is worthwhile to emphasize the difficulties in trying to develop theoretical estimates of the processes that occur in implantation through a multilayer target. We first recall that range distribution calculations for single-element amorphous targets produce no less than a 10 - 20% deviation from measured values, due to such problems as shell effects in electronic excitation, electronic excitation during nuclear collisions, loss of ions through back scattering, erosion of the target surfaces due to sputtering, and difficulties in developing accurate solutions to the range equation (Eq. (2.42)) [9]. If we now consider the production of recoils from a  $\text{SiO}_2$  layer of finite thickness, we are faced with additional difficulties. Theoretical estimates of the stopping power of  $\text{SiO}_2$  give results significantly in error from experimentally determined values [32]. Measurements of  $\text{SiO}_2$  films on Si surfaces indicate that nearly 10 oxygen atoms are sputtered



LP-1271

Figure 2.5. Calculated depth distribution of oxygen recoils for a  $10^{16} \text{ cm}^{-2}$  150 keV As implant through 430 Å of  $\text{SiO}_2$  (after Moline *et al.* [7]).

away for each oxygen atom recoil-implanted for a 200 keV As implant [5]; thus, a strict treatment of implantation through a  $\text{SiO}_2$  layer would have to treat the target surface as a boundary that moves as a function of ion dose. This would lead to a further spread in the recoil distribution beyond the interface and would also increase the recoil yield with dose, due to the fact that recoils from the surface would have to travel a shorter distance to the substrate as the surface erodes. For example, analysis of an oxide layer before and after a  $1 \times 10^{16} \text{ cm}^{-2}$  200 keV As implantation yielded a decrease of 36 Å in an  $\text{SiO}_2$  layer originally 176 Å thick [5], a 20% change.

In addition to affecting the recoil yield, oxide erosion also affects the shape of the As distribution inside the Si layer, for exactly the same reasons. One further consideration also affects the As distribution inside the Si for a through-oxide implant. Since  $\text{SiO}_2$  has a greater stopping power than Si, the distribution of As ions that penetrate the  $\text{SiO}_2$ -Si interface is peaked at a shallower range than for an equivalent implantation in a homogeneous Si sample. This would imply a smaller penetration depth and thus higher peak concentration and a steeper fall-off for the As profile. Finally, the variation in stopping powers also affects the mathematical treatment of implants through multiple layers. Again, since  $\text{SiO}_2$  has a greater stopping power, ions that would come to rest just beyond the interface, based on  $\text{SiO}_2$  range statistics, in fact travel further in the Si due to being in a material with a lower stopping power. Neglecting ion backscattering, this would yield a distribution that is discontinuous at the interface [33]. Such a discontinuity has not been experimentally observed.

The theory of implantations into layered targets is still in an early state of development, and therefore, experimental examination of a given set of conditions provides the best analysis. However, as more data becomes generated, we can look forward to greater refinements in the theory.

### 3. PHOTOLUMINESCENCE

Low-temperature photoluminescence has been shown to be an extremely sensitive monitor of radiation damage in silicon [34-37], including damage resulting from ion implantation [38,39]. Luminescence spectra from radiation-damaged silicon have been studied to relate trace impurities growth techniques and the presence of chemical dopant impurities to the formation and annealing of defects in silicon. For these reasons, it is natural to apply this technique to the study of the residual damage seen following arsenic implantations into silicon through  $\text{SiO}_2$ . The advantage of photoluminescence as a diagnostic technique is the sensitivity of radiative recombination to the presence of defects. It is also possible to correlate peaks in the recombination spectra to known defects which have well-characterized impurity dependences. This chapter contains an introductory description of the technique of low-temperature photoluminescence, and the impurity dependence of the major peaks seen in the recombination spectra of implanted silicon. This method is then applied to the specific problem of through-oxide arsenic implants.

#### 3.1. Photoluminescence System

The luminescence system used in this work is schematically illustrated in Fig. 3.1. Light from a 500 W high-pressure Hg lamp is chopped, filtered to remove its infrared components, and focused onto the surface of a sample held in a liquid helium temperature cryostat. This light, with photon energies greater than the Si bandgap, is absorbed at the sample surface, creating excess carriers. Some of these carriers recombine radiatively, and the resulting luminescence (lower than bandgap energy) passes through the



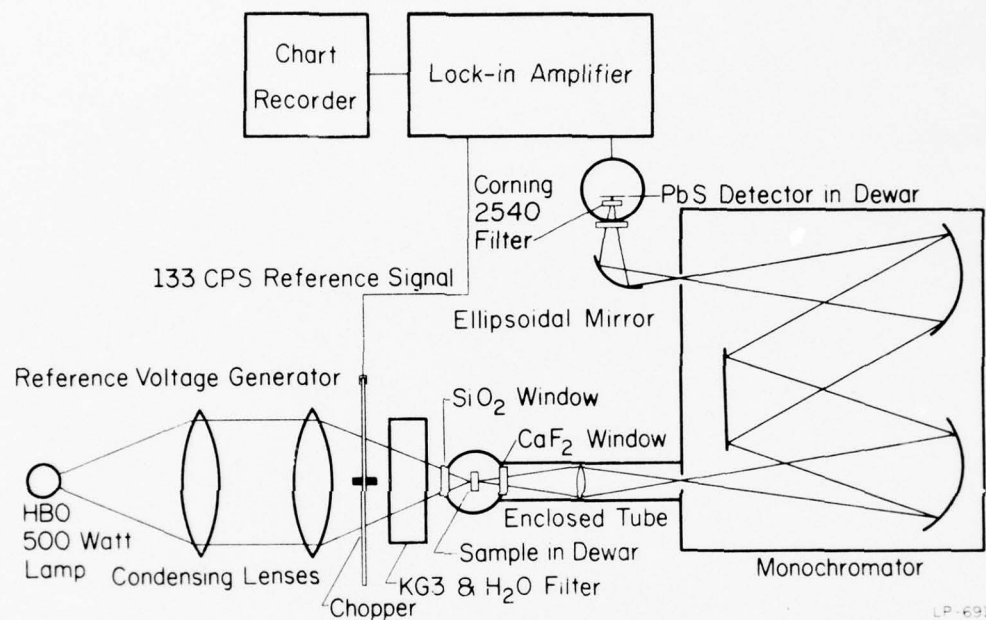


Figure 3.1. Schematic diagram of luminescence system.

sample and exits at the back surface. This luminescence is collected, spectrally analyzed in a Jarrell-Ash 0.5m spectrometer, and detected by a PbS detector ( $D^* = 6 \times 10^{11} \text{ cm (Hz)}^{-\frac{1}{2}}/\text{watt}$ ) using lock-in techniques. Spectra are corrected for system response, detector output, monochromator calibration and sample observation temperature. Detailed descriptions of the cryostat and optical system are given elsewhere [36].

### 3.2. Silicon Luminescence and Defect Identification

Since silicon is an indirect semiconductor, luminescence at the bandgap energy is not observed, and instead excitons recombine with the aid of momentum-conserving phonons. This yields the spectrum shown in Fig. 3.2. Because the TO phonon has the largest density of states [40], this phonon-assisted band yields the highest luminescent intensity. The intrinsic luminescence spectrum shown in Fig. 3.2 is suppressed by particle irradiation, and defect-related luminescence is observed instead (Fig. 3.3). This luminescence is characterized by dominant zero-phonon peaks due to electronic transitions at defects and by associated lower energy bands due to phonon participation in the transitions.

The three dominant zero-phonon peaks seen from ion-implanted silicon are those at 1.018 eV, 0.970 eV, and 0.790 eV. The 1.018 eV line has been identified [39] with a five-vacancy complex modelled by EPR [41]. The 0.970 eV peak was until recently identified with the divacancy [36], and the 0.790 eV line was attributed to the SiG (15) (or K) center [36]. However, the latter two assignments have been disputed on the basis of low-temperature irradiation studies [37] and the effects of Al and Ga impurities on these centers [42].

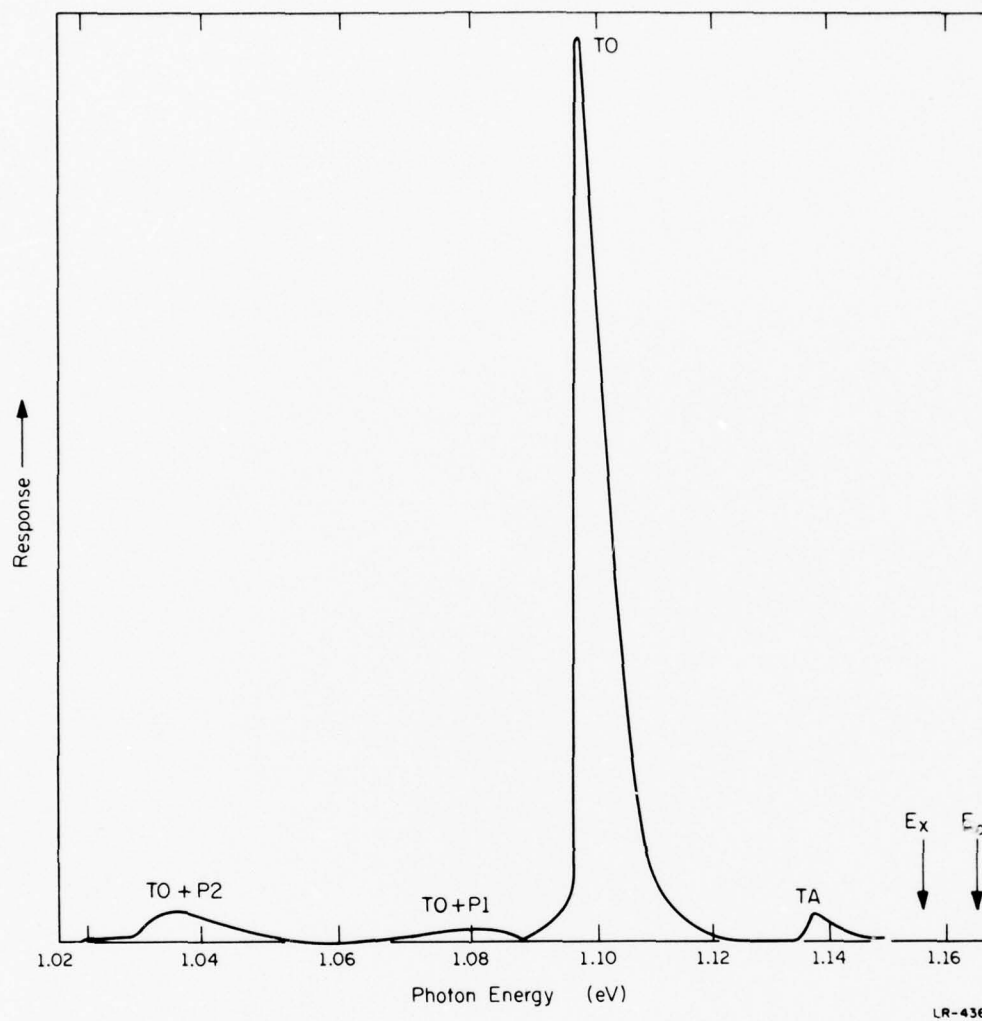


Figure 3.2. Free exciton recombination luminescence from unirradiated, high resistivity Si showing bandgap energy  $E_0$  and energy of bandgap minus exciton binding energy  $E_x$  (after Haynes [40]).

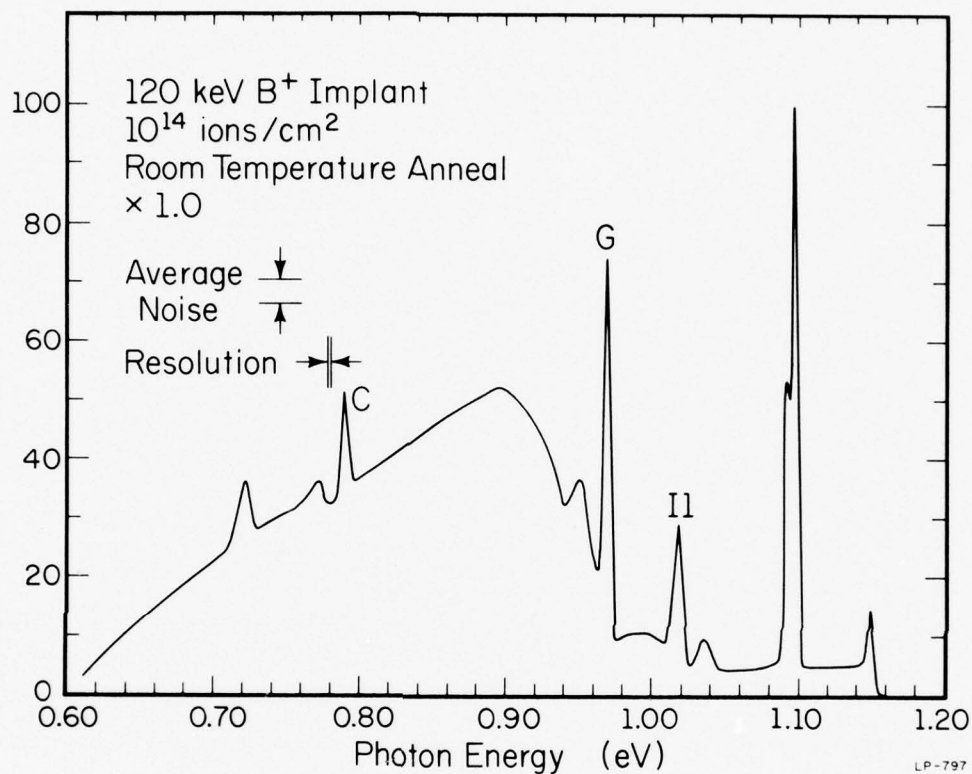


Figure 3.3. Recombination luminescence from p-type pulled Si implanted with 120 keV B<sup>+</sup> to a fluence of 10<sup>14</sup> ions/cm<sup>2</sup> following room temperature annealing. The peak near 1.10 eV is due to free exciton recombination, while the peaks at 1.018 eV (Il), 0.970 eV (G), and 0.790 eV (C) are due to irradiation induced defects (after Noonan *et al.* [38]).

These recent studies suggest identification of the 0.970 eV line with the split  $\langle 111 \rangle$  carbon interstitialcy defect, and the 0.790 eV line with a carbon-modified A center (O-vacancy complex). Photoluminescence studies of carbon- or oxygen-implanted silicon were performed [43], and the latter experiment suggested that impurity dependence of the 0.970 and 0.790 eV peaks could only be determined by examining the effects of incorporated impurities on the photoluminescence spectra following irradiation. For this reason,  $\langle 111 \rangle$  n-type,  $121\text{-}83\ \Omega\text{-cm}$  silicon wafers were implanted with  $1 \times 10^{14}\text{ cm}^{-2}$  150 keV  $\text{O}^+$ , or  $1.1 \times 10^{14}\text{ cm}^{-2}$  111 keV  $\text{C}^+$ , or both. These doses and energies were chosen to provide nearly identical impurity depth distributions in the substrates, with peak concentrations of  $5 \times 10^{18}\text{ cm}^{-3}$  [19]. These wafers, along with an unimplanted control wafer, were annealed at  $900^\circ\text{C}$  under flowing argon gas to remove the primary implantation damage and then were irradiated with  $10^{17}\text{ cm}^{-2}$  2.5 MeV electrons at  $0^\circ\text{C}$ . These wafers were examined as irradiated and also after a  $200^\circ\text{C}$  anneal, which increases the intensity of the peaks. The resultant intensities of the three major peaks are summarized in Table I. From these results, it can be seen that the 0.970 eV peak dramatically increases in intensity for those samples which had been doped with carbon prior to the irradiation. After room temperature annealing, the 0.970 eV line appears at greater intensity in the carbon- and oxygen-doped substrates than in the substrate doped with carbon only; however, following a  $200^\circ\text{C}$  anneal, the intensity of this peak increases sharply for the oxygen-lean sample. This behavior is identical to that seen from electron irradiated pulled (oxygen-rich) and float zone (oxygen-lean) silicon [44], and demonstrates the interaction between carbon and oxygen in the recovery of radiation damaged silicon [45]. The carbon dependence of this peak is

TABLE I

Relative intensities of the major luminescence peaks from ion implantation-doped, electron-irradiated float zone (n-type, 121-83  $\Omega$ -cm) silicon. All implantations were performed at  $7^\circ$  off the  $\langle 111 \rangle$  axis at room temperature, at energies of 111 keV and 150 keV, to fluences of  $1.1 \times 10^{14}$  and  $10^{14} \text{ cm}^{-2}$  for carbon and oxygen, respectively. The electron irradiations were performed at  $0^\circ\text{C}$  at 2.5 MeV to a fluence of  $10^{17} \text{ cm}^{-2}$  into material previously implanted as indicated in the dopant column, followed by  $900^\circ\text{C}$  anneals.

| <u>Dopant</u> | <u>Room Temperature Anneal</u> |                 |                 | <u><math>200^\circ\text{C}</math> Anneal</u> |                 |                 |
|---------------|--------------------------------|-----------------|-----------------|--|-----------------|-----------------|
|               | <u>0.790 eV</u>                | <u>0.970 eV</u> | <u>1.018 eV</u> | <u>0.790 eV</u>                              | <u>0.970 eV</u> | <u>1.018 eV</u> |
| C,O           | 185                            | 407             | *               | 332  | 383             | *               |
| C             | 13                             | 330             | *               | 92   | 580             | *               |
| O             | 110                            | 75              | *               | 187  | 119             | 17              |
| *             | 29                             | 49              | *               | 44   | 88              | 85              |



consistent with the previously suggested identification of this center with the split  $\langle 111 \rangle$  carbon interstitialcy (Si-G-11) center [37]. Together with the results of the low temperature irradiations [37] and the effects of Ga impurities on the spectra from irradiated silicon [42], this work further reinforces the proposed defect identification.

The samples which had been intentionally doped with oxygen showed very strong 0.790 eV signals compared with those which had not been oxygen-implanted. This behavior is consistent with previous studies of irradiated oxygen-doped silicon [36]. While the oxygen dependence of the 0.790 eV peak has been previously identified, the carbon dependence of this peak has not been determined prior to the work reported here. Table I indicates that the 0.790 eV luminescence is higher in the samples doped with both carbon and oxygen compared with those doped with oxygen alone, consistent with the hypothesis that the 0.790 eV luminescence arises from the carbon-modified A center. The weak presence of the 0.790 eV peak in those samples which had not been oxygen-implanted appears to be the result of oxygen contamination from the high temperature annealing prior to the electron irradiation.

The growth of the 1.018 eV peak is consistent with its identification with the five vacancy complex. This peak is seen strongly for ion-implanted silicon after room temperature irradiations, but has never been seen directly after electron irradiations [43]. That this center is seen in these electron-irradiated samples is an effect of the interaction of impurities with irradiation-induced defects during the annealing process. Both carbon and oxygen are efficient vacancy traps [44]. Simpler defects, such as the E (donor-vacancy) center, break up by 200°C, liberating vacancies which can in turn

become trapped by carbon or oxygen impurities. One would then expect to see the highest intensity from a vacancy-related center in those samples which have the lowest carbon and oxygen concentrations. Thus, we see in Table I that the 1.018 eV peak is greatest in intensity at 200°C annealing for the control sample, and next largest in intensity for the sample doped with oxygen. This behavior correlates well with the already strong case for the identification of the 1.018 eV peak with the five vacancy complex [39].

In addition to the peaks mentioned above, new peaks were seen in the photoluminescence spectra from the irradiated samples. Unfortunately, the intensities of these peaks were too small to allow detailed investigation. These samples, with their dopant and annealing dependencies, are summarized in Table II.

### 3.3. Oxygen Recoil Detection

With further evidence establishing the 0.790 eV peak as arising from an oxygen-dependent center and the 1.018 eV peak as arising from the five vacancy complex, we are now in a position to apply this knowledge to the study of through-oxide arsenic implantations into silicon. In this study, bare (no grown oxide) float zone (oxygen-lean)  $\langle 111 \rangle$  n- and p-type wafers (123-81  $\Omega$  cm) were implanted with As ions to isolate the damage due to As implantation alone. To determine the effects of possible oxygen recoils, similar float zone crystals were implanted through a thin ( $\sim 500$  Å) layer of SiO<sub>2</sub> grown by dry thermal oxidation. As a control to test the effects of oxygen in-diffusion, an identical float zone sample was oxidized under the same conditions as the above wafers, and then the SiO<sub>2</sub> was removed by chemical etching prior to implantation.

TABLE II

Additional zero-phonon peaks seen from electron-irradiated silicon samples, listing the dopants added, if any, and the anneals (room temperature, 200°C, or both) for which they were observed.

| <u>Peak Energy (eV)</u> | <u>Samples and Anneals</u>                      |
|-------------------------|---|
| 0.950                   | C and O (RT, 200°C)                             |
| 0.912                   | C and O (RT, 200°C)                             |
| 0.900                   | Undoped (200°C), O (RT, 200°C)                  |
| 0.898                   | C and O (RT, 200°C), (RT, 200°C)                |
| 0.890                   | C and O (200°C), O (RT, 200°C), undoped (200°C) |
| 0.811                   | O (RT)  |
| 0.772                   | C and O (RT)                                    |
| 0.746                   | O (200°C)                                       |

Arsenic implantations of  $10^{13} \text{ cm}^{-2}$  were then performed at room temperature at 200 keV with typical beam current densities of  $0.05 \mu \text{ A/cm}^2$ . Wafers were oriented  $7^\circ$  from the beam direction to minimize channeling effects. Anneals below  $300^\circ\text{C}$  were performed in a controlled temperature oil bath, whereas anneals above  $300^\circ\text{C}$  were performed in a tubular furnace under flowing argon gas. All anneals in this study were of 30 minutes duration.

We examine first the luminescence peaks common to all spectra seen from the arsenic-implanted samples. These peaks occur at 1.018 eV (I1), 1.034 (I4), and 1.039 eV (I3). Of all the peaks examined in this study, the peak at 1.018 eV produced the greatest intensity. This peak grew in following the  $150^\circ\text{C}$  anneal, reached an intensity maximum following  $250^\circ\text{C}$  annealing, and then disappeared following  $350^\circ\text{C}$  anneals. The 1.018 eV peak appears at such great intensity that for the  $200^\circ\text{C}$  and  $250^\circ\text{C}$  annealing it completely dominates the recombination spectrum, appearing at approximately 40 times the intensity seen from the electron-irradiated samples (Table I). The intensity of this peak is such that we are able to identify its replication by the 18 meV TA, the 44 meV LA, the 53 meV LO, and the 59 meV TO phonons (Fig. 3.4). The I4 peak 1.034 eV appears as a higher energy shoulder on the 1.018 eV peak for the  $200^\circ\text{C}$  anneal, and then vanishes for higher temperature annealing. Peak I3 (1.039 eV) appears weakly for the  $300^\circ\text{C}$  anneal, reaches a maximum intensity for  $350^\circ\text{C}$ , and then anneals out following  $450^\circ\text{C}$  annealing. The annealing behavior of all three of these peaks is identical to that observed from samples implanted with other species [39], and indicates that these peaks are probably due to defects without impurity interaction or involving trace impurities common to silicon substrates.

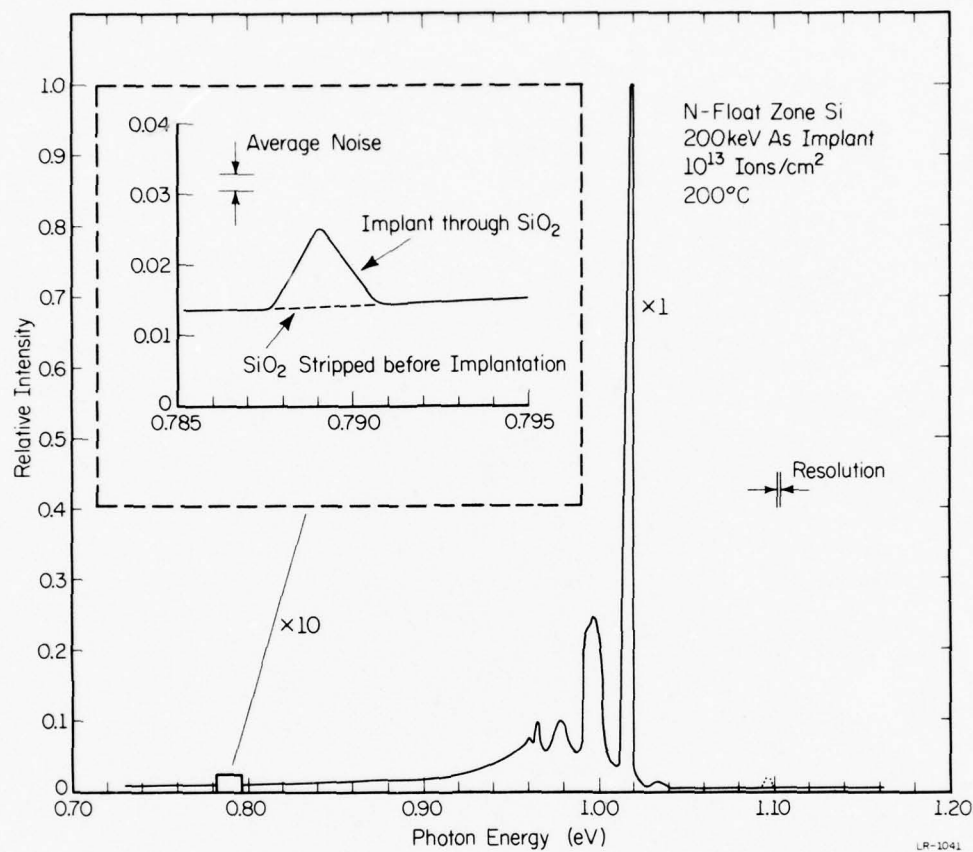


Figure 3.4. Photoluminescence from float zone Si following As implantation through an SiO<sub>2</sub> layer. The intense peak at 1.018 eV is due to a five vacancy cluster. The weak peak near 0.79 eV is due to an oxygen dependent defect. The 0.790 eV peak is absent in the sample implanted after removing the SiO<sub>2</sub> layer (broken line).

The most interesting results of this study come from examination of the 0.79 eV peak. This peak is seen from all the through-oxide implanted float zone (oxygen-lean) samples as well as from the bare surface implanted, pulled (oxygen-rich) substrates, but not from the bare surface implanted, float zone samples. Furthermore, the control float zone sample, from which the  $\text{SiO}_2$  was stripped before implantation, exhibited no oxygen-related luminescence (Fig. 3.4). The presence of this oxygen-dependent damage center for the float zone samples which had been implanted through a  $\text{SiO}_2$  layer, and not for the bare surface implantations nor for the control sample, shows conclusively the arsenic implantations through silicon dioxide result in oxygen recoils which enter the silicon substrate. These oxygen atoms participate in irradiation-induced defect complexes, including that related to the 0.79 eV luminescence. It is seen that oxygen in-diffusion during thermal growth of the  $\text{SiO}_2$  is insufficient to produce detectable luminescence following arsenic implantations.

The oxygen-dependent damage center causing the 0.790 eV luminescence anneals out at  $350^\circ\text{C}$ , so that this center is not itself responsible for the residual damage seen following through-oxide implantations. However, the presence of the 0.790 eV luminescence provides a direct detection of the oxygen recoil, and allows us to estimate an average oxygen concentration. The intensity of the 0.790 eV peak for the through-oxide implanted samples was half that of the arsenic-implanted pulled silicon sample. Since the oxygen content of pulled silicon is typically  $1 \times 10^{18} \text{ cm}^{-3}$  [47], by assuming the production rate of this defect is approximately the same for recoil-implanted oxygen as for grown silicon -- an assumption which may not be strictly justified [43] -- we estimate the "average" oxygen concentration



in the recoil-implanted layer to be on the order of  $5 \times 10^{17} \text{ cm}^{-3}$ . This estimate agrees well with the calculations of Moline *et al.* (Figure 5) if their concentration is scaled down to represent an implantation at the appropriate fluence.

The samples were annealed beyond  $400^{\circ}\text{C}$  to compare the spectra from the through-oxide implanted samples to those from the bare surface implants. The luminescence disappeared by  $500^{\circ}\text{C}$  and did not return even after  $1000^{\circ}\text{C}$  annealing, except for weak luminescence from the unimplanted substrate. For this reason, it is necessary to resort to other techniques to study the residual damage resulting from the through-oxide implants. The next chapters will examine and compare diffusion, electrical activation, and carrier mobility profiles for through-oxide and bare surface As implantations.

It should be noted in closing that MOS techniques have also been used to detect the oxygen recoil [47]. This method relies on the presence of surface states with well characterized energy levels in the silicon bandgap to provide defect identification. It is reported that the density of these surface states can be calibrated to yield a direct measure of oxygen recoil densities [47], the results of which are again in order of magnitude agreement with the calculations of Moline [7].

#### 4. ELEMENTAL PROFILING

Not all implanted ions become electrically active after annealing; the distribution of electrically active impurities differs from the total impurity distribution due to the presence of defects. Thus, the only accurate method of evaluating the activation of implanted ions is to compare their elemental profiles with the profile of electrically active impurities. This chapter will be concerned with the measurement of elemental depth profiles for implanted arsenic and recoil implanted oxygen and carbon. The next chapter will deal with measurement of the electrical properties of the implanted layers and comparison of the carrier and mobility profiles with the elemental impurity profiles.

##### 4.1. Sample Preparation

The wafers used for the determination of electrical and elemental profiling were all cut from  $\langle 100 \rangle$  - oriented boron doped single crystal silicon boules and all had commercially polished surfaces. One set of 5.2 to 7  $\Omega$ -cm Ventron substrates was implanted with 200 keV  $\text{As}^+$  to a fluence of  $1 \times 10^{15} \text{cm}^{-2}$  either into the bare surface or through approximately 840  $\text{\AA}$  of thermally grown  $\text{SiO}_2$  (1100°C, 30 min dry oxygen). The other set of wafers used in this study was Texas Instruments 9-14  $\Omega$ -cm pulled silicon. These wafers were implanted with 150 keV  $\text{As}^+$  to a fluence of  $5 \times 10^{15} \text{cm}^{-2}$ , either into the bare surface or through approximately 150  $\text{\AA}$  of silicon dioxide (900°C, 40 min dry oxygen). These samples were examined as implanted and also after selected annealing stages. All anneals in this study were performed in a quartz-lined tubular furnace under flowing argon gas. The samples

implanted to  $5 \times 10^{15} \text{ cm}^{-2} \text{ As}^+$  were also examined following redistribution by thermal oxidation. Both the bare surface and the through oxide implanted samples were subjected to either 5 minutes anneal in dry nitrogen, 2 hours wet oxidation, and 5 minutes anneal in dry nitrogen performed sequentially at  $900^\circ\text{C}$ , or 5 minutes anneal in dry nitrogen, 1 hour wet oxidation and 5 minutes anneal in dry nitrogen performed sequentially at  $1100^\circ\text{C}$ . Oxide thickness values quoted in this study were measured by ellipsometry. Table III summarizes the samples used for profile determination.

#### 4.2. Techniques for Elemental Profiling

Three techniques were available in this study for the determination of elemental profiles: Auger electron spectroscopy (AES) [48], glow discharge optical spectroscopy (GDOS) [49], and secondary ion mass spectroscopy (SIMS) [50]. These techniques all employ sputtering for sample sectioning, but differ in the ways in which the profile information is obtained. The mechanisms basic to these techniques will be briefly summarized below.

##### 4.2.1. Auger Electron Spectroscopy

In this technique, the sample to be examined is bombarded in high vacuum ( $< 10^{-10}$  torr) by a primary electron beam in the energy range of 1-10 keV. This primary beam causes a variety of secondary processes to occur, the most important of which, for this technique, is the creation of an atomic inner shell vacancy. The inner shell vacancy is filled by an outer shell electron, and this excess energy is carried away either by a photon or by an electron. If an electron is ejected, the radiationless transfer of energy is known as the Auger effect and the emitted electron as the Auger

TABLE III

Summary of samples used in this study to determine elemental and electrically active profiles. All substrates used were  $\langle 100 \rangle$  oriented p-type (boron-doped). Values quoted for oxide thickness were determined by ellipsometry.

| <u>Sample Type</u> | <u>Sample Resistivity</u> | <u>Pre-Implant Surface Condition</u> | <u>As Energy and Dose</u>                  | <u>Post-Implant Oxidation</u>     |
|--------------------|---------------------------|--------------------------------------|--|-----------------------------------|
| 1                  | 9 - 14 $\Omega$ -cm       | $\sim 150 \text{ \AA} \text{ SiO}_2$ | $5 \times 10^{15} \text{ cm}^{-2}$ 150 keV | None                              |
| 2                  | 9 - 14 $\Omega$ -cm       | $\sim 150 \text{ \AA} \text{ SiO}_2$ | $5 \times 10^{15} \text{ cm}^{-2}$ 150 keV | 2 hr $\text{O}_2$<br>@ 900°C      |
| 3                  | 9 - 14 $\Omega$ -cm       | $\sim 150 \text{ \AA} \text{ SiO}_2$ | $5 \times 10^{15} \text{ cm}^{-2}$ 150 keV | 1 hr wet $\text{O}_2$<br>@ 1100°C |
| 4                  | 9 - 14 $\Omega$ -cm       | Bare                                 | $5 \times 10^{15} \text{ cm}^{-2}$ 150 keV | 2 hr wet $\text{O}_2$<br>@ 900°C  |
| 5                  | 9 - 14 $\Omega$ -cm       | Bare                                 | $5 \times 10^{15} \text{ cm}^{-2}$ 150 keV | None                              |
| 6                  | 9 - 14 $\Omega$ -cm       | Bare                                 | $5 \times 10^{15} \text{ cm}^{-2}$ 150 keV | 1 hr wet $\text{O}_2$<br>@ 900°C  |
| 13                 | 5.2 - 7 $\Omega$ -cm      | $\sim 840 \text{ \AA} \text{ SiO}_2$ | $1 \times 10^{15} \text{ cm}^{-2}$ 200 keV | None                              |
| 14                 | 5.2 - 7 $\Omega$ -cm      | Bare                                 | $1 \times 10^{15} \text{ cm}^{-2}$ 200 keV | None                              |

electron [52]. The energy of this ejected electron is determined by the energy levels of the atom before and after ejection and hence is characteristic of the emitting atom. If the emitting atoms are close enough to the sample surface ( $3\text{-}20\text{\AA}$  [51]), the emitted electrons will suffer no inelastic collisions and thus retain their characteristic energy. Electrons emitted from greater depths will suffer inelastic collisions and thus lose their characteristic energies. These inelastically scattered Auger electrons combine with secondary electrons created by other mechanisms to form a broad continuum of electrons upon which the Auger peaks are superimposed. In this technique, the voltage of the electron analyzer is modulated by a few volts and lock-in detection is used to electronically differentiate the low level Auger peaks from the large continuous background [53]. Since only the Auger electrons emitted very close to the sample surface retain their characteristic energies, Auger spectroscopy is essentially a surface analytical technique. Depth profiles are obtained by gradually sputtering the sample surface to expose successively deeper regions to Auger analysis.

#### 4.2.2. Glow Discharge Optical Spectroscopy

In the GDOS technique, the sample to be examined is placed on the cathode of a dc glow discharge operated in the "abnormal glow" mode [54]. Atoms from the sample to be examined are ejected into the discharge by the sputtering gas (typically argon or krypton). Most of these sputtered atoms leave the sample surface as neutrals [55]. Some of these atoms are collisionally excited by secondary electrons escaping the cathode, and emit characteristic atomic luminescence. This luminescence is spectrally analyzed for the emission

characteristic of the element of interest, and the intensity of this luminescence is monitored with time. The GDOS process assumes that the emission intensity is proportional to the concentration of the element of interest in the substrate. Thus, emission intensity can be calibrated by use of suitable standards to yield impurity concentration, and the sputtering rate can be independently determined to yield a depth calibration. It is important to note that the element to be profiled is examined in a region outside the sample surface, thus reducing the influence of the substrate on the profile measurement to that due to the mechanisms of the atomic ejection during sputtering.

#### 4.2.3. Secondary Ion Mass Spectroscopy

The SIMS technique employs a focused primary ion beam to bombard the sample to be examined. Unlike GDOS, however, SIMS analyzes the small fraction of sample atoms that leave the surface as ions. These ions are extracted from the sputtered area and mass analyzed to provide the profile information. As in GDOS, however, the atomic concentration is produced as a direct result of the sputtering process; thus both GDOS and SIMS are inherently depth profiling techniques.

As with Auger spectroscopy, the escape depth for the analyzed particles, here the secondary ions, is  $10\text{-}20 \text{ \AA}$  [51]; however, the interpretation of SIMS data is significantly more complicated than is AES data. The reason for this complication lies in the various natures of the two techniques. Auger electrons are produced by atomic inner shell vacancies; the energies of these core levels are barely affected by chemical binding. Ionization, however,



occurs at the outer shell of electrons -- where all the chemical binding occurs. Thus the secondary ion yield can vary over several orders of magnitude for different elements in the same matrix or for the same element in different matrices [50]. Typically, the secondary ion yield of an element is much higher when it is sputtered from a bound state than is the case for a metallic state [50]. Thus, the presence of a reactive species in the sample enhances the secondary ion yield [50]. SIMS profiling typically employs either oxygen or cesium as the primary ion beam to stabilize the secondary ion yield at high levels. From basic chemistry, we recall that elements in the left of the periodic table (such as boron) tend to lose electrons to form complete outer shells; these elements thus prefer to form positive ions, and therefore oxygen (electron-accepting) primary beams are used to enhance secondary ion yields for these elements. On the other hand, elements from the right of the periodic table, such as arsenic, attract electrons to complete their outer shells and form negative ions; thus cesium (electron-donating) primary beams are used to enhance the secondary yields of these elements [56]. Nevertheless, by examining known concentrations of a particular element in a given matrix, calibration of sample concentration can be obtained, and as in GDOS the sputtering rate can be independently measured to provide a direct depth calibration.

#### 4.3. Results

##### 4.3.1. Auger Electron Spectroscopy

The Auger profiles of carbon, oxygen, and arsenic for the  $5 \times 10^{15} \text{ cm}^{-2}$  150 keV As-implanted samples are shown in Fig. 4.1. This data was obtained on a PHI system using a 5 keV coaxial electron gun.

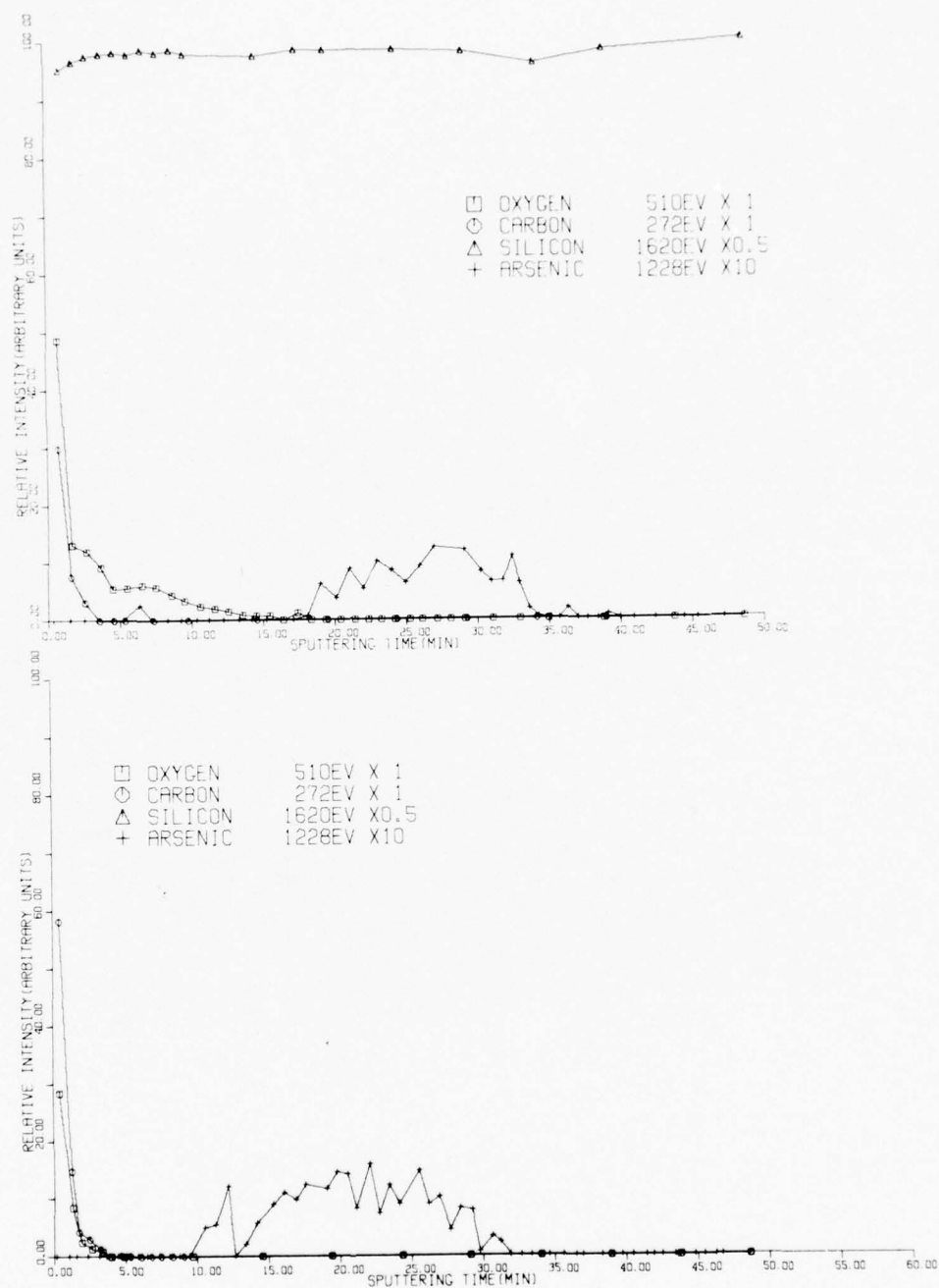


Figure 4.1. AES profiles for oxygen, carbon, arsenic and silicon, for unannealed  $5 \times 10^{15} \text{ cm}^{-2}$ , 150 keV As implants into bare surface (top) and through  $\text{SiO}_2$  (bottom). Notice linear intensity scales.

It can be seen that even for the peak As concentration of  $7 \times 10^{20} \text{ cm}^{-3}$  expected for the bare surface implant from LSS theory [19], the signal appears very noisy. Auger spectroscopy has very poor sensitivity (minimum detectable concentration 0.1% of matrix for elements with high atomic numbers [51]), although better sensitivity can be obtained for elements of lower atomic number, such as carbon and oxygen. Unfortunately, however, surface contamination by these common trace elements is unavoidable, so that Auger spectra always show strong initial carbon and oxygen signals even when the native oxide is chemically removed immediately prior to insertion in the Auger system. As the sample surface is sputtered to develop the depth profiles, a fraction of this surface layer is recoil-implanted into the substrate, thus producing a sloping profile from the surface that obscures the near surface carbon and oxygen profiles.

The only samples which showed sufficient arsenic concentrations to be easily measured were the samples wet oxidized at  $900^\circ\text{C}$  after the implant. For these samples, as the oxide is grown through the implanted layers, the arsenic accumulates at the interface. Apparently, at  $900^\circ\text{C}$  the diffusion of arsenic away from the interface is slower than the advance of the interface with the wet oxide growth, and thus the entire implanted arsenic dose is contained within a region only a few hundred Angstroms from the interface. Fig. 4.2 shows the Auger results for the  $5 \times 10^{15} \text{ cm}^{-2}$  150 keV  $\text{As}^+$  bare surface implant, after subsequent wet oxidation at  $900^\circ\text{C}$ . Of special interest is the sample from which the  $\text{SiO}_2$  had been chemically removed before examination. Of the three elemental profiling techniques used here, Auger spectroscopy is best suited for samples where the impurity distribution is peaked at the surface, since it does not require the establishment of an equilibrium in the

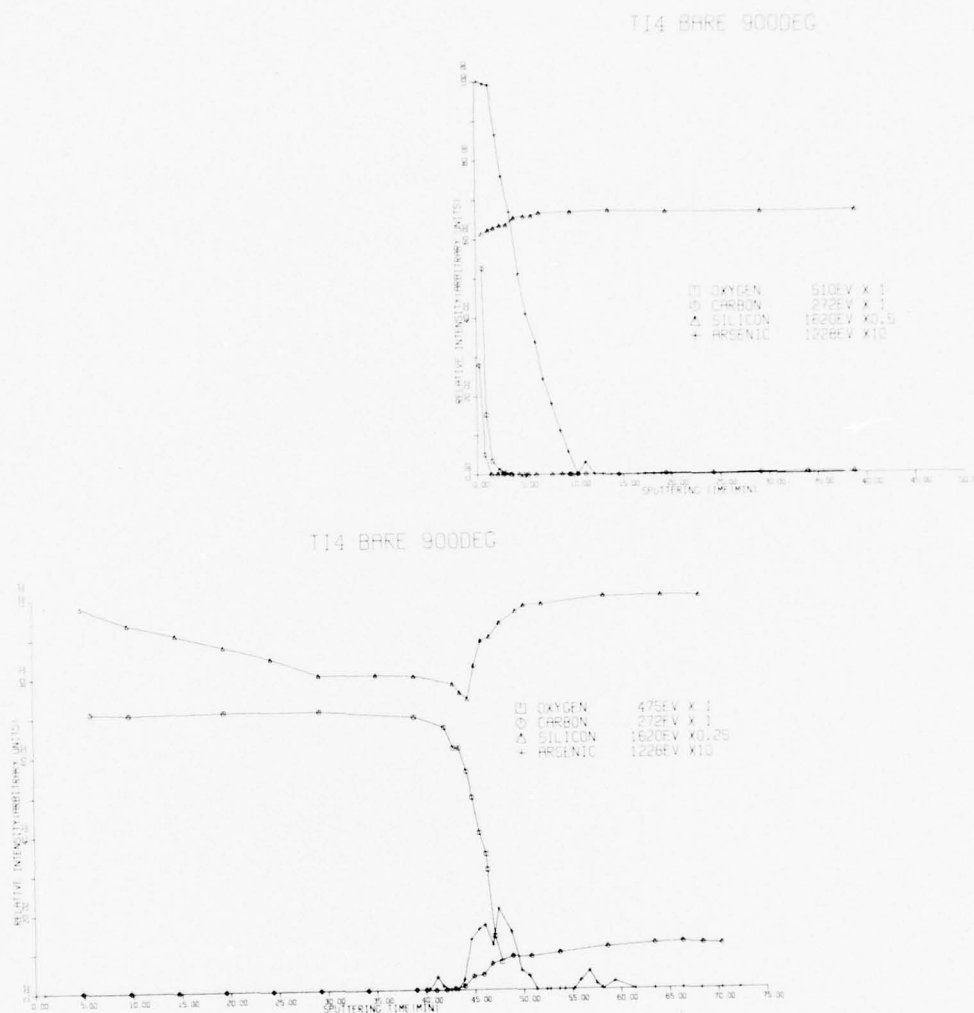


Figure 4.2. AES results for  $5 \times 10^{15} \text{ cm}^{-2}$ , 150 keV  $\text{As}^+$  implant following 2 hour wet oxidation at  $900^\circ\text{C}$ . For the top profile, the  $\text{SiO}_2$  was chemically removed prior to examination; for the bottom, the profiles were taken by sputtering through the  $\text{SiO}_2$  layer. Apparent in the lower profiles are the loss of intensity due to oxide charging effects and the decrease in depth resolution with sputtering time.

sputtering process before a reliable signal can be developed. Unfortunately, however, the Auger intensity obtained from these samples could not be converted into concentration due to lack of a standard sample with sufficiently high arsenic concentration. Additionally, Fig. 4.2 graphically illustrates a disadvantage common to all sputtering techniques; namely, the gradual loss of depth resolution with sputtering time due to nonuniform sputtering effects [57]. In addition, the sample examined through the thick oxide also exhibits a lower Auger yield due to trapped charges in the oxide repelling some of the emitted electrons. Due to all the problems listed above, intensity vs. time results were not calibrated to yield concentration vs. depth plots for the Auger analysis.

#### 4.3.2. Glow Discharge Optical Spectroscopy

Due to the presence of hydrocarbon pump oils in the discharge chamber, the GDOS technique is unable to provide elemental profiles for carbon or oxygen. The elemental As implants are shown in Fig. 4.3 for the bare surface and through oxide implanted samples. The bare surface implant shows a projected range of  $820 \pm 20 \text{ \AA}$  with a standard deviation for the Gaussian approximation of  $335 \pm 20 \text{ \AA}$ . These values compare well with compiled values for As range statistics of  $842 \text{ \AA}$  projected range and  $292 \text{ \AA}$  standard deviation [19]. It is also seen from this figure that the detection limit for arsenic using this technique is approximately  $3 \times 10^{19} \text{ cm}^{-3}$ . In the GDOS technique, the sensitivity is limited by the sputtering rate [58]; however, faster sputtering rates increase depth uncertainty for shallow profiles such as these. It was determined during this study that a sputtering rate of  $50 \text{ \AA/minute}$

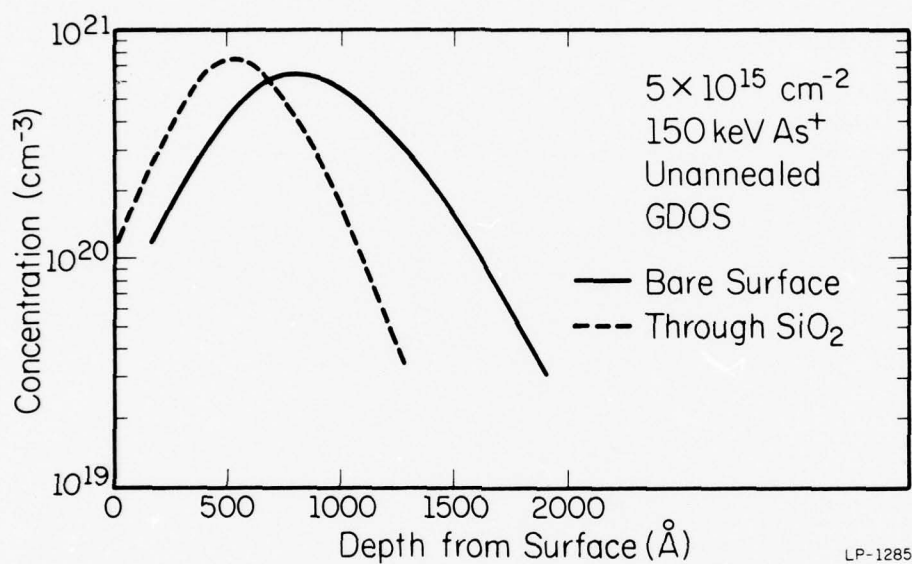


Figure 4.3. Arsenic profiles by GDOS for  $5 \times 10^{15} \text{ cm}^{-2}$   $150 \text{ keV As}^+$  implants. The solid line represents the profile resulting from a bare surface implant while the broken line represents the profile resulting from implants through an approximately  $150 \text{ \AA}$  thick  $\text{SiO}_2$  layer.



produced optimal results.

When the glow discharge is initiated, there is a temporary period of instability until an equilibrium sputtering rate is attained. This initial instability could result in an uncertainty in depth calibration for the GDOS process if the glow discharge were initiated on the sample surface. To avoid these problems, a thin (approximately 200 Å) nickel layer is evaporated over the sample surface, and the discharge is initiated on this nickel layer. Nickel was chosen for this layer due to its excellent adhesion to silicon, its faster sputtering rate than the silicon substrate (thus avoiding cone formation [57]), and its excellent mechanical properties (i.e. scratch resistance). The present GDOS system employs two monochromator and detection systems operating simultaneously. One system monitors the intensity of the element to be profiled, and the second monitors substrate (i.e. silicon) intensity. This second system indicates the time at which the silicon surface is reached and provides a monitor of the uniformity of the substrate sputtering rate.

Problems were encountered in measuring the profiles of the other arsenic-implanted samples. Difficulties in depth calibration were encountered, however, for the 150 keV  $\text{As}^+$  implants annealed to 1000°C, and uniform sputtering rates could not be obtained for the sample redistributed by thermal oxidation. Unfortunately, not enough material from 200 keV  $\text{As}^+$  implants was available to permit GDOS measurement.

#### 4.3.3. Secondary Ion Mass Spectroscopy

Since only a small amount of sample area is consumed in the SIMS technique (approximately 0.01 mm<sup>2</sup> profile) all the samples mentioned in Table III

were profiled by the SIMS technique. On the SIMS system used in this study (an AEI model IM 20 modified by the addition of a cesium ion source) it was impossible to simultaneously profile more than one element; thus profiles of different elements in the same sample are obtained by consecutive runs from areas immediately adjacent on the sample examined. At least two craters are necessary for every sample examined--one to measure the arsenic intensity and the other to measure silicon intensity. This procedure was required, since ion yield varies from one position in the sample holder to the other, due to geometric factors. These factors were fairly constant for each particular sample position in the holder, and thus could be cancelled by normalizing the observed arsenic intensity to the intensity of the silicon substrate.

The SIMS technique yields plots of ion yield vs. sputtering time, as shown in Fig. 4.4. These plots were then calibrated to yield graphs of concentration vs. depth using a procedure described below. Arsenic yield normalized to the silicon yield was calibrated by assuming that the peak value obtained for the  $5 \times 10^{15} \text{ cm}^{-2}$  150 keV bare surface implant was  $7.0 \times 10^{20} \text{ cm}^{-2}$  (the value given by LSS calculations [19]). This value agrees very closely with the GDOS result shown in Fig. 4.3. Depth scales were calibrated through the use of a Sloan Dektak to determine crater depths for known sputtering times, and thus determine average sputtering rates for four of the samples examined ( $5 \times 10^{15} \text{ cm}^{-2}$  150 keV  $\text{As}^+$  implants into bare surface or through silicon dioxide for the  $600^\circ\text{C}$  and  $1000^\circ\text{C}$  anneals). Since the measurement of a crater 100  $\mu\text{m}$  on a side with the Sloan Dektak is difficult at best, the sputtering rate was also calibrated by assuming that the peak of the

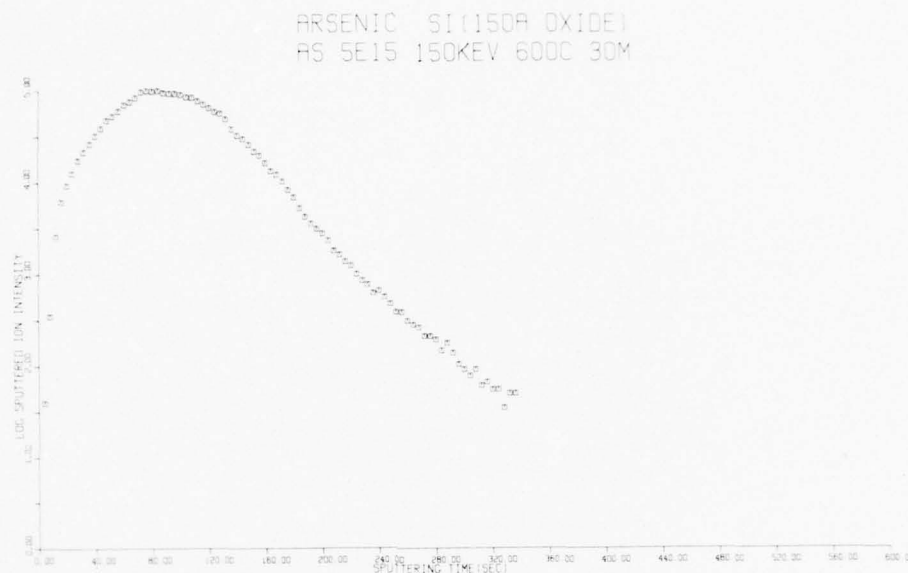


Figure 4.4. Plot of sputtering  $^{75}\text{As}^-$  secondary ion yield (log scale) vs. sputtering time following  $600^\circ\text{C}$  annealing of  $5 \times 10^{15} \text{ cm}^{-2}$  150 keV  $\text{As}^+$  implant through approximately 150 Å of  $\text{SiO}_2$ . This raw data was converted to yield arsenic concentration profiles through the use of calibration procedures discussed in the text.

arsenic distribution for the 150 keV bare surface arsenic implant occurred at the LSS value of  $842 \text{ \AA}$  [19]. The difference between these two measurement techniques was less than 10% for those samples in which crater depth could be unambiguously determined.

The plots of arsenic concentration vs. depth obtained by this technique are shown in Figs. 4.5-4.12. An arsenic profile for the  $600^{\circ}\text{C}$  annealed sample, for which there is negligible diffusion from the initial implanted profile, is shown in Fig. 4.5. Comparing these results with the profiles obtained following  $1000^{\circ}\text{C}$  anneal (Fig. 4.6), we observe of the effects of concentration dependent diffusion of arsenic in silicon [1,59] for the doses used here. This effect is due to field-aided diffusion [3]. Because of the concentration dependent diffusion, the peak of the implanted distribution, having a higher arsenic concentration, diffuses more rapidly and eventually overtakes the tail of the distribution which has a lower arsenic concentration and thus lower diffusion coefficient. This produces an abrupt arsenic profile, which is extremely useful for emitter formation in bipolar transistors [1]. This effect is also seen for the samples implanted through an approximately  $150 \text{ \AA}$  thick  $\text{SiO}_2$  layer, where the peak of the arsenic implant is inside the silicon substrate. The effect is not easily observable for the samples implanted through  $840 \text{ \AA}$  of  $\text{SiO}_2$ , where the arsenic distribution was peaked near the silicon-silicon dioxide interface. In fact, for the latter case the  $1000^{\circ}\text{C}$  profile (Fig. 4.10) is even shallower than that of the  $600^{\circ}\text{C}$  annealed sample (Fig. 4.9). This result for implants through the thicker silicon dioxide layer suggests that the thin oxide layers grown were inadvertently of non-uniform thickness. Subsequent investigation by GDOS, SIMS,

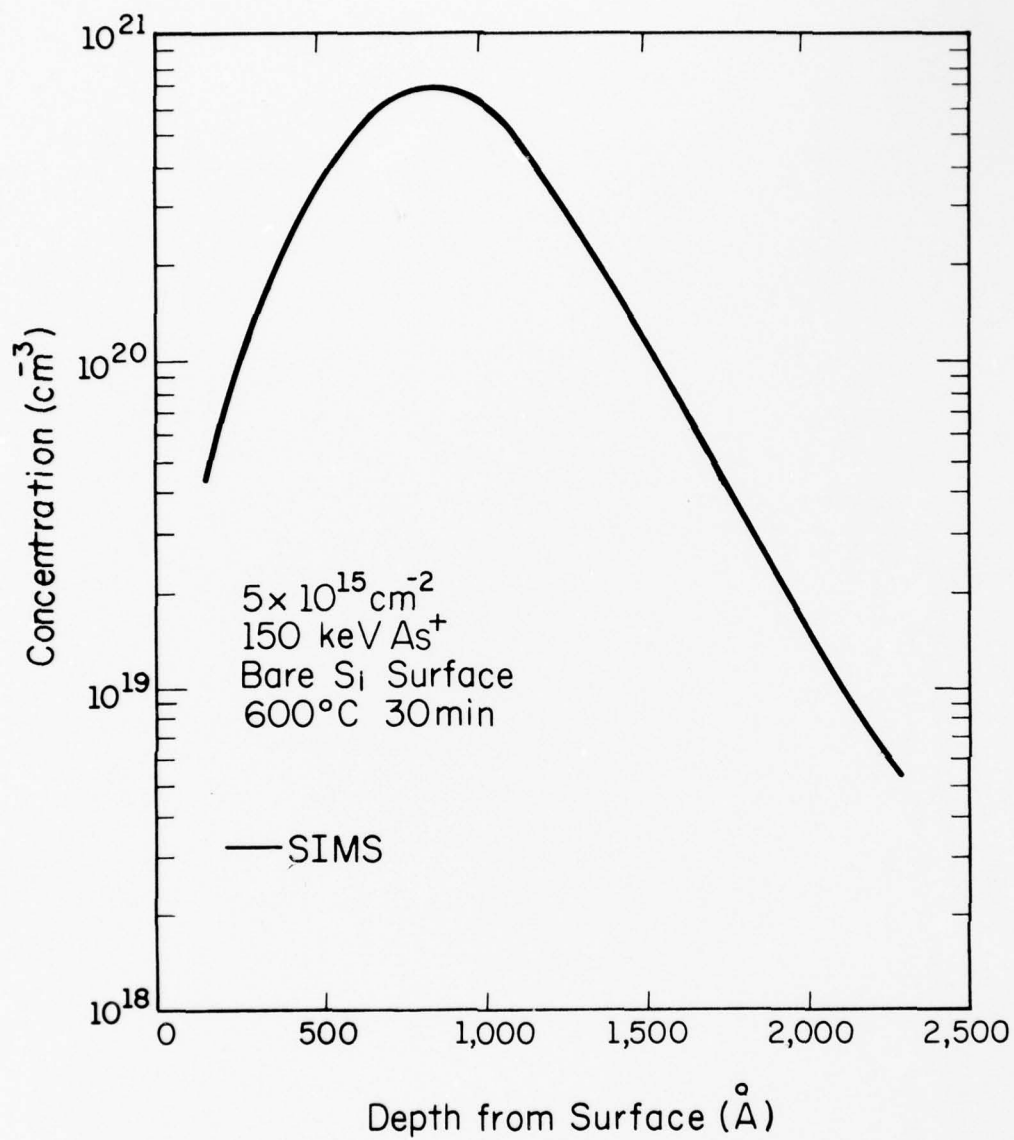


Figure 4.5. Arsenic profile by secondary ion mass spectroscopy following 600°C 30 minute annealing of  $5 \times 10^{15} \text{ cm}^{-2}$  150 keV  $\text{As}^+$  bare surface implant.

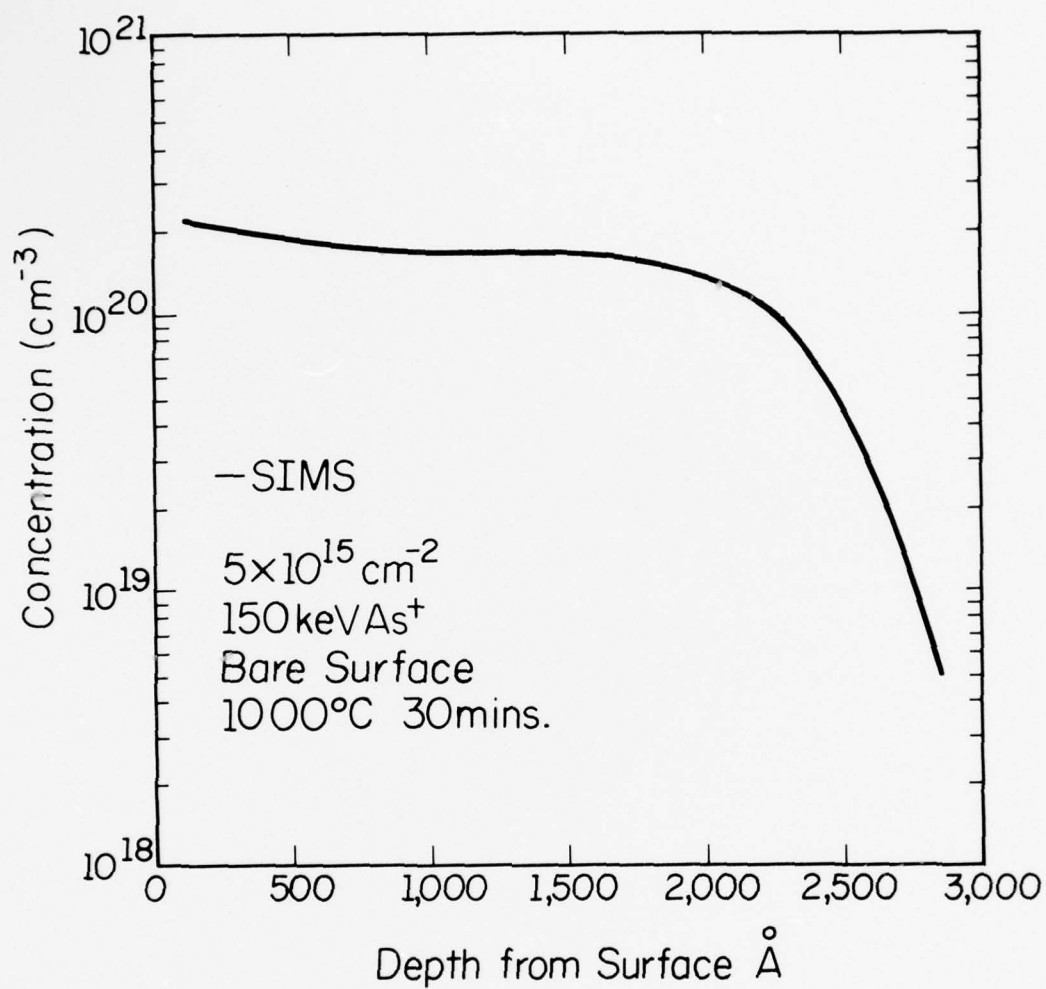


Figure 4.6. Arsenic profile by secondary ion mass spectroscopy following  $1000^\circ\text{C}$  30 minute annealing of  $5 \times 10^{15} \text{ cm}^{-2}$  150 keV  $\text{As}^+$  bare surface implant.



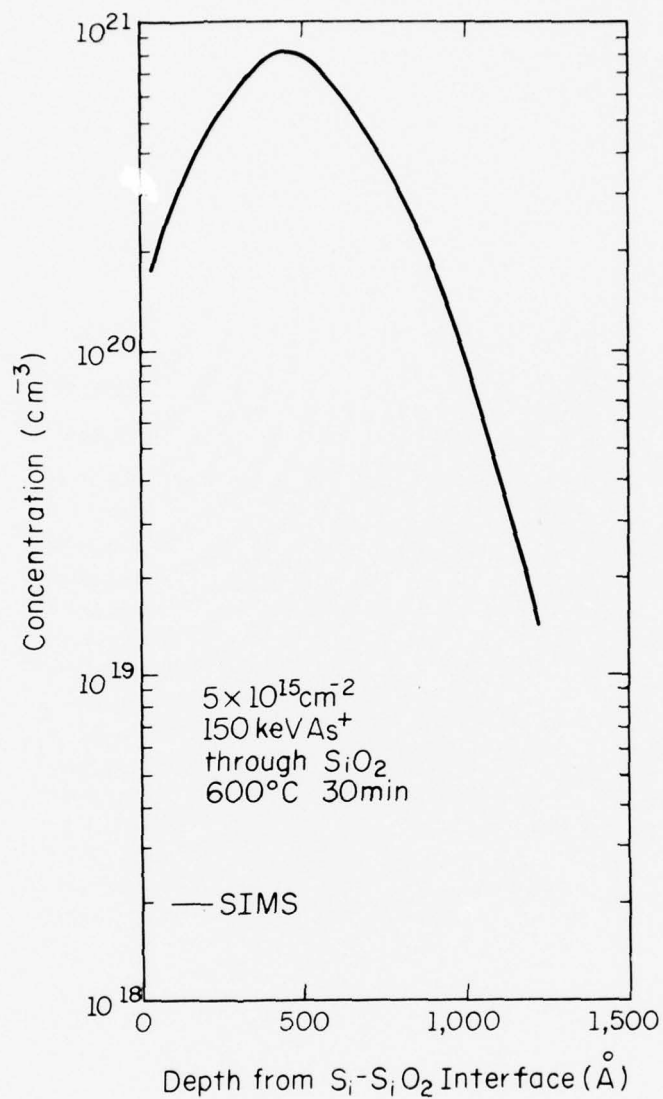


Figure 4.7. Arsenic profile in silicon by secondary ion mass spectroscopy following  $600^\circ\text{C}$  30 minute annealing of  $5 \times 10^{15} \text{cm}^{-2}$   $150 \text{ keV As}^+$  implant through an approximately  $150 \text{ \AA}$  thick  $\text{SiO}_2$  layer.

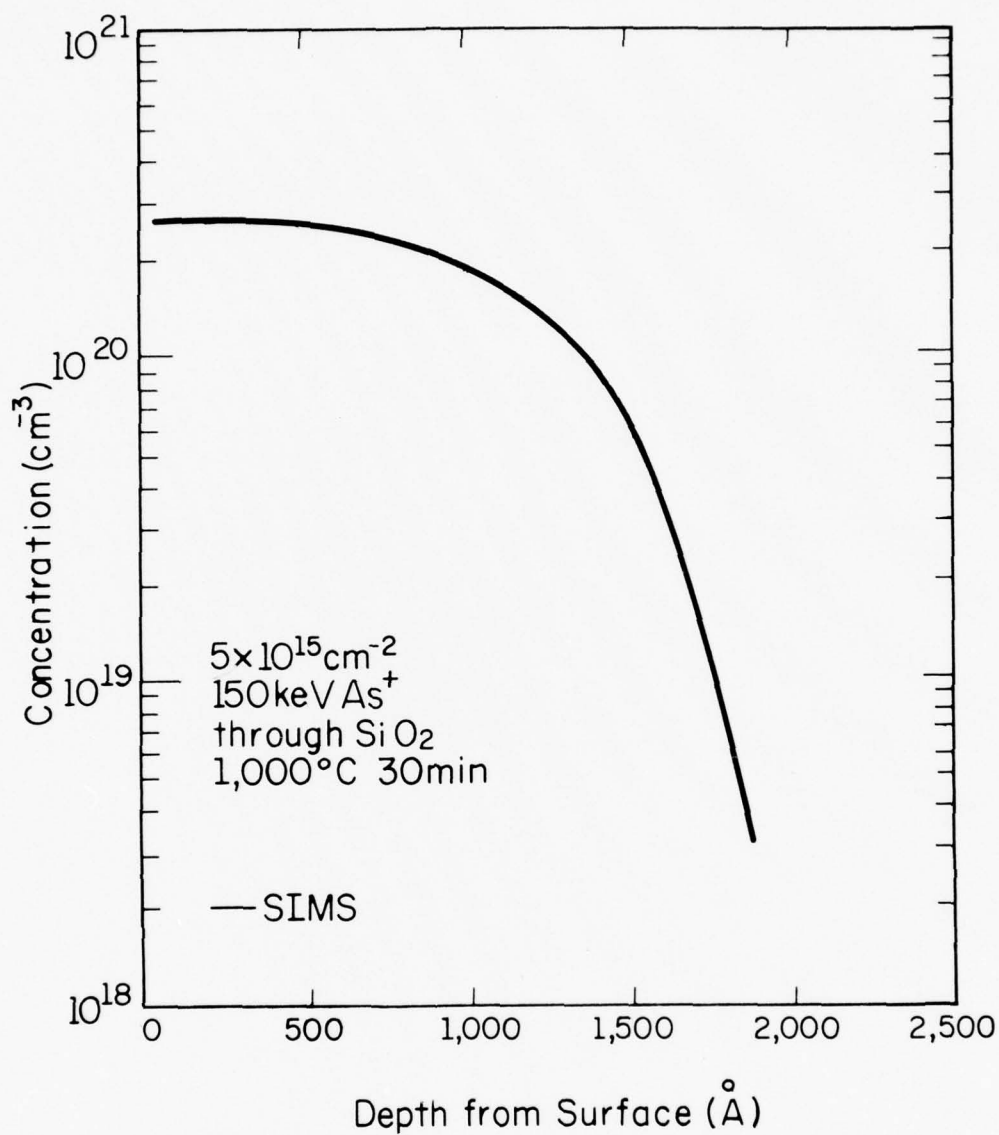


Figure 4.8. Arsenic profile in silicon by secondary ion mass spectroscopy following  $1000^\circ\text{C}$  annealing of  $5 \times 10^{15} \text{ cm}^{-2}$   $150 \text{ keV As}^+$  implant through an approximately  $150 \text{ \AA}$  thick  $\text{SiO}_2$  layer.

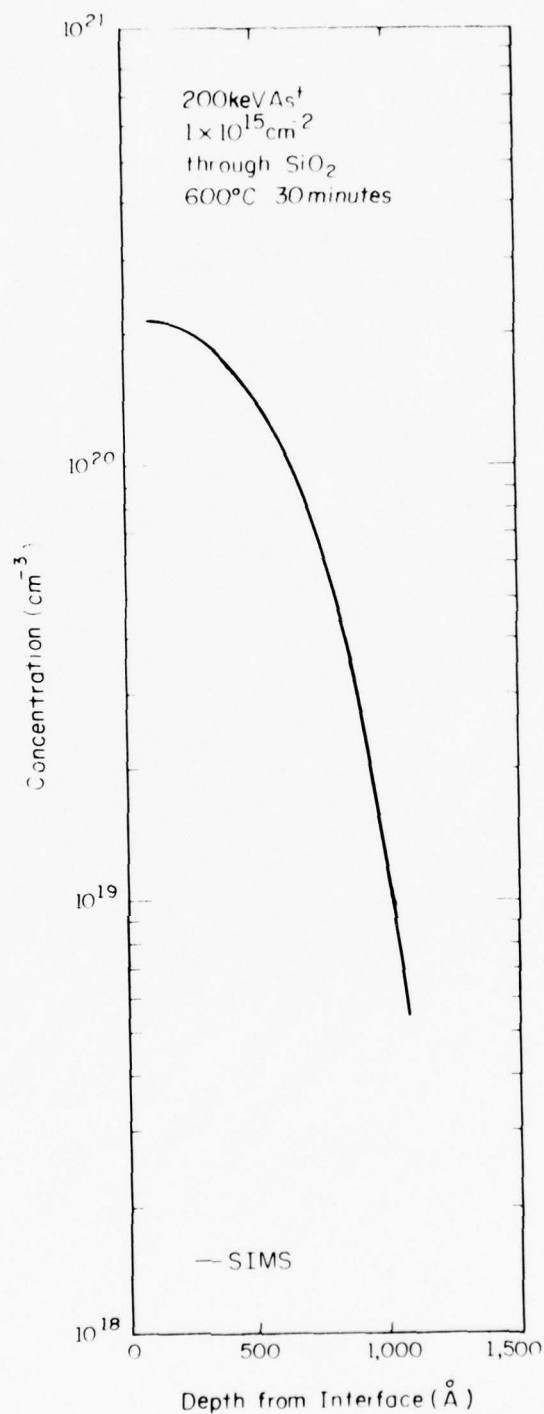


Figure 4.9. Arsenic profile in silicon by secondary ion mass spectroscopy following 600°C 30 minute annealing of  $1 \times 10^{15} \text{ cm}^{-2}$  200 keV As<sup>+</sup> implant through an approximately 840 Å thick SiO<sub>2</sub> layer.

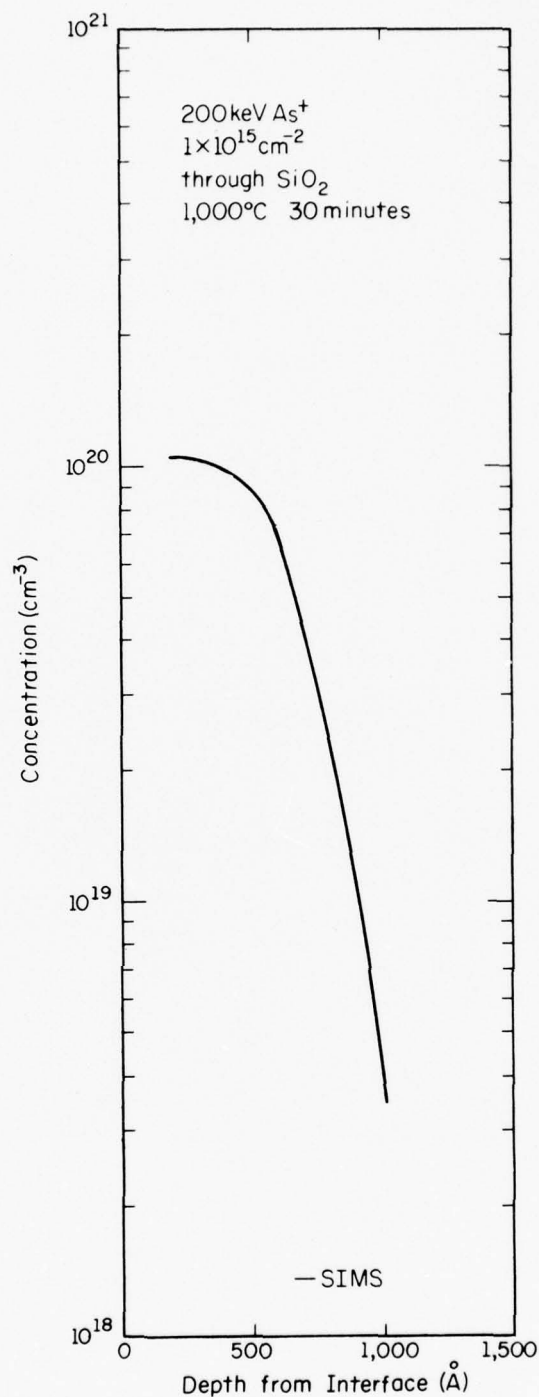


Figure 4.10. Arsenic profile in silicon by secondary ion mass spectroscopy following 1000°C 30 minute annealing of  $1 \times 10^{15} \text{ cm}^{-2}$  200 keV As<sup>+</sup> implant through an approximately 840 Å thick SiO<sub>2</sub> layer.

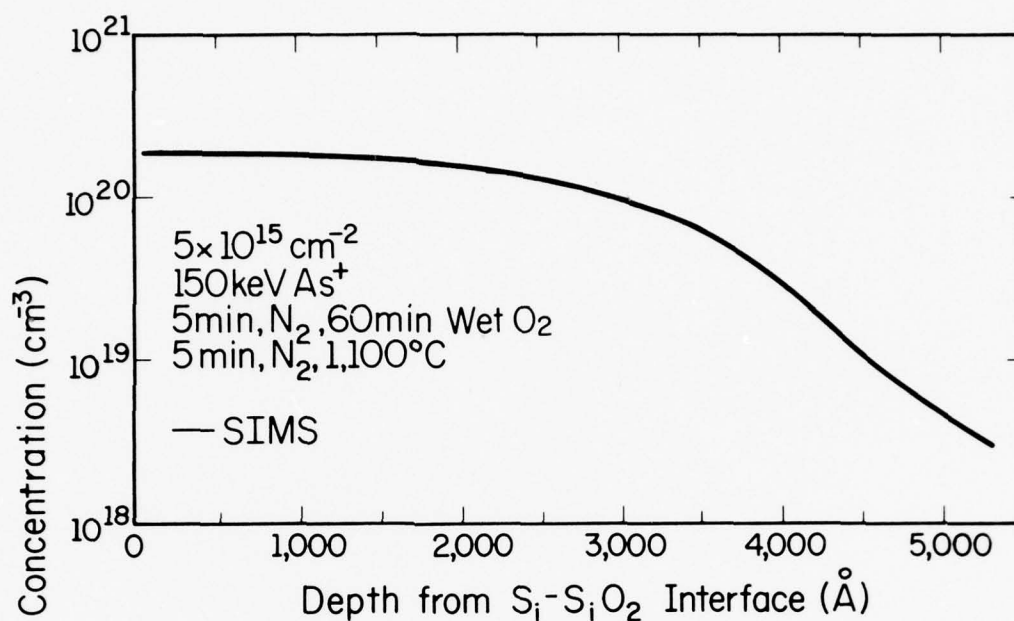
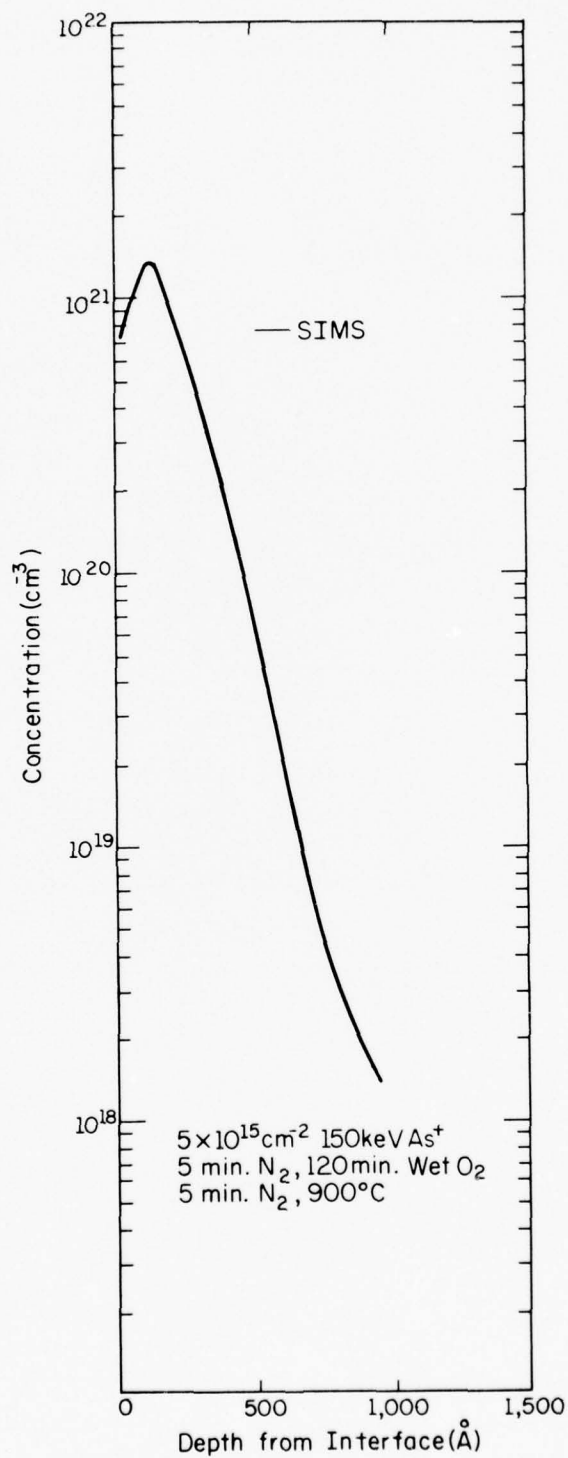


Figure 4.11. Arsenic profile in silicon by secondary ion mass spectroscopy for  $5 \times 10^{15} \text{ cm}^{-2}$   $150 \text{ keV As}^+$  implant following redistribution by wet oxidation for 60 minutes at  $1100^\circ\text{C}$ . Profiles are identical for implants into bare surface and implants through approximately  $150 \text{ \AA SiO}_2$ .

Figure 4.12. Arsenic profile in silicon by secondary ion mass spectroscopy for  $5 \times 10^{15} \text{ cm}^{-2}$  150 keV  $\text{As}^+$  implant following redistribution by wet oxidation for 120 minutes at  $900^\circ\text{C}$ . Profiles are identical for implants into bare surface and implants through approximately  $150 \text{ \AA}$   $\text{SiO}_2$ .





and electrical measurements described in the next chapter indicated variations in the projected ranges for arsenic implanted through the silicon dioxide layers. These variations were greater than the uncertainties of any of the depth profiling techniques used. Such variation in the arsenic distributions was not seen for the bare surface implants, and thus could only have arisen from variations in the thickness of the grown silicon dioxide layers, since the bare surface and through-oxide implanted layers were implanted simultaneously. The variation in projected ranges for the through-oxide implanted samples over various regions of the implanted wafer makes it impossible to quantitatively compare the diffusion of through-oxide implanted silicon with bare surface implanted silicon.

It is interesting to observe the effects of thermal oxidation on the arsenic implanted profiles. During oxide growth the arsenic is rejected by the growing oxide region [3], and instead accumulates inside the silicon near the silicon-silicon dioxide interface. The accumulated arsenic can also diffuse from the interface into the bulk at the oxide growth temperature, and the two mechanisms of segregation and diffusion combine to produce the final arsenic distribution. At  $900^{\circ}\text{C}$  the wet oxidized layer grows at a faster rate than the arsenic diffuses away from the interface, so that the entire arsenic dose is contained within a few hundred angstroms of the surface. At  $1100^{\circ}\text{C}$  the situation is reversed, and the arsenic diffuses away from the interface at a faster rate than the silicon-silicon dioxide interface advances. Since the oxide layers incorporate the entire implanted arsenic distributions, it is no surprise that the final arsenic distributions are nearly identical for the bare surface and through-oxide implanted samples.

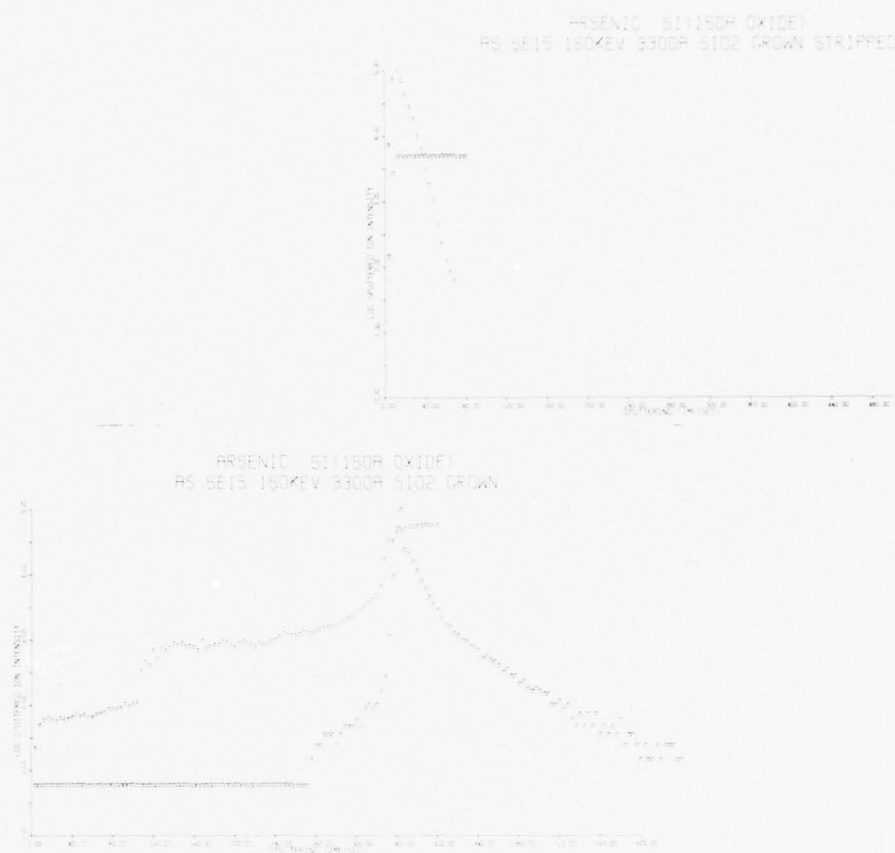


Figure 4.13. SIMS results for  $5 \times 10^{15} \text{ cm}^{-2}$ , 150 keV  $\text{As}^+$  implants following 2 hour wet oxidation at  $900^\circ\text{C}$ . Arsenic profile (dots) was determined after the  $\text{SiO}_2$  layer was chemically removed; on the bottom the arsenic profile (squares) was determined by sputtering through the  $\text{SiO}_2$  layer. Apparent in the lower profiles is a decrease in depth resolution with sputtering time and a loss of intensity due to oxide charging effects.

In examining the profiles of the 900°C oxidized samples, we notice the limitation of the SIMS technique for near surface analysis. Whereas the arsenic distribution is peaked at the interface, the SIMS technique shows a peak located away from the interface, due to a lack of chemical equilibrium between the primary ion beam and the substrate for the initial stages of sputtering [57]. This effect reduces the initial secondary ion yield, for the reasons discussed in section 4.2.3. By comparing the profiles obtained from sputtering through the  $\text{SiO}_2$  layer with those obtained when the  $\text{SiO}_2$  is chemically removed prior to examination (Fig. 4.13), we again see profile broadening and reduction in ion yield, as in the Auger spectroscopy results.

Finally, it should be noted that one anomaly occurred in the measurement of the sample redistributed by thermal oxidation at 1100°C following implantation. The profiles obtained for samples 3 and 6 were of the same shape, but the absolute intensity for sample 6 (bare surface) was 55% larger than that obtained from sample 3 (through-oxide implant). It has previously been observed that the secondary ion yield from crystalline samples is strongly orientation-dependent [57], and it appears likely that for sample 6 the primary cesium beam in the SIMS system was incident upon a preferred crystalline direction. However, the calibration for sample 6 led to an integrated arsenic intensity approximately 50% greater than the total dose, while the integrated intensity for sample 3 agrees with the ion dose to within experimental uncertainty (approximately 10%). For this reason, the results obtained for sample 6 were scaled to correspond to the results obtained for sample 3.

#### 4.4. Comparison of Techniques

The results obtained in section 4.3 allow us to make several observations about the relative advantages of each of the various profiling techniques.

Auger spectroscopy excels in the measurement of near-surface features, but suffers from poor impurity detection limits (approximately  $4 \times 10^{20} \text{ cm}^{-3}$  for arsenic). AES has excellent lateral resolution [48] (which is not examined in this study) and the capability to monitor more than one element simultaneously. The GDOS technique is well suited to the measurement of implanted profiles, and provides easier concentration calibration than any of the other techniques. The As detection limit for GDOS is between that for SIMS and AES. By using multiple analysis and detection schemes the GDOS technique can simultaneously monitor the presence of several elements in the sample simultaneously. While not of direct concern for this study, GDOS is also the least expensive depth profiling technique of the three examined in this study. The GDOS technique suffers, however, in lack of lateral resolution and the amount of sample area consumed (approximately  $0.5 \text{ cm}^2$  per profile). Also, in GDOS, it is not possible to examine samples implanted through an oxide layer without first chemically removing the oxide layer. Glow discharge optical spectroscopy is a technique still in its infancy, and as more work is put into the development of this technique it should be possible to overcome the problems encountered in profiling the annealed samples.

Finally, we consider SIMS. This technique is the most sensitive and also the most expensive of the techniques employed here. The SIMS system used in this study detects arsenic concentrations as low as  $1 \times 10^{17} \text{ cm}^{-3}$  using a cesium ion source [56], although a distinction must be made between ultimate sensitivity and the dynamic range of the instrument. The SIMS system used here can only detect changes in impurity concentration over three orders of magnitude, below which impurities sputtered from the sides of the crater walls create a background ion count above the ultimate detection limits of the system. The SIMS technique excels at producing the shape of the dopant vs. depth relationship; however, the calibration of impurity concentrations and depth scales requires care and considerable effort.



## 5. ELECTRICAL MEASUREMENTS

In an ion implanted sample both the carrier concentration and carrier mobility vary with depth from the sample surface; thus any electrical measurement of an implanted layer represents a weighted average over the depth distribution of implanted ions. By combining electrical measurements with successive layer removal, it is possible to isolate the contribution from each layer and determine its average carrier concentration and mobility. By comparing such measurements on samples that have been implanted through thin oxide layers with samples that have been implanted into bare surfaces under the same conditions, we obtain a direct measurement of the effects of the recoil damage on the electrical properties of the implanted layers. In addition, these measurements allow a direct examination of the diffusion and activation of ion implanted arsenic in silicon.

### 5.1. Experimental Procedure

The samples used for this part of the study were identical to those described in section 4.1 and summarized in Table III. Prior to annealing, the samples were cleaned with organic solvents and  $H_2O_2$ -based cleaning solutions [60]. All anneals performed were of 30 minutes duration under flowing argon gas. Following annealing, the samples were cleaved into approximately 100 mil squares, cleaned, and then etched in a buffered-HF solution. Contacts of Au(1% Sb) were then evaporated onto the front surface through a shadow mask to define a van der Pauw [61] pattern. These contacts were annealed at temperatures between  $400^{\circ}C$  and  $425^{\circ}C$  (well above the  $370^{\circ}C$  Au-Si eutectic [62]) for approximately 20 seconds and then quenched in distilled

water. This procedure forms alloy junctions that penetrate the implanted layers. Following contact formation, the samples were mounted over a different shadow mask, held in place with glycol phthalate, and a groove pattern was sandblasted into the surface to minimize the effects of finite contact size [63]. In addition to providing positive location, the glycol phthalate also protected the sample surface during the sandblasting. The completed sample (Fig. 5.1) was next removed from the mask, cleaned, and mounted on nylon disks using GE 7031 varnish and aligned to provide proper registration in the sample holder (Fig. 5.2). Electrical contact to the sample was made with spring loaded non-magnetic Pogo stick contacts made by the Pylon Co.

Hall effect and sheet resistivity measurements are made using a double ac Hall effect system, described elsewhere [64]. In this method, the magnet is excited with current of one frequency (250 Hz) and the sample with current of a different frequency (1 kHz). The Hall voltage then appears at the difference frequency. Since the driving frequencies are phase locked, one measures the heterodyne component using a lock-in technique as shown in the schematic diagram (Fig. 5.3), providing excellent noise suppression. For the van der Pauw style double ac method, the sheet mobility and sheet carrier concentration are given by [64]

$$\rho_s = \frac{\pi}{\ln 2} \left( \frac{R_{ABCD} + R_{BCDA}}{2} \right) f \left( \frac{R_{ABCD}}{R_{BCDA}} \right) \quad (5.1)$$

and

$$N_s = \frac{1}{R_s e} \quad (5.2)$$

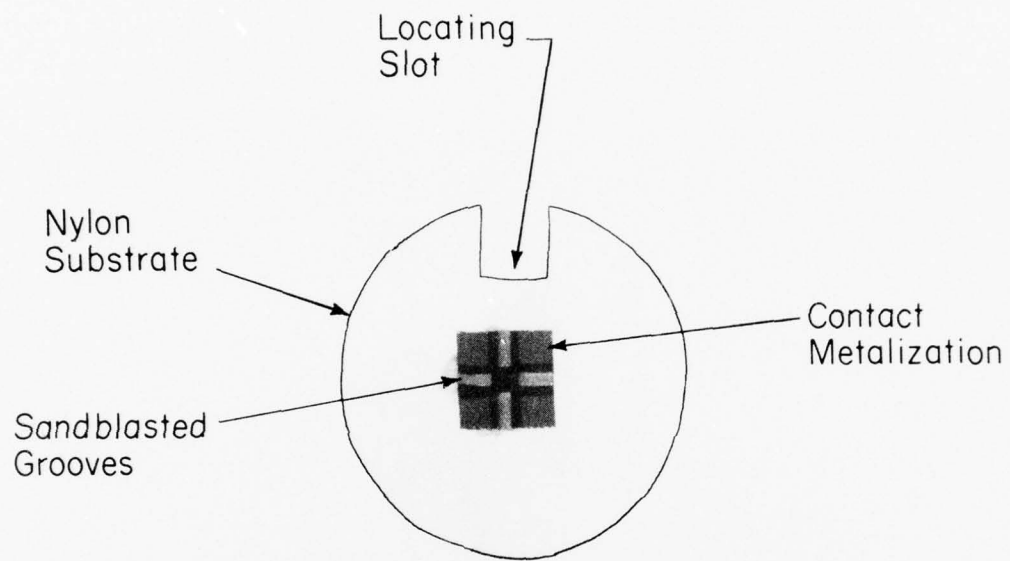


Fig. 5.1. Photograph of a typical van der Pauw sample on a nylon substrate. The contacts are isolated by sandblasted regions. The locating slot on the substrate enables proper positioning of the sample in the double ac sample holder.

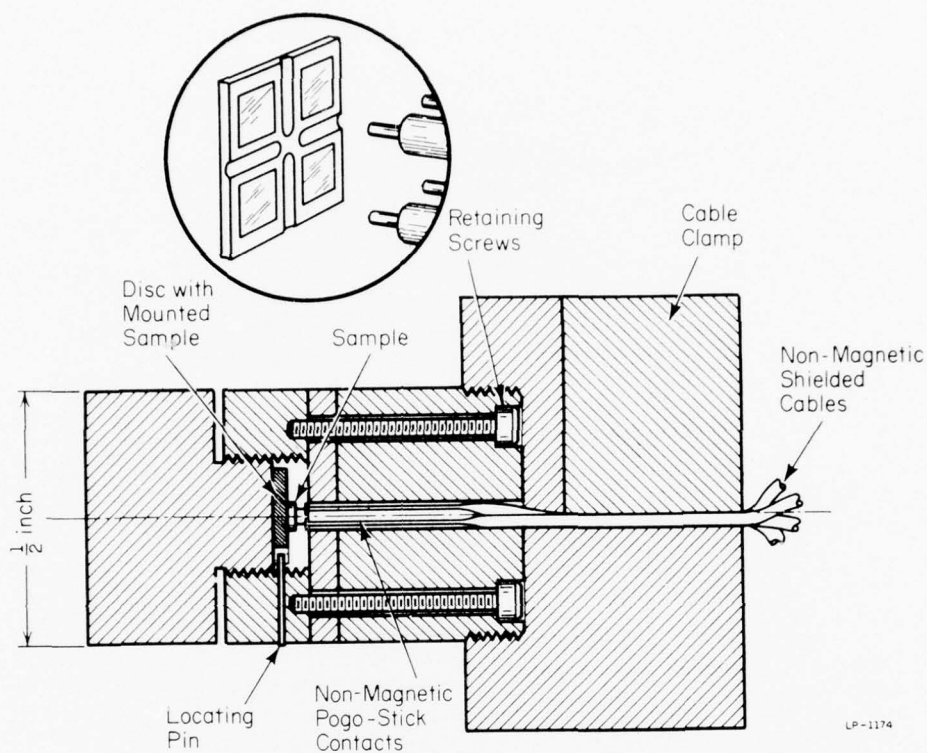
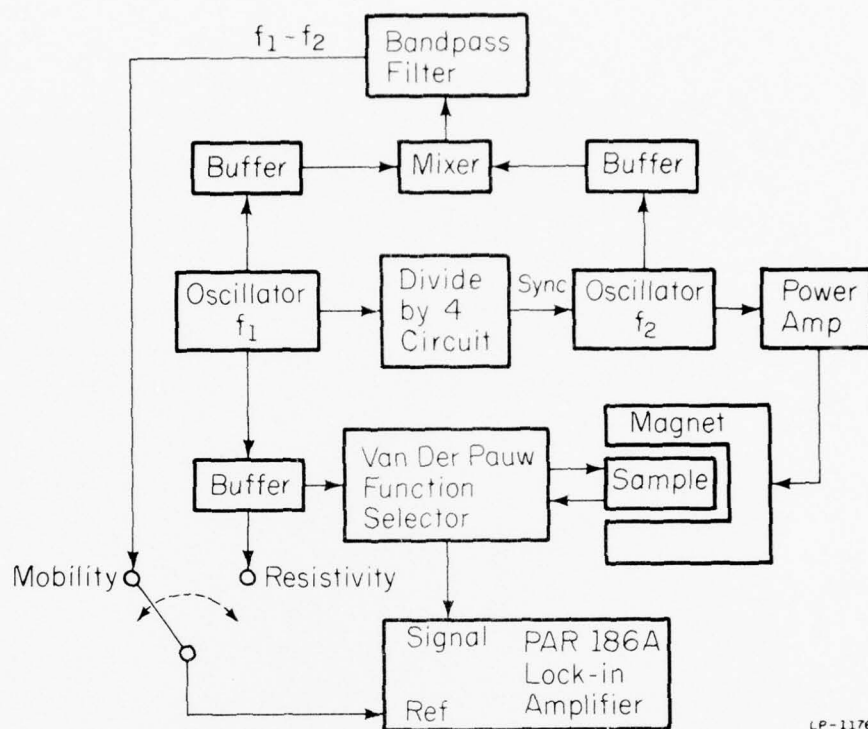


Figure 5.2. Cross sectional view of the sample holder which is placed inside the magnet for double a-c Hall effect measurements. The inset shows an enlarged view of the sample and spring mounted contacts in the holder (after McLevige *et al.* [64]).



LP-1176

Figure 5.3. Block diagram of double a-c Hall effect system (after McLevige et al. [64]).

with

$$R_s = \frac{\sqrt{2} \Delta V_{BDAC}(\text{rms})}{B(\text{rms}) \times I(\text{rms})} \quad (5.3)$$

If the contacts are labeled clockwise,  $R_{ABCD}$  represents the voltage developed across contacts A and B when unit current is passed through contacts C and D. The other symbols are defined similarly.

In the same way,  $\Delta V_{BDAC}$  represents the voltage measured at the heterodyne frequency across contacts B and D for unit current through contacts A and C under the ac magnetic field  $B(\text{rms})$  (202 gauss for the present system).

Here  $f\left(\frac{R_{ABCD}}{R_{BCDA}}\right)$  is a tabulated factor given by van der Pauw [61] and  $e$  is the electronic charge. By successively removing layers of thickness  $d_j$ , the average carrier concentration and mobility of the layer can be determined by measuring the sheet resistivity  $\rho_{s_j}$  and sheet Hall coefficient  $R_{s_j}$  before stripping and the same quantities after stripping (i.e.,  $\rho_{s_{j-1}}, R_{s_{j-1}}$ ). The average mobility in the layer is given by

$$\mu_j = \frac{R_{s_j} / \rho_{s_j}^2 - R_{s_{j-1}} / \rho_{s_{j-1}}^2}{1 / \rho_{s_j} - 1 / \rho_{s_{j-1}}} \quad (5.4)$$

and the average carrier concentration is given by [27]

$$n_j = \frac{1 / \rho_{s_j} - 1 / \rho_{s_{j-1}}}{e d_j \mu_j} \quad (5.5)$$

The derivation of these equations based on an equivalent circuit model is presented in the Appendix; however, these can also be derived from the Boltzmann transport equation [65]. In the derivation of these equations



with

$$R_s = \frac{\sqrt{2} \Delta V_{BDAC}(\text{rms})}{B(\text{rms}) \times I(\text{rms})} \quad (5.3)$$

If the contacts are labeled clockwise,  $R_{ABCD}$  represents the voltage developed across contacts A and B when unit current is passed through contacts C and D. The other symbols are defined similarly. In the same way,  $\Delta V_{BDAC}$  represents the voltage measured at the heterodyne frequency across contacts B and D for unit current through contacts A and C under the ac magnetic field  $B(\text{rms})$  (202 gauss for the present system).

Here  $f\left(\frac{R_{ABCD}}{R_{BCDA}}\right)$  is a tabulated factor given by van der Pauw [61] and  $e$  is the electronic charge. By successively removing layers of thickness  $d_j$ , the average carrier concentration and mobility of the layer can be determined by measuring the sheet resistivity  $\rho_{sj}$  and sheet Hall coefficient  $R_{sj}$  before stripping and the same quantities after stripping (i.e.,  $\rho_{sj-1}, R_{sj-1}$ ). The average mobility in the layer is given by

$$\mu_j = \frac{R_{sj}/\rho_{sj}^2 - R_{sj-1}/\rho_{sj-1}^2}{1/\rho_{sj} - 1/\rho_{sj-1}} \quad (5.4)$$

and the average carrier concentration is given by [27]

$$n_j = \frac{1/\rho_{sj} - 1/\rho_{sj-1}}{ed_j\mu_j} \quad (5.5)$$

The derivation of these equations based on an equivalent circuit model is presented in the Appendix; however, these can also be derived from the Boltzmann transport equation [65]. In the derivation of these equations

it is assumed that the conductivity mobility and the Hall mobility are equal. The two mobilities are equal in the case of impurity banding [66], which takes place in silicon for donor concentrations of  $3 \times 10^{18} \text{ cm}^{-3}$  [67]. Thus, for concentrations greater than  $3 \times 10^{18} \text{ cm}^{-3}$ , the carrier concentrations will be correct to within the experimental limitations of the technique.

Following the measurement of surface sheet resistivity and sheet Hall coefficient, the successive layer removal is accomplished by chemical etching. Before the etch is begun, Apiezon W (black wax) dots of approximately 0.5 mm are melted onto the sample surface outside the corners of the contact pads. These dots serve to protect the original surface and allow for a direct depth calibration through the use of a surface profilometer.

Controlled etching is performed by immersing the sample in a beaker partly filled with the etch solution for a fixed period of time. The mounted sample is held with Teflon-coated tweezers and the solution is manually stirred at approximately 120 rpm during the etching process. Following the etching, the sample is immediately placed in water and then dried with compressed dry nitrogen. The sheet resistivity and Hall measurements are taken, and the entire process is repeated successively until the implanted layer is removed.

The standard silicon planar etch [68] is 300 ml nitric acid, 100 ml acetic acid, 4 ml hydrofluoric acid; however, its etch rate was determined experimentally to be approximately 5  $\mu\text{m}/\text{minute}$ . Since the concentration of hydrofluoric acid controls the etch rate [69], a more dilute etch was constructed by mixing 10.4 ml of a mixture consisting of 100 ml acetic acid and 4 ml of hydrofluoric acid with 90 ml of acetic acid and 300 ml of nitric

acid. The more dilute etch was used during this study. The etch rate varied from one mixture to another from a minimum of  $230 \text{ \AA/minute}$  to a maximum of  $580 \text{ \AA/minute}$ , but was fairly consistent within a given batch. The variation in etch rate from one solution to the other indicates the difficulty in controlling such small concentrations of hydrofluoric acid in the solutions. It is also possible that other factors, such as extent of crystalline damage and the position of the Fermi level in the sample, may also have had an effect on the etch rate.

The concentration dependence of the etch was determined by etching through a sample with a nearly gaussian impurity distribution, measured by the differential Hall effect method. This sample was etched past the peak of the impurity distribution until the impurity concentration ( $6.3 \times 10^{19} \text{ cm}^{-3}$ ) was 7.5% of the peak concentration. The dots were then removed, other dots formed in different areas of the sample, and an equal number of steps removed. The step heights were then measured with a Sloan Dektak. The etch rate through the region with the maximum impurity concentration was  $300 \pm 30 \text{ \AA/minute}$ , while the etch rate for the lower concentration region was  $290 \pm 29 \text{ \AA/minute}$ . Measurements on similar samples using a different batch of etch mixture yielded  $332 \pm 30 \text{ \AA/minute}$  for the peak of the distribution and  $325 \pm 30 \text{ \AA/minute}$  for the tail region of the distribution. For all the samples examined the change in etch rate with concentration was less than the uncertainty in the etch rate. The samples which were steam oxidized following implantation showed the greatest variations. For such samples, the etch rate was typically  $380 \pm 40 \text{ \AA/minute}$  for the peak of the distribution and  $320 \pm 30 \text{ \AA/minute}$  for the tail regions of the distribution. In all cases, the thickness of the layer

removed was calculated from the measured etch rate for that number of steps and not from an etch rate averaged over the total profile.

## 5.2. Sheet Measurements

The formation of emitters for silicon bipolar transistors is one of the major applications of arsenic implantation in silicon. Since the emitter sheet resistivity plays an important part in the determination of transistor gain [70], measurement of the sheet resistivity of arsenic implanted layers has immediate technical importance. In addition, these measurements, when combined with measurements of sheet Hall coefficient, yield a direct estimate of the activation of the implanted ions for the bare surface implants. Difficulties are encountered, however, in estimating the activation of the through-oxide implants since not all of the total dose reaches the silicon substrate. For those cases, one must compare the integrated electrically active concentration to the integrated total impurity concentration to obtain a true value for activation. In this study, all values quoted represent an average of measurements from at least four identical samples.

Sheet resistivity measurements have recently been performed through-oxide implanted samples [71], but these were only for 1000°C anneals. No mention was made of electrical activation and no measurements of carrier or mobility profiles were attempted. The values obtained in this study for the sheet resistivities and sheet Hall coefficients of the bare surface and through-oxide implants following 600°C annealing are summarized in Table IV. From these results it can be seen that the  $1 \times 10^{15} \text{ cm}^{-2}$  implants attain almost identical sheet resistivities following 600°C annealing. It can also be seen that the  $1 \times 10^{15} \text{ cm}^{-2}$  bare surface implant

TABLE IV

Average sheet resistivities and average sheet carrier concentrations for  $\text{As}^+$  implanted  $\langle 100 \rangle$  p-type silicon substrates following  $600^\circ\text{C}$  30 minute annealing.

| <u>Sample Type</u> | <u>As Implant</u>                          | <u>Surface condition before Implantation</u> | <u>Average Sheet Resistivity</u> | <u>Average Sheet Carrier Concentration</u> |
|--------------------|--|--|----------------------------------|--|
| 1                  | $5 \times 10^{15} \text{ cm}^{-2}$ 150 keV | $150 \text{ \AA SiO}_2$                      | $65 \text{ } \Omega/\square$     | $2.1 \times 10^{15} \text{ cm}^{-2}$       |
| 5                  | $5 \times 10^{15} \text{ cm}^{-2}$ 150 keV | Bare   | $56 \text{ } \Omega/\square$     | $1.9 \times 10^{15} \text{ cm}^{-2}$       |
| 13                 | $1 \times 10^{15} \text{ cm}^{-2}$ 200 keV | $840 \text{ \AA SiO}_2$                      | $98 \text{ } \Omega/\square$     | $8.2 \times 10^{14} \text{ cm}^{-2}$       |
| 14                 | $1 \times 10^{15} \text{ cm}^{-2}$ 200 keV | Bare   | $96 \text{ } \Omega/\square$     | $9.9 \times 10^{14} \text{ cm}^{-2}$       |

has reached nearly complete electrical activity following the 600°C annealing, consistent with the work of Crowder [72], who sees complete electrical activity for peak impurity concentrations less than  $2 \times 10^{20} \text{ cm}^{-3}$ . For the samples implanted to  $5 \times 10^{15} \text{ cm}^{-2}$ , the sheet resistivities and sheet carrier concentrations agree to within 10% for the bare surface and through oxide implanted samples. The higher dose bare surface implant shows approximately 40% activation of the implanted ions, which is reasonable in view of its peak impurity concentration of  $7 \times 10^{20} \text{ cm}^{-3}$  [59]. The  $5 \times 10^{15} \text{ cm}^{-2}$  through-oxide implant shows an activation similar to that of the corresponding bare surface implant.

Since the  $1 \times 10^{15} \text{ cm}^{-2}$  implants showed practically complete electrical activity, they were not subjected to further anneals. Samples subjected to higher fluence implants were examined after 30 minute anneals of 700°C, 800°C, 900°C or 1000°C, and the results are summarized in Fig. 5.4. Again, it can be seen that both the sheet resistivities and the sheet carrier concentrations are nearly identical for each annealing temperature to 1000°C. The scatter in the through oxide implanted samples compared to the bare surface implants is probably due to variations in the oxide thickness, affecting both the projected range and peak concentration of the arsenic ions. These results are surprising in view of the vast crystallographic damage seen by transmission electron microscopy [4,7] and by He ion backscattering [5] for through oxide implanted samples annealed at 1000°C. When the  $5 \times 10^{15} \text{ cm}^{-2}$  implanted samples are annealed for 5 minutes in dry nitrogen, followed by  $\text{SiO}_2$  thermal growth which incorporates the entire implanted layer, sheet resistivities and carrier concentrations were nearly identical for the bare surface and through oxide implants (Table V). This



Figure 5.4. Variation in sheet carrier concentrations (top graph) and sheet resistivities (bottom) with annealing temperature for  $5 \times 10^{15} \text{ cm}^{-2}$  150 keV As implants into bare surfaces (squares) and through approximately 150 Å  $\text{SiO}_2$  (circles).

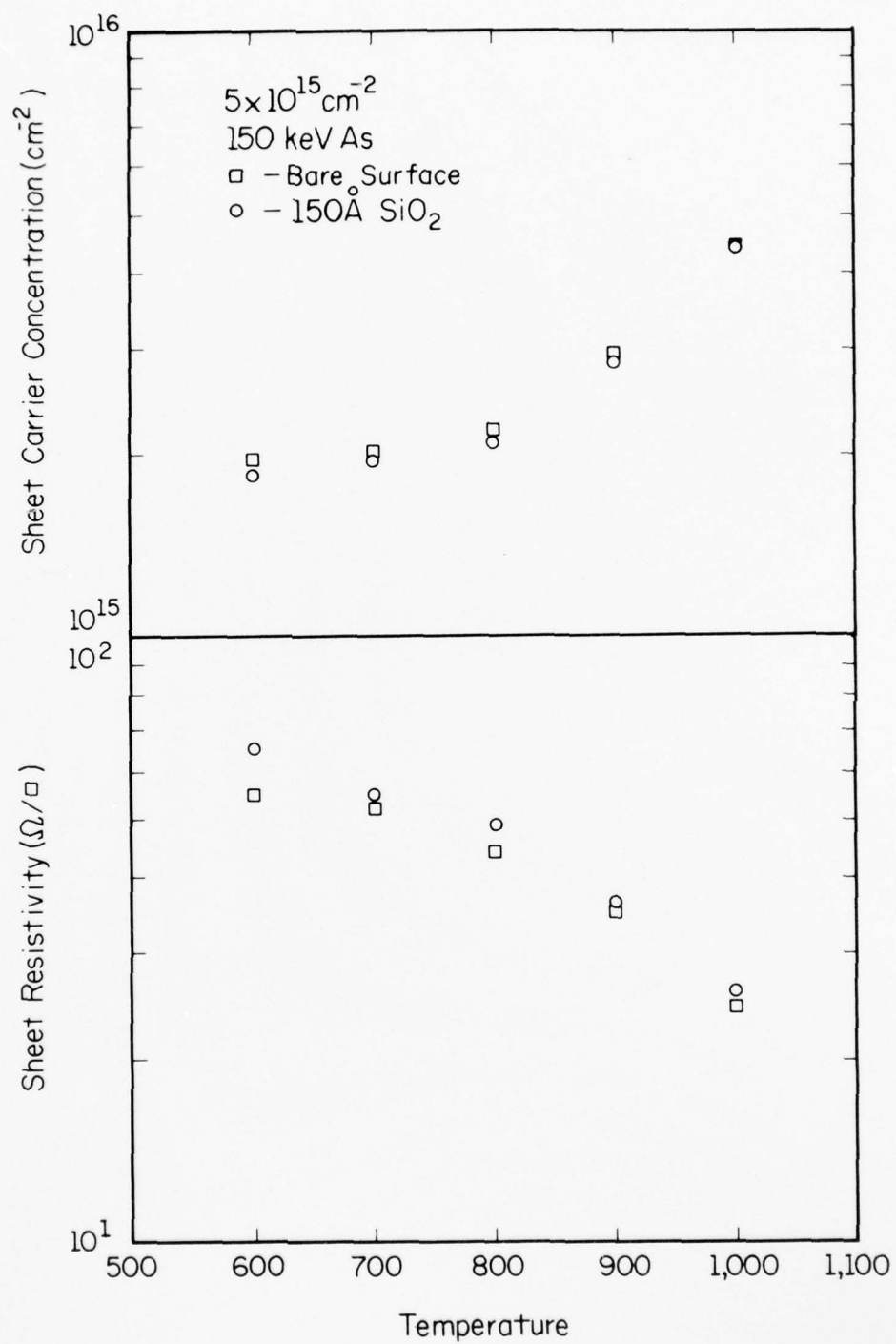


TABLE V

Average sheet resistivities and average sheet carrier concentrations for  $5 \times 10^{15} \text{ cm}^{-2}$  150 keV  $\text{As}^+$ -implanted  $\langle 100 \rangle$  p-type silicon substrates following redistribution by thermal oxidation. Oxide thickness was determined by ellipsometry.

| Sample Type | Surface before Implantation          | Oxidation Temperature | Final $\text{SiO}_2$ Thickness | Sheet Resistivity             | Carrier Concentration                |
|-------------|--------------------------------------|-----------------------|--------------------------------|-------------------------------|--------------------------------------|
| 2           | $\sim 150 \text{ \AA} \text{ SiO}_2$ | $900^\circ\text{C}$   | $3272 \text{ \AA}$             | $126 \text{ } \Omega/\square$ | $7.3 \times 10^{14} \text{ cm}^{-3}$ |
| 3           | $\sim 150 \text{ \AA} \text{ SiO}_2$ | $1100^\circ\text{C}$  | $4432 \text{ \AA}$             | $20 \text{ } \Omega/\square$  | $4.7 \times 10^{15} \text{ cm}^{-3}$ |
| 4           | Bare                                 | $900^\circ\text{C}$   | $3338 \text{ \AA}$             | $128 \text{ } \Omega/\square$ | $7.1 \times 10^{14} \text{ cm}^{-3}$ |
| 6           | Bare                                 | $1100^\circ\text{C}$  | $4382 \text{ \AA}$             | $20 \text{ } \Omega/\square$  | $4.6 \times 10^{15} \text{ cm}^{-3}$ |

AD-A040 683

ILLINOIS UNIV AT URBANA-CHAMPAIGN COORDINATED SCIENCE LAB F/G 20/12  
PROPERTIES OF SILICON IMPLANTED WITH ARSENIC THROUGH SILICON DI--ETC(U)  
JAN 77 D R MYERS  
R-756

DAAB07-72-C-0259

NL

UNCLASSIFIED

2 OF 2  
AD  
A040683



END

DATE  
FILMED  
7-77

also is surprising, in view of the fact that the 2 to 1 increase in volume in the surface silicon layer due to thermal oxidation is known to propagate surface defects further into the silicon substrate [73].

Finally, an attempt was made to determine an activation energy for the annealing of sheet resistivity and sheet carrier concentration of the  $5 \times 10^{15} \text{ cm}^{-2}$  implants. Isothermal anneals were performed at  $600^{\circ}\text{C}$  for 30 minutes, 60 minutes, and 150 minutes, but no change in sheet carrier concentration nor sheet resistivity could be observed among the various anneals, within experimental uncertainty. Apparently, annealing operative at  $600^{\circ}\text{C}$  occurs rapidly ( $< 30 \text{ min}$ ).

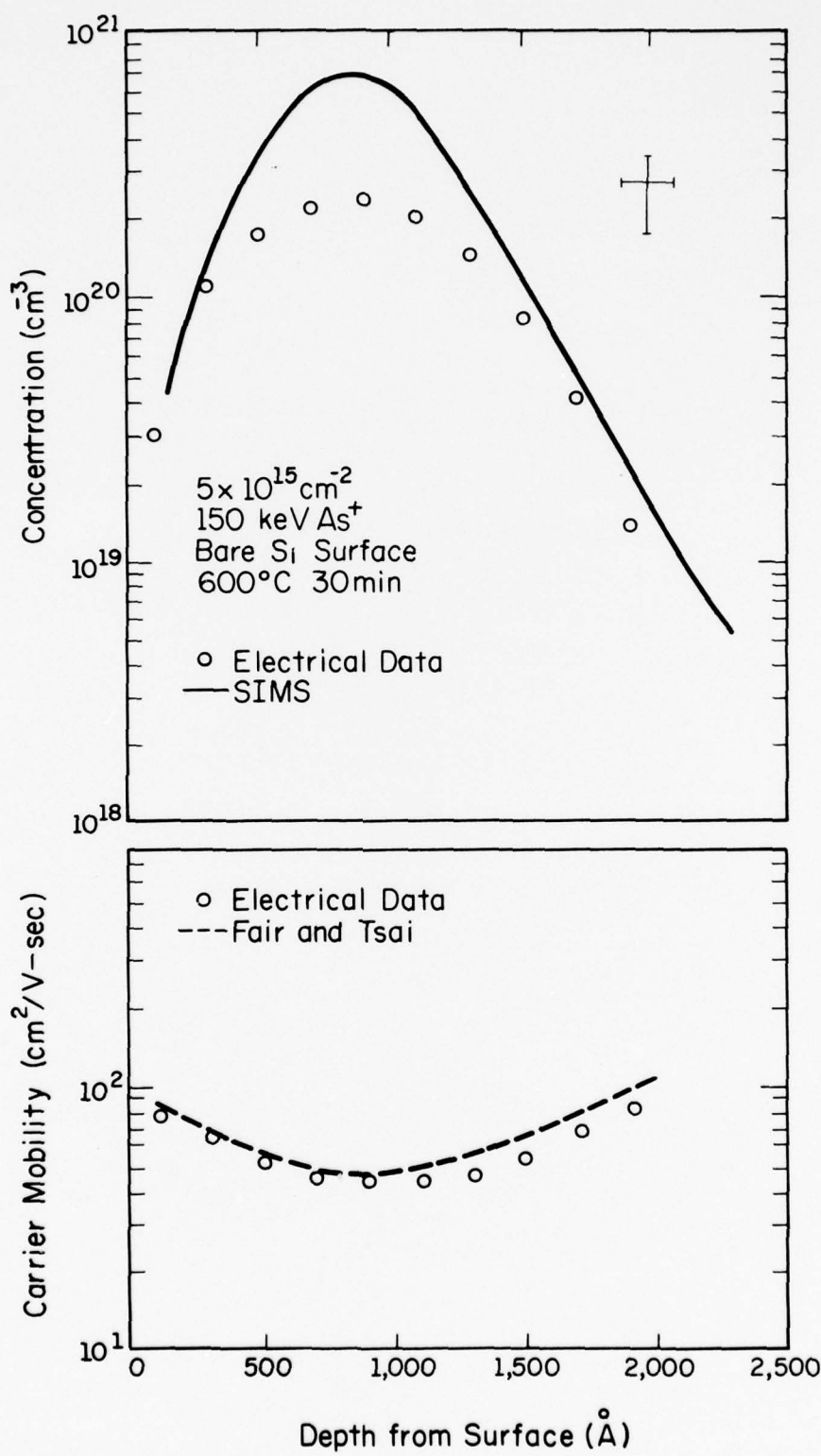
### 5.3. Carrier Concentration and Mobility Profiles

The only way to obtain a true estimate of the impurity activation and carrier transport properties of the through-oxide implanted samples is by combining differential Hall effect measurements with a technique that measures the total impurity distribution, such as SIMS. These measurements are performed on the through-oxide implanted samples and also on the equivalent bare surface implanted wafers. This comparison provides a direct measurement of the effects of the damage produced by recoil implanted oxygen on the transport properties of through-oxide implanted layers. Although the interpretation of the results obtained is complicated by the fact that the grown oxides were of nonuniform thickness, we shall see that the depth profiles verify the trends seen from the sheet resistivity measurements and provide a partial explanation of these trends.

In Fig. 5.5 we present the carrier concentration and mobility profiles for the  $5 \times 10^{15} \text{ cm}^{-2}$  150 keV As implant. Comparing the electrical profile with the total impurity profile indicates a concentration-dependent activation after  $600^\circ\text{C}$  annealing consistent with the measurements of Crowder [72]. Integrating the carrier concentration over the depth distribution yields a result in excellent agreement with the sheet carrier concentration reported in Table IV. In the plot of the mobility as a function of depth, the experimentally-obtained mobilities are compared to mobility values expected for the experimentally-determined carrier concentrations. The expected values of mobility for the given carrier concentrations are obtained from an eleven-term polynomial fit to the empirical resistivity-carrier concentration relationship for arsenic-doped silicon determined by Fair and Tsai [59].



Figure 5.5. Carrier concentration and mobility profiles for 600°C 30 minute anneal of  $5 \times 10^{15} \text{ cm}^{-2}$  150 keV  $\text{As}^+$  implants into bare Si surface. Top: comparison of electrically active arsenic concentration obtained by differential Hall effect measurements (circles) with total arsenic concentration obtained by SIMS (solid line). Bottom: comparison of mobility values obtained by differential Hall effect measurements with values expected from polynomial fit of Fair and Tsai [59] to empirical carrier concentration-mobility relationship for As-doped Si.



It is seen that the experimentally observed mobilities agree well with the expected values. Annealing the  $5 \times 10^{15} \text{ cm}^{-2}$  150 keV As implant to  $1000^{\circ}\text{C}$  (Fig. 5.6) produces excellent electrical activation, in good agreement with the other studies of implanted arsenic [59], and the experimentally-determined mobilities exhibit excellent agreement with the expected mobilities. Integrating the electrically active profile yields results in excellent agreement with the sheet carrier concentration values. Throughout this study, the integrated carrier concentrations never differed from the measured sheet carrier concentrations by more than 10%, and thus the agreement will no longer be noted in the descriptions of the remaining profiles.

In Figs. 5.7 and 5.8, we examine the corresponding samples implanted through thin oxides. Since the oxide thickness for the implanted layer was found to be nonuniform, difficulties are encountered in correlating the depth scales between the electrically-active profile and the SIMS profile.

Throughout this study, effort was made to take samples for elemental profiling and samples used for electrical measurements from adjacent areas on the implanted wafer. Despite these efforts, examination of Fig. 5.7 indicates that the oxide thickness for the area of the wafer used for SIMS profiling was slightly thicker than the oxide thickness for the area of the wafer used for electrical profiling. Thus the depth distributions peak at different values from the silicon-silicon dioxide interface. Nevertheless, we observe that electrical activation similar to the bare surface implant is attained, and that surprisingly, the mobilities obtained for the through-oxide implants agree well with the expected values for arsenic-doped silicon. Annealing the through oxide implanted sample to  $1000^{\circ}\text{C}$  - where the residual

Figure 5.6. Carrier concentration and mobility profiles for 1000°C 30 minute anneal of  $5 \times 10^{15} \text{ cm}^{-2}$  150 keV  $\text{As}^+$  implants into bare Si surface. Top: comparison of electrically active arsenic concentration obtained by differential Hall effect measurements (circles) with total arsenic concentration obtained by SIMS (solid line). Bottom: comparison of mobility values obtained by differential Hall effect measurements with values expected from polynomial fit of Fair and Tsai [59] to empirical carrier concentration-mobility relationship for As-doped Si.

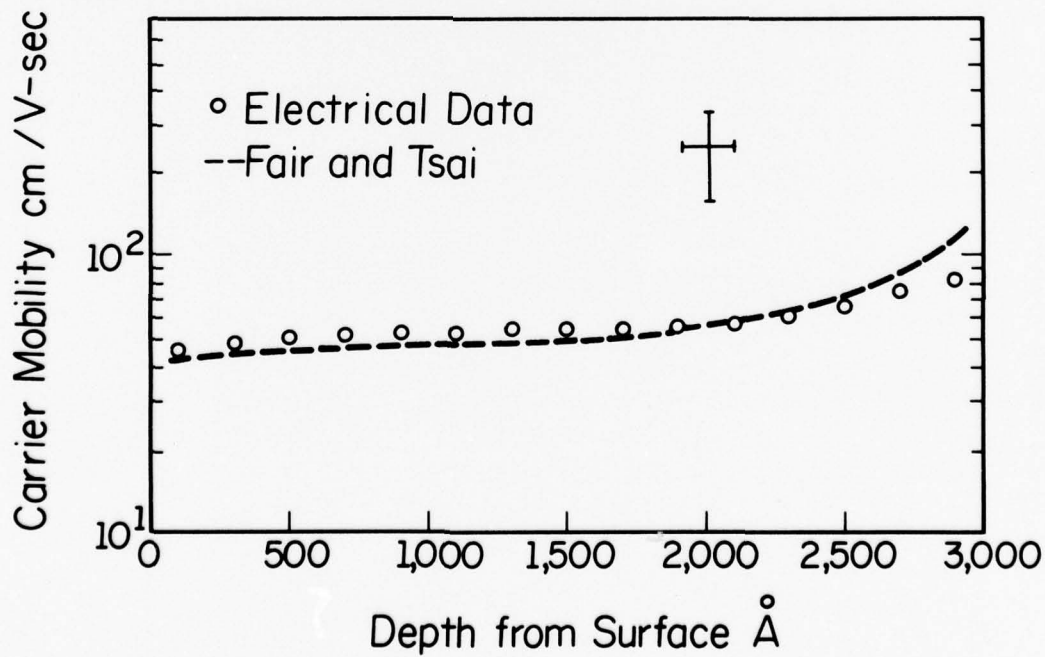
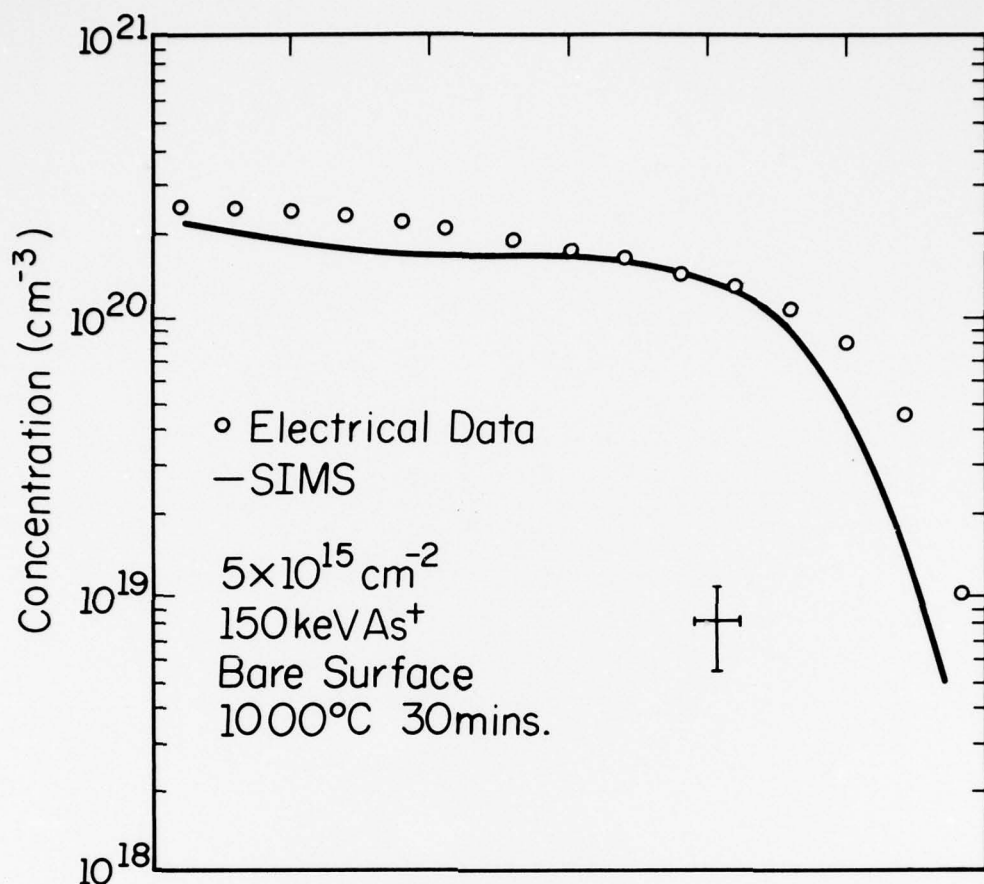




Figure 5.7. Carrier concentration and mobility profiles for 600°C 30 minute anneal of  $5 \times 10^{15} \text{ cm}^{-2}$  150 keV  $\text{As}^+$  implants through approximately 150 Å  $\text{SiO}_2$ . Top: comparison of electrically active arsenic concentration obtained by differential Hall effect measurements (circles) with total arsenic concentration obtained by SIMS (solid line). Bottom: comparison of mobility values obtained by differential Hall effect measurements with values expected from polynomial fit of Fair and Tsai [59] to empirical carrier concentration-mobility relationship for As-doped Si.



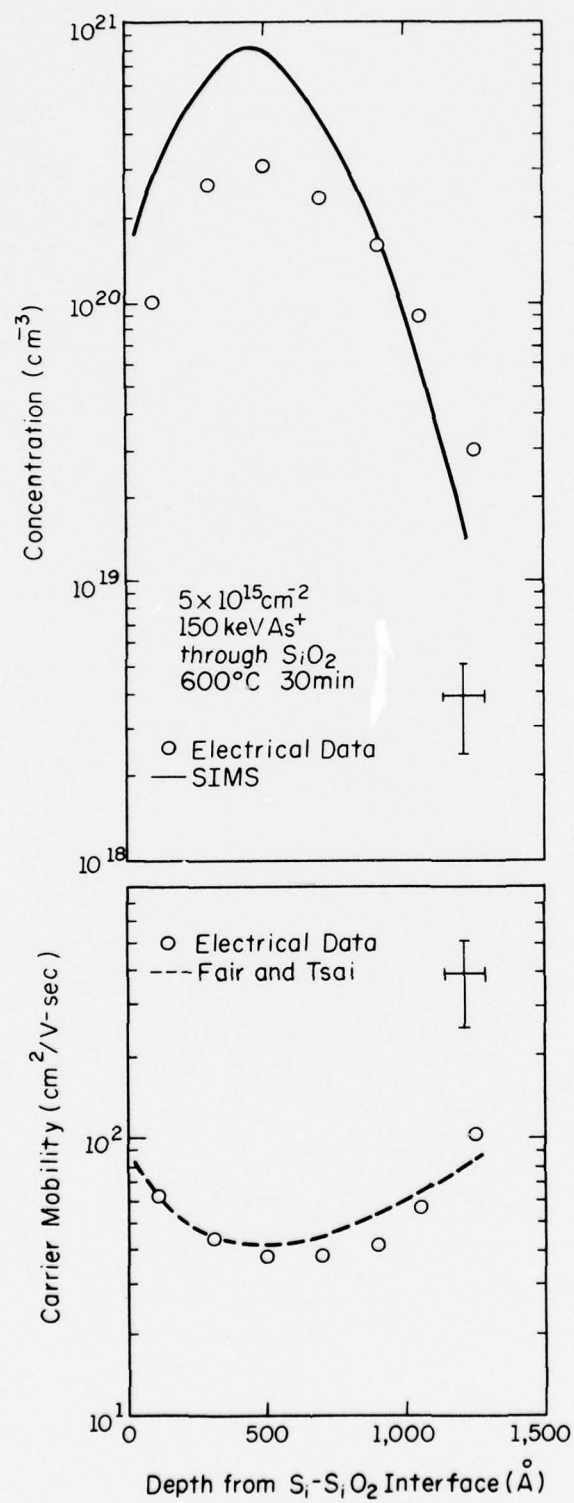
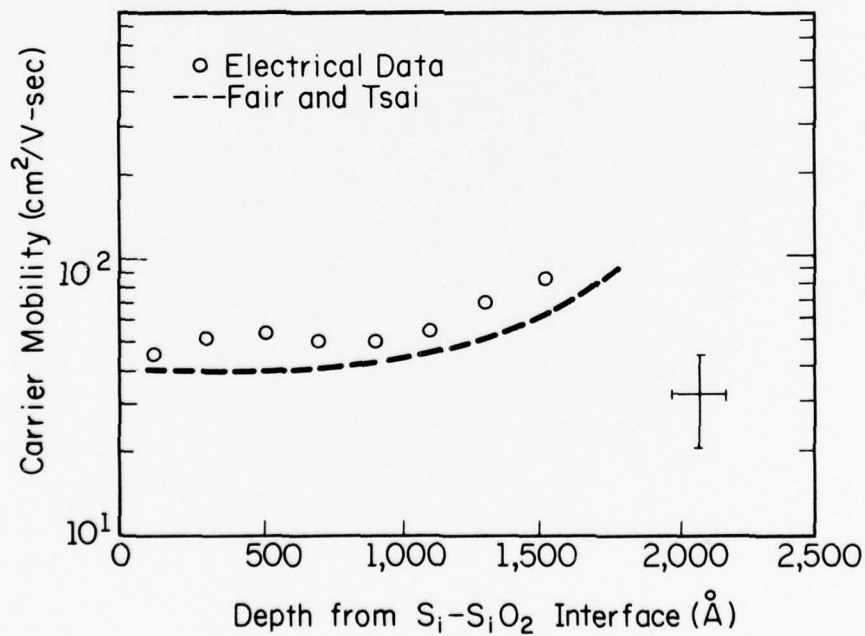
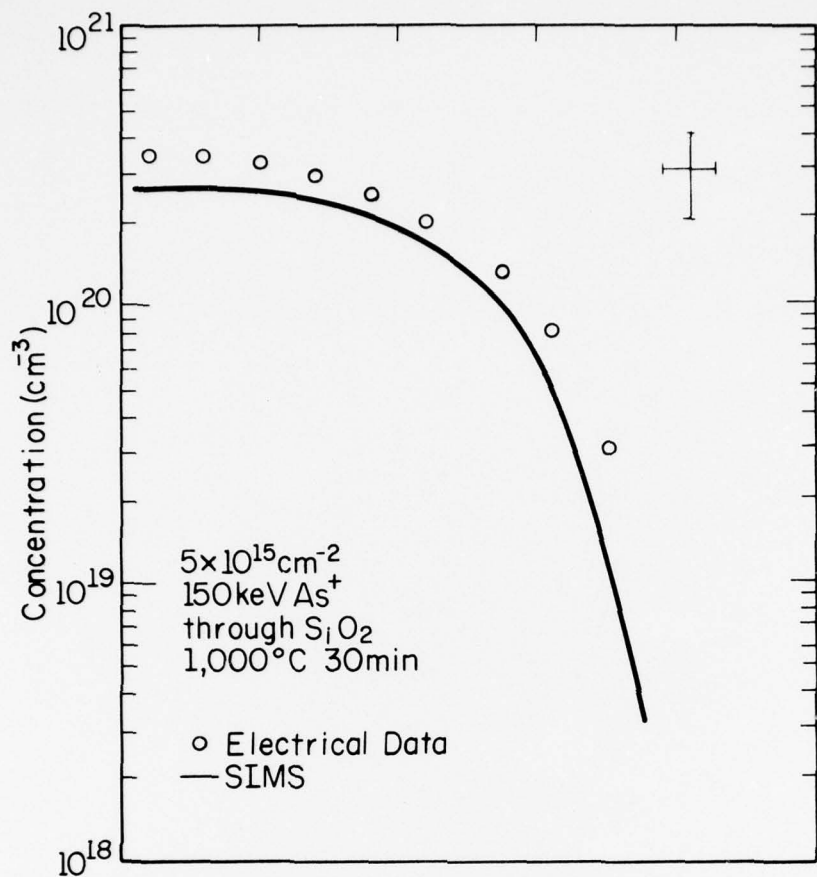


Figure 5.8. Carrier concentration and mobility profiles for 1000°C 30 minute anneal of  $5 \times 10^{15} \text{ cm}^{-2}$  150 keV  $\text{As}^+$  implants through approximately 150 Å  $\text{SiO}_2$ . Top: comparison of electrically active arsenic concentration obtained by differential Hall effect measurements (circles) with total arsenic concentration obtained by SIMS (solid line). Bottom: comparison of mobility values obtained by differential Hall effect measurements with values expected from polynomial fit of Fair and Tsai [59] to empirical carrier concentration-mobility relationship for As-doped Si.



damage was originally observed [4] - again shows electrical activation identical to the bare surface implant and surprisingly good mobility values. Even more surprisingly, when silicon dioxide layers are thermally grown to incorporate the entire implanted layer, the carrier and mobility profiles for the bare surface and through oxide implants are identical, to within experimental uncertainties. Thus in Figs. 5.9 and 5.10, only one set of points is shown to indicate the profiles obtained from both implant conditions. In Fig. 5.9, we again see that for the  $1100^{\circ}\text{C}$  redistribution nearly complete electrical activation is obtained, and that experimental mobilities agree well with the expected values. Apparently the diffusion coefficient of arsenic in silicon at  $1100^{\circ}\text{C}$  is large enough that the arsenic displaced by the moving silicon-silicon dioxide boundary diffuses away from the interface fast enough to prevent an appreciable impurity pile-up. Such is not the case, however, for the  $900^{\circ}\text{C}$  oxidation. Here the arsenic has accumulated within a few hundred angstroms of the silicon-silicon dioxide interface. Such shallow profiles are extremely difficult to measure accurately. The chemical etch rate was appreciably faster for the peak of this distribution than for the tail region (section 5.1) while the SIMS data overestimates the depth of the distribution due to matrix effects and differential sputtering. These problems make it difficult to correlate the electrically-active concentration profile with the elemental profile, although both methods gave consistent readings within themselves. Good mobility and activation are also obtained for annealing of samples implanted through thicker oxides (Fig. 5.11 + 5.12).

The work reported in this chapter represents the first complete set of electrical measurements of the transport properties of through-oxide

Figure 5. 9. Carrier concentration and mobility profiles following redistribution by wet oxidation for 60 minutes at  $1100^{\circ}\text{C}$  of  $5 \times 10^{15} \text{ cm}^{-2}$  150 keV  $\text{As}^{+}$  implants. Results for bare surface and through oxide implants identical. Top: comparison of electrically active arsenic concentration obtained by differential Hall effect measurements (circles) with total arsenic concentration obtained by SIMS (solid line). Bottom: comparison of mobility values obtained by differential Hall effect measurements with values expected from polynomial fit of Fair and Tsai [59] to empirical carrier concentration-mobility relationship for As-doped Si.

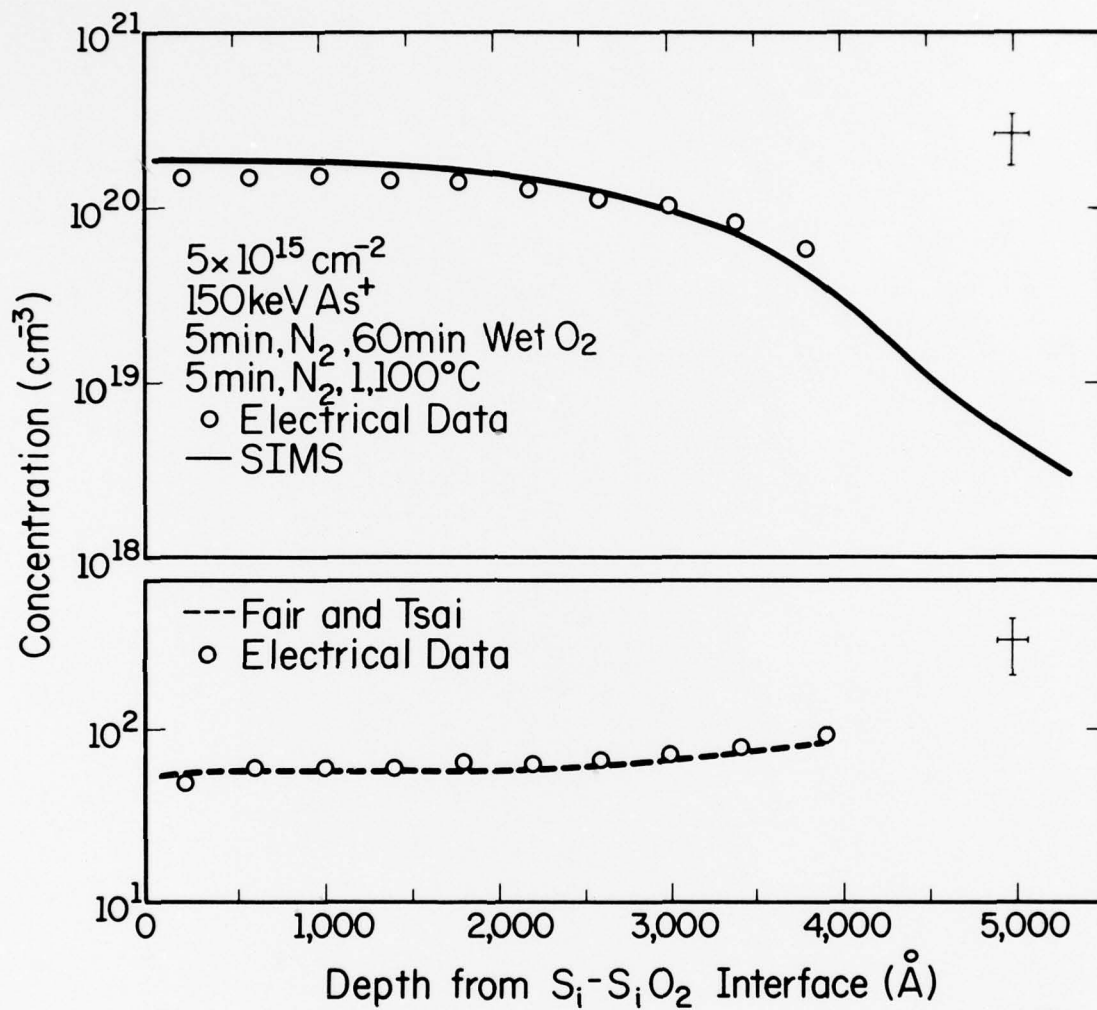
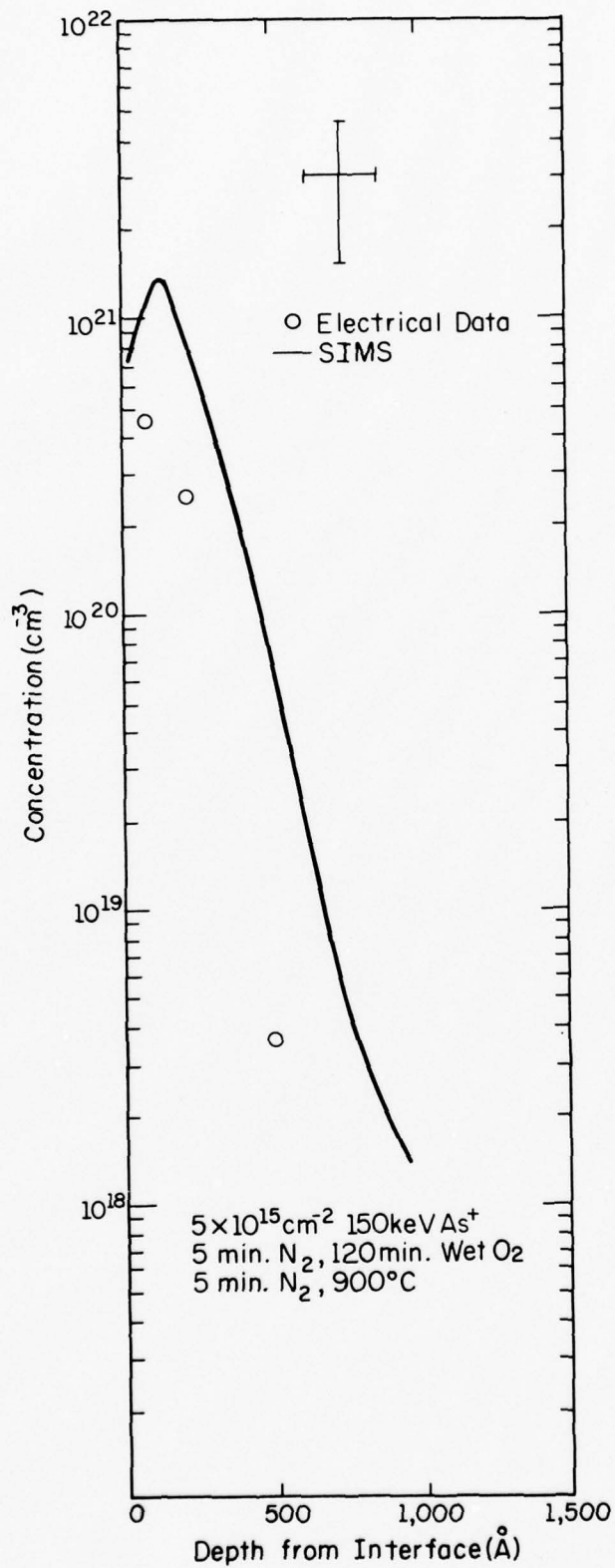


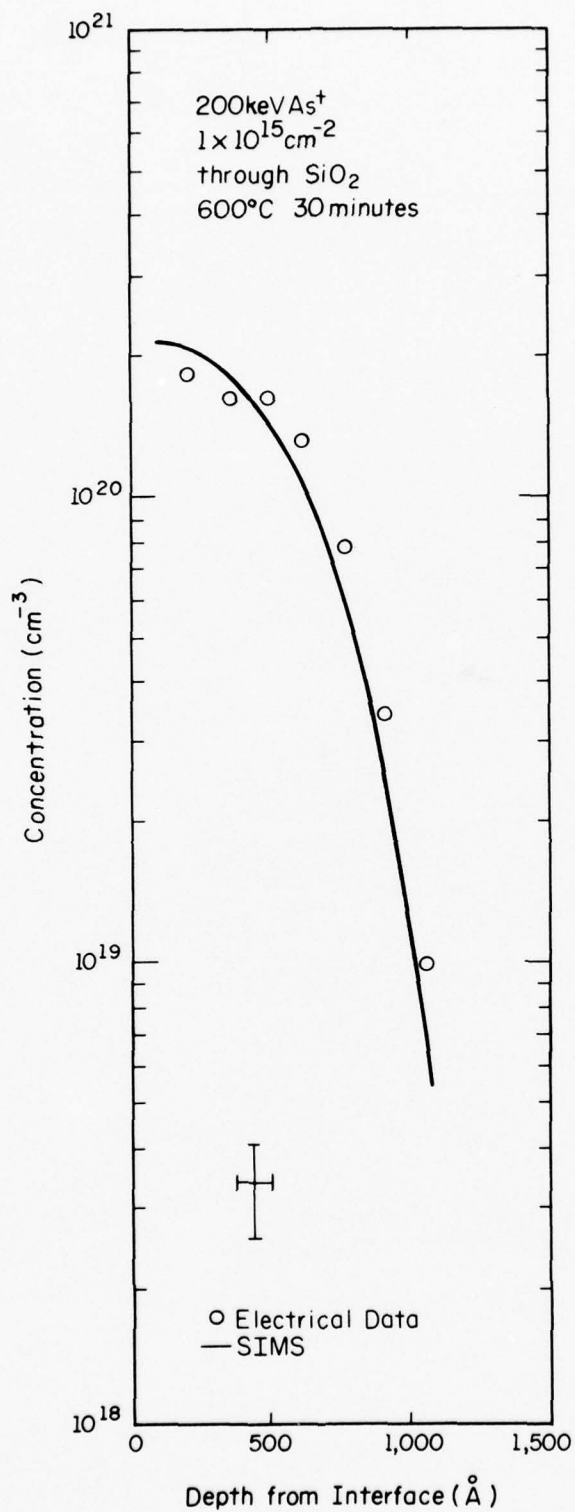


Figure 5.10. Carrier concentration and mobility profiles following redistribution by wet oxidation for 120 minutes at 900°C of  $5 \times 10^{15} \text{ cm}^{-2}$  150 keV  $\text{As}^+$  implants. Results for bare surface and through oxide implants identical. Top: comparison of electrically active arsenic concentration obtained by differential Hall effect measurements (circles) with total arsenic concentration obtained by SIMS (solid line).



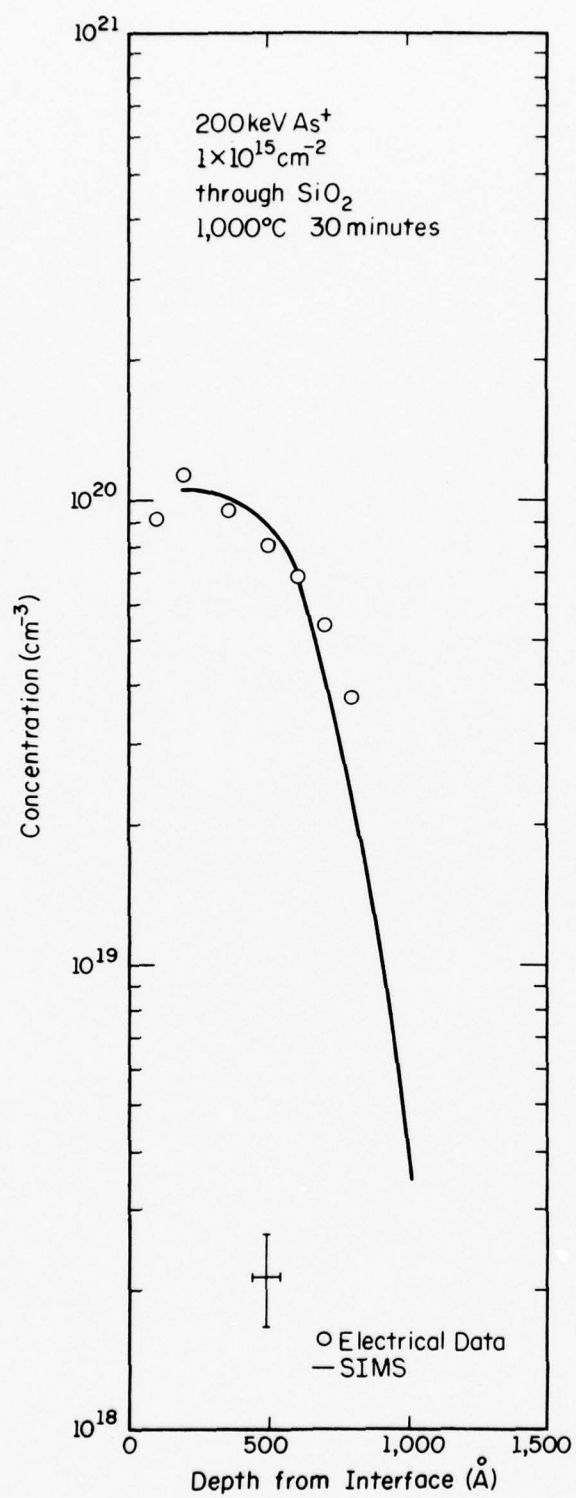
LP-1278

Figure 5.11. Carrier concentration and mobility profiles for 600°C 30 minute anneal of  $1 \times 10^{15} \text{ cm}^{-2}$  200 keV  $\text{As}^+$  implants through approximately 840 Å  $\text{SiO}_2$ . Top: comparison of electrically active arsenic concentration obtained by differential Hall effect measurements (circles) with total arsenic concentration obtained by SIMS (solid line).



LP-1275

Figure 5.12. Carrier concentration and mobility profiles for 1000°C 30 minute anneal of  $1 \times 10^{15} \text{ cm}^{-2}$  200 keV  $\text{As}^+$  implants through approximately 840 Å  $\text{SiO}_2$ . Top: comparison of electrically active arsenic concentration obtained by differential Hall effect measurements (circles) with total arsenic concentration obtained by SIMS (solid line).



LP-1274



implanted silicon. It is seen that good electrical properties of the through-oxide implanted samples suggested by the sheet resistivity measurements are due to two factors: activation for the through-oxide implant identical to bare surface implanted silicon and the attainment of carrier mobilities in the through oxide implanted layers identical to mobilities obtained for bulk silicon. These results could hardly have been suspected prior to this investigation, due to the known complexing of arsenic and oxygen in radiation-damaged silicon [8] and the extensive damage seen for through-oxide implanted samples [4,5,7]. These results do, however, provide for a possible interpretation, which we shall develop in the next chapter.

#### 5.4. Discussion of Uncertainties

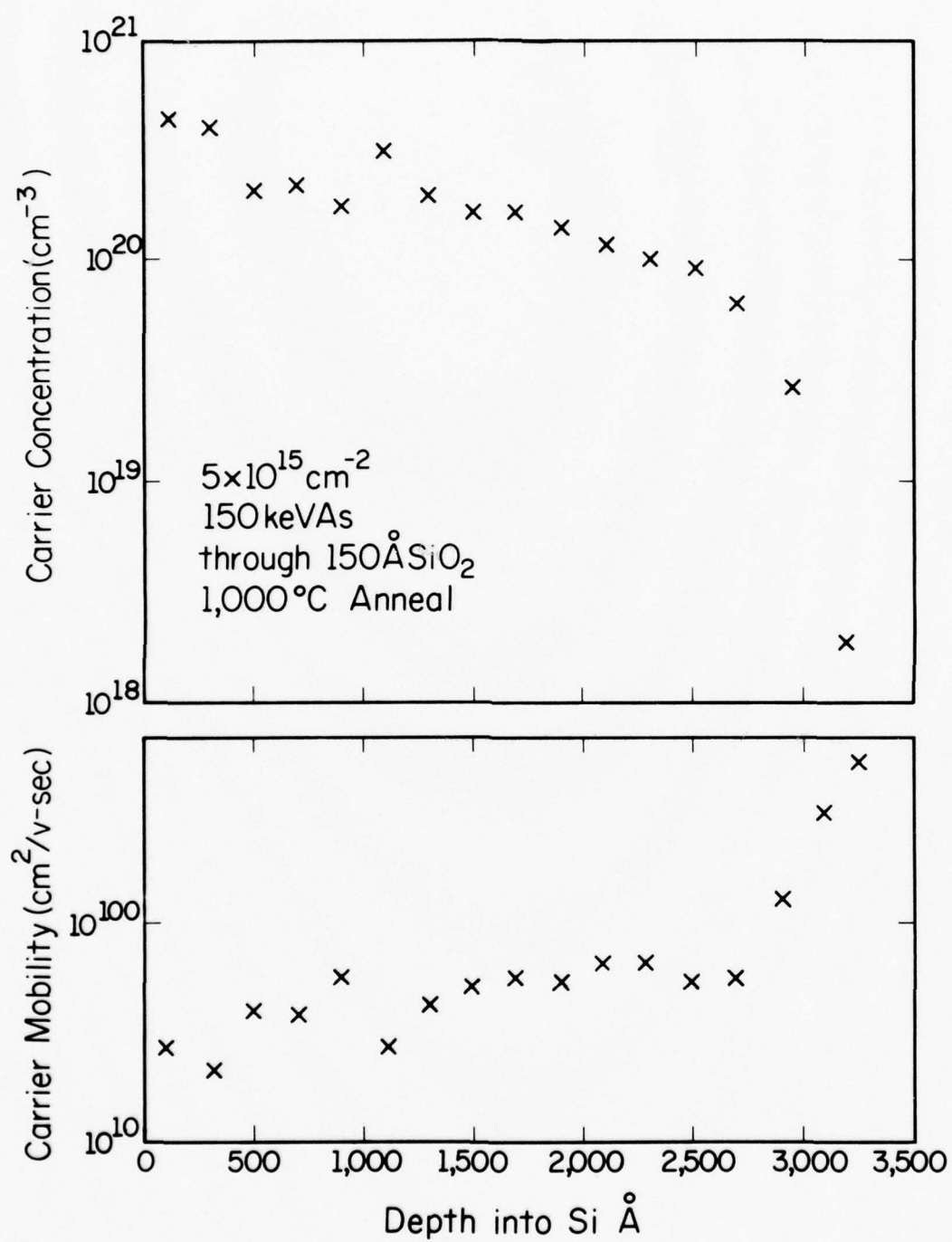
The major sources of uncertainty in determining the electrically active impurity profile and the mobility profile for the implanted layer are nonuniformity of layer thickness, uncertainty in measurement of sample currents and voltages, uncertainty in magnetic field strength, and junction leakage from the implanted layer. From Eq. (5.1), it is seen that the uncertainties in sheet Hall coefficient and sheet resistivity are directly proportional to the uncertainty in the measurement of sample voltages, while the uncertainty in the sheet Hall coefficient is inversely proportional to both the magnetic field strength and the sample current. For the present system, the magnetic field is  $202 \pm 2$  gauss, which would create a 1% uncertainty in the sheet Hall coefficient. The sample current is determined by measuring the voltage developed across a  $100 \Omega$  precision resistor using a PAR HR-8 lock-in amplifier, which is read out on a Keithley 160 digital multimeter. Sample voltages are

measured directly using a PAR 186A lock-in amplifier and are read out on a Digitec dc digital voltmeter. Drift of the reference frequency for the HR-8, voltage loss in the connecting cables, variations in contact pressure for the Pogo stick contacts, and electrical noise all combine to produce less than a 3% spread in the measured voltages for a given sample.

To understand how the uncertainties in the sheet resistivity and sheet Hall coefficient affect the experimentally determined carrier concentrations and mobilities, one must consider the mathematical form of Eqs. (5.4) and (5.5). This can best be illustrated by first considering the effects of layer removal on a uniformly doped sample, and then extending this analysis to the experimentally encountered profiles.

For a uniformly doped sample, graphs of sheet resistivity and sheet Hall coefficient with depth form hyperbolas, the two quantities being related by a constant. The above can be verified by examination of Eqs. (A.17) and (A.18) of the Appendix for  $n_i$  and  $\mu_i$  constant. If we now consider an actual impurity profile with a slight slope (Fig. 5.13), we see that the sheet resistivity and sheet Hall coefficients are no longer related by a constant, but rather that the sheet Hall coefficient increases more rapidly with depth than the sheet resistivity (Fig. 5.14). This behavior is expected since the sheet Hall coefficient is essentially proportional to  $1/n_{eff}$ , while the sheet resistivity is proportional to  $1/n_{eff}\mu_{eff}$ , where  $n_{eff}$  and  $\mu_{eff}$  are "average" carrier concentrations and mobilities, respectively. Because lower carrier concentrations have higher mobilities, the loss of free carriers in the sheet resistivity is partly offset by their increased mobility, while this effect does not occur for the sheet Hall coefficient. The changes in

Figure 5.13. Measured depth variation of carrier concentration and mobility for nearly uniform profile with slight gradient ( $1000^{\circ}\text{C}$  30 minute anneal of the  $5 \times 10^{15}$  150 keV As implant through approximately  $150 \text{ \AA}$  of  $\text{SiO}_2$ ). Scatter in the first two points is due to the small percentage change in sheet resistivity at the surface and the scatter near  $1000^{\circ}\text{C}$  is due to a bad data point in the sheet measurements at  $1000 \text{ \AA}$ .



LP-1268

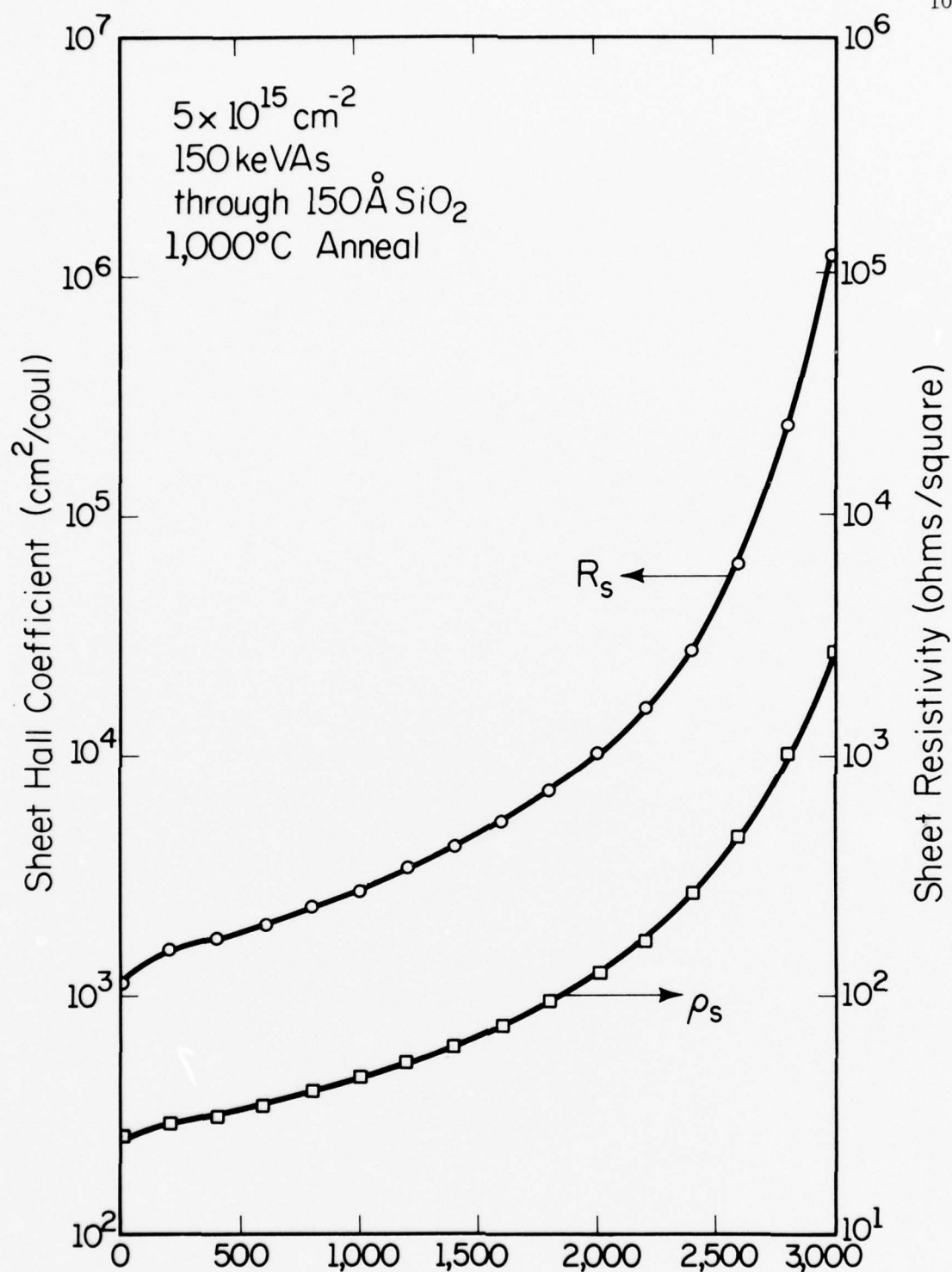


Figure 5.14. Measured variation in sheet resistivity and sheet Hall coefficient with depth for the sample shown in Fig. 5.13 ( $1000^\circ\text{C}$  30 minute anneal of  $5 \times 10^{15} \text{ cm}^{-2}$  150 keV As implant through  $\text{SiO}_2$ ).

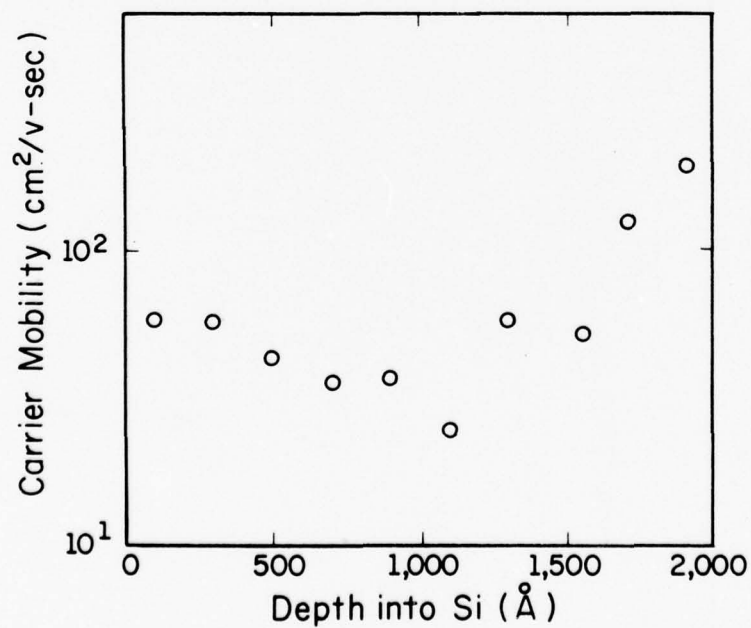
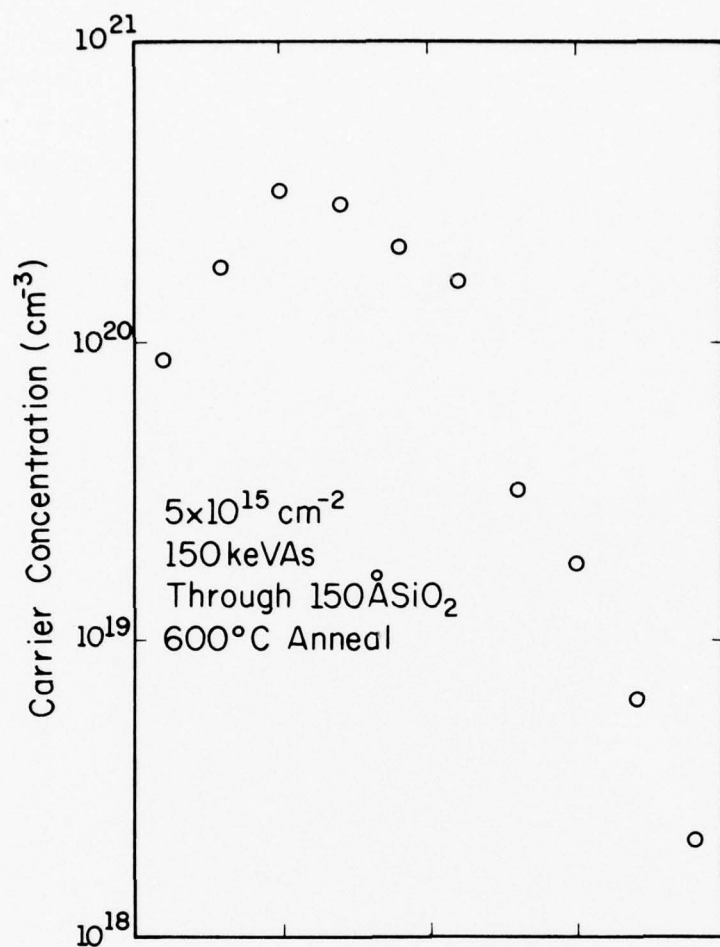


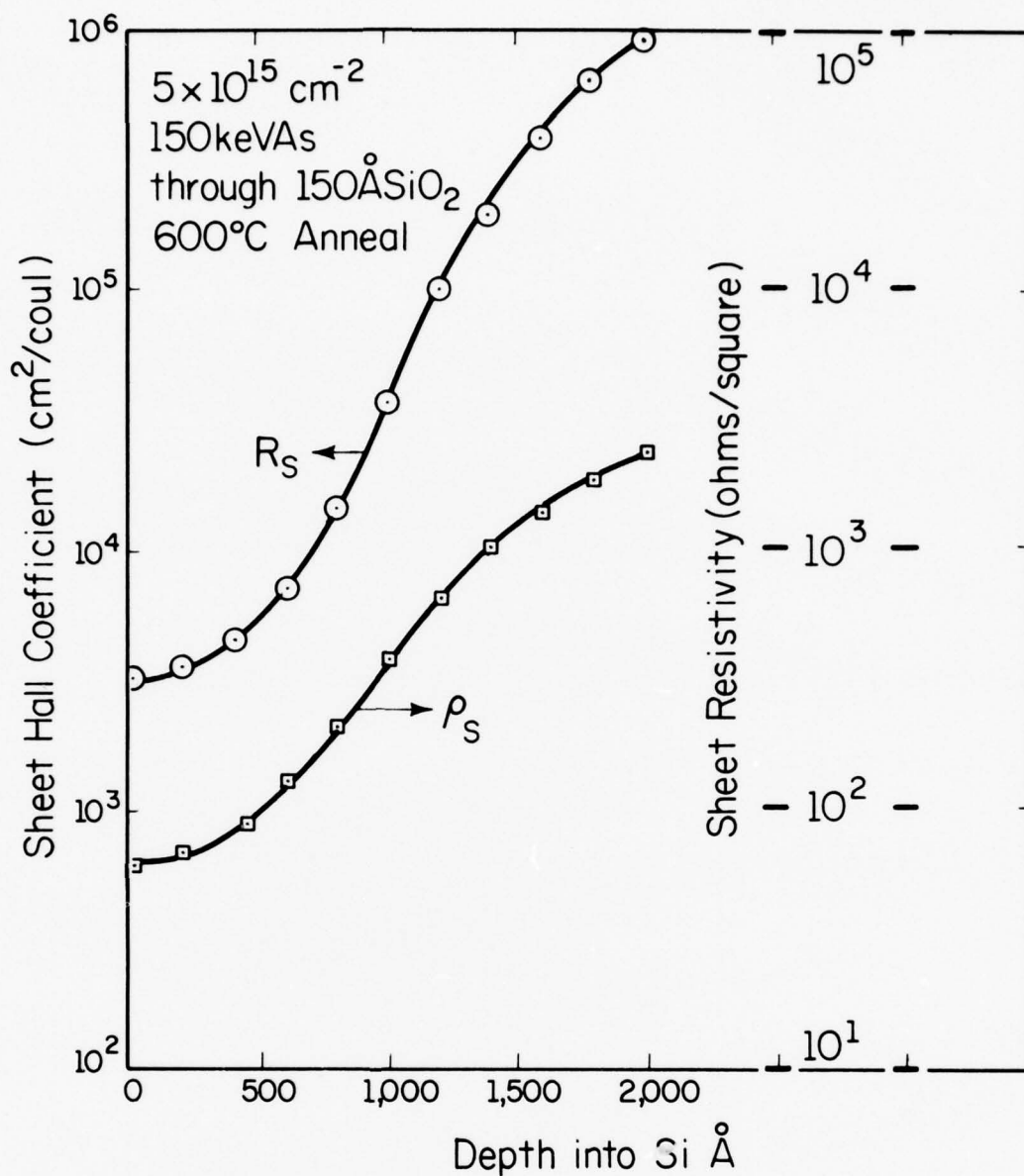
sheet resistivity and sheet Hall coefficients are even more drastic for the case of a gaussian impurity distribution (Figs. 5.15 and 5.16).

The graphs of the raw data presented in Figs. 5.13 and 5.14 help to explain other limitations of the technique. Near the surface, the sheet resistivity suffers only a small percentage change on the removal of the first few layers (Fig. 5.13), and thus uncertainties in the measurement of each sheet resistivity can amount to a significant percentage of the difference between successive sheet resistivities. Because Eq. (5.4) requires the difference between the inverse sheet resistivities and also the difference of their squares, small uncertainties in the measurement of the sheet resistivity (e.g. 3%) can yield large variations (approximately 50%) in sheet mobility and carrier concentration near the surface, as is seen in the profile for the 1000°C anneal (Fig. 5.14). Since Eqs. (5.4) and (5.5) rely on the difference between two sets of data points, one bad measurement affects two sets of data points: the values obtained by comparing the bad data point with the preceding step and the values obtained by comparing the bad data point with the following step. Thus, a bad data point at 1000 Å for the 1000°C annealed sample shown in Fig. 5.13 leads to incorrect values of mobility and carrier concentration at 800 Å and 1200 Å (Fig. 5.14). Even at the peak of the gaussian distribution where the change in both sheet resistivity and sheet Hall coefficient is greatest and thus the percentage uncertainty in the change is the least, values of carrier concentration and mobility are extremely sensitive to variations in sheet resistivity, as can be seen from Table VI. For this reason, the effect of junction leakage on these measurements is of extreme concern. As a rule of thumb, the data is no longer



Figure 5.15. Measured depth variation of carrier concentration and mobility for sample with gaussian-type impurity distribution ( $600^{\circ}\text{C}$  30 minute anneal of  $5 \times 10^{15} \text{ cm}^{-2}$  150 keV  $\text{As}^{+}$  implant through approximately  $150 \text{ \AA}$   $\text{SiO}_2$ ).





LP-1267

Figure 5.16. Measured variation in sheet resistivity and sheet Hall coefficient with depth for sample shown in Fig. 5.15 (600°C 30 minute anneal of  $5 \times 10^{15} \text{ cm}^{-2}$  150 keV As implant through  $\text{SiO}_2$ ).

TABLE VI

Variation in carrier concentration and mobility for a range of values of sheet resistivity. The points taken are near the peak of the impurity distribution for a 600°C anneal of a  $5 \times 10^{15} \text{ cm}^{-2}$  150 keV As implantation through  $\text{SiO}_2$ . The step size used is 200 Å.

| $\rho_s$<br>( $\Omega/\square$ ) | $R_s$<br>( $\text{cm}^2/\text{coul}$ ) | $\Delta(1/o)$<br>( $\Omega/\square$ ) <sup>-1</sup> | $\Delta(R_s/\rho_s^2)$<br>$\frac{\text{coul-cm}^2}{(\text{V-sec})^2}$ | $\mu_i$<br>( $\text{cm}^2/\text{V-sec}$ ) | $n_i$<br>( $\text{cm}^{-3}$ ) |
|----------------------------------|--|---|---|---|-------------------------------|
| 295                              | 2.20E4                                 | 1.60E-3   | 1.36E-2   | 85  | 5.9E20                        |
| 560                              | 7.50E4                                 |   |   |   |                               |
| 295                              | 2.20E4                                 | 1.67E-3   | 2.99E-2   | 18  | 2.9E20                        |
| 580                              | 7.50E4                                 |   |   |   |                               |
| 295                              | 2.20E4                                 | 1.69E-3   | 3.73E-2   | 22  | 2.4E20                        |
| 590                              | 7.50E4                                 |   |   |   |                               |
| 295                              | 2.20E4                                 | 1.72E-3   | 4.47E-2   | 25  | 2.0E20                        |
| 600                              | 7.50E4                                 |   |   |   |                               |

considered valid when the maximum sample current through the implanted layer is less than fifty times the leakage current.

While the differential Hall effect method is extremely sensitive to the value of sheet resistivity, it is not strongly affected by the thickness of the layer removed. Layer thickness does not enter into the calculation of average mobility of Eq. (5.4), and enters inversely into the calculation of carrier concentration from Eq. (5.5). On the other hand, layer thickness enters directly into the depth calibration. In this study, etching was performed for  $30 \pm 2$  seconds/step, giving a minimum 7% variation in the uniformity of the etch step, disregarding other factors possibly affecting the etch rate, such as residual damage or carrier concentration dependence of the etch. Thus, in the construction of the profiles presented in this chapter, the 7% uncertainty in carrier concentration due to the uncertainty in layer uniformity was accepted rather than trying to estimate "smoothed" values of resistivity or Hall coefficient; errors in smoothing these values would lead to disproportionately larger errors in carrier concentration or mobility. The carrier concentration and mobility profiles represent the overlay of from three to five measurements on identical samples with the range of values obtained listed as the uncertainty in the measurements.

## 6. DISCUSSION AND CONCLUSIONS

It is well understood that when bare silicon surfaces are implanted with arsenic to doses greater than  $10^{14} \text{ cm}^{-2}$ , an amorphous region is formed at the sample surface due to the extensive damage created by the energetic arsenic ions [27]. For annealing temperatures greater than  $550^\circ\text{C}$ , this amorphous layer regrows epitaxially on the undamaged substrate [72]. For peak arsenic concentrations less than approximately  $2.0 \times 10^{20} \text{ cm}^{-3}$ , all the implanted arsenic ions become electrically active [72], as is seen in this study. Implantations with higher peak arsenic concentrations result in incomplete electrical activation, the extent of which depends on the annealing time and temperature used [59]. This incomplete activation is mainly due to the formation of electrically-inactive arsenic clusters for high dopant concentrations, also observed in silicon grown with high arsenic content [74]. The percent activation is improved with higher annealing temperatures, due to the lowering of the peak arsenic concentration due to diffusion. Support for this interpretation is provided by the electrical results for the bare surface implants reported here (Chapter 5). The  $600^\circ\text{C}$  anneal of the  $5 \times 10^{15} \text{ cm}^{-2}$  bare surface (Fig. 5.5) results in the lowest percentage activation at the peak of the arsenic concentration, while the regions of the profile with impurity concentrations below approximately  $1.5 \times 10^{20} \text{ cm}^{-3}$  show complete electrical activation within the experimental uncertainty. As the annealing temperature approaches  $1000^\circ\text{C}$ , the profile has spread such that most of the impurity concentration is less than  $2 \times 10^{20} \text{ cm}^{-3}$  (Fig. 5.6) and the sample shows 90 to 95% electrical activation.



Consistent with this interpretation, the activation of the  $5 \times 10^{15} \text{ cm}^{-2}$  bare surface implanted sample after recrystallization is constant for annealing times up to 150 minutes (Section 5.2). This correlates well with the fact that measurable arsenic diffusion has not been observed for  $600^\circ\text{C}$  annealing [1].

From these results a commonly accepted view of high dose ( $> 10^{14} \text{ cm}^{-2}$ )  $\text{As}^+$  implantations into bare surfaces has been proposed. According to this model, the implantation creates an amorphous layer on top of an essentially undamaged substrate. This layer regrows during annealing resulting in arsenic activation similar to that observed in arsenic-doped silicon boules. Thus it is suggested that the epitaxial regrowth of bare surface implanted amorphous samples is a simple example of an amorphous-to-crystalline phase transformation [75]. Channeling effect measurements on bare surface implanted samples indicate a linear regrowth rate and a well defined activation energy [75]. Both the quality of the regrown layer and the regrowth rate are functions of substrate orientation [6,76], with the most disorder seen for  $\langle 111 \rangle$ -oriented substrates [6] with damage consisting of extensive dislocation networks permeating the implanted volume, together with isolated dislocation loops [7]. Residual damage in  $\langle 100 \rangle$ -oriented substrates, such as those used in Chapter 5, is considerably lower [6].

When silicon samples are implanted through an oxide layer, the results of annealing differ significantly from that of the bare surface implant. Well-annealed high-dose through-oxide arsenic implanted samples are characterized by stable high defect density networks [4], and diffraction patterns reveal the through-oxide implanted surface layer to be essentially polycrystalline in nature.

An interesting result from the earlier studies of this problem [4,6,7] was the fact that implantation of oxygen and arsenic into bare silicon surfaces yields exactly the same type of disorder seen for the through-oxide arsenic implanted silicon. The role of oxygen in the recovery of radiation-damaged silicon has been extensively studied. Oxygen is known to interact strongly with irradiation-induced defects in silicon such as the lattice vacancy (forming the A-center [77]), and the As-vacancy complex (the E center) [8]. In fact, it is the presence of an oxygen related defect in the recombination spectrum from irradiated silicon that allowed the identification of the oxygen recoil in through-oxide arsenic implanted substrates (Chapter 2). With oxygen impurities already established as an important factor in the recovery of irradiated silicon, it became important to determine whether or not the presence of arsenic was crucial to the formation of the residual defect structure. If arsenic were involved in defect complexes responsible for the formation of the residual defects, it would not show the electrical activation seen from silicon free from the residual defects. However, the measurements of the electrically-active impurity profiles following 1000°C annealing (Figs. 5.6 and 5.8) show arsenic activation for the through-oxide implanted sample equal to that seen from the bare surface implanted samples. We must therefore conclude it is the presence of the excess (recoil-implanted) oxygen that is responsible for residual defect formation.

To understand the role of oxygen in the formation of residual defects, it is necessary to examine the behavior of oxygen in undamaged silicon. Oxygen is an impurity commonly found in Czochralski-grown Si [47]. The

solubility of oxygen in silicon is approximately  $2 \times 10^{18} \text{ cm}^{-3}$  at the growth temperature [78]. This solubility decreases with decreasing temperature until it reaches a value of approximately  $2 \times 10^{17} \text{ cm}^{-3}$  at  $1000^\circ\text{C}$  [78]. During subsequent heatings, the oxygen in solution may be larger than the equilibrium value at that temperature; if sufficient thermal energy is present, the excess oxygen will then precipitate out of solution. This precipitation can occur in the form of  $\text{SiO}_2$  precipitates [79], which would cause dislocations in the silicon substrate due to differences in physical properties of the precipitates from those of the surrounding silicon matrix [78]. Thus a possible cause of the residual damage would be the precipitation of the excess oxygen. Furthermore, the presence of  $\text{SiO}_2$  precipitates would interrupt the orderly regrowth of the crystalline silicon from an amorphous layer, and could even serve as nucleation sites for the microcrystals. This hypothesis is clearly consistent with the fact that both transmission electron microscopy and diffraction patterns indicate that the recrystallized through-oxide implanted layer is essentially polycrystalline, consisting of a collection of microcrystals randomly oriented [4,7].

The essentially polycrystalline nature of the through-oxide implanted layer suggested that the presence of the excess oxygen affects the regrowth rate of the amorphous layer. This aspect of the problem was recently examined by Kennedy *et al.* using the technique of helium ion backscattering [80]. They found that the regrowth rate of amorphous silicon decreases exponentially with increasing oxygen concentration, thus suggesting a slight modification in the interpretation of the recovery of silicon driven amorphous by ion implantation. Instead of a simple amorphous-to-crystalline phase transition,

epitaxial regrowth of an implanted layer occurs in competition with homogeneous nucleation of the implanted layer (i.e. the formation of randomly-oriented silicon crystals at random locations in the amorphous layer). For bare surface implanted samples, epitaxial regrowth apparently predominates. Significantly, the substrate orientation with the lowest regrowth rate, i.e. the  $\langle 111 \rangle$  direction [76], also shows the greater residual disorder after annealing of bare surface implanted samples [5]. For samples implanted through thin oxide layers, the epitaxial regrowth is slowed by the presence of the recoil-implanted oxygen, and thus homogeneous nucleation predominates. Significantly, the residual damage seen following implantation through oxide layers is greatest for  $\langle 111 \rangle$ -oriented substrates which also have the slowest regrowth rates for bare surface implants. Unfortunately, it is not clear from these measurements whether it is the presence of  $\text{SiO}_2$  precipitates that retards the epitaxial regrowth or whether the excess oxygen slows the epitaxial regrowth rate for other, unknown reasons. Nevertheless, the fact that recoil implanted oxygen does indeed reduce the epitaxial growth rate is unambiguous.

The hypothesis that the residual damage is caused by the slowing of the epitaxial regrowth rate by recoil implanted oxygen leads to predictions that are verified by the electrical measurements of Chapter 5. If arsenic is not involved in the defect formation, it should show an electrical activation in the through-oxide implanted layers equivalent to that seen for bare surface implants, since the activation of arsenic does not depend on the physical dimensions of the crystal but rather on the concentration of arsenic inside



a unit volume. Additionally, grain boundary scattering of carriers is unobservable in silicon except for very pure crystals at very low temperatures [66,81]. For samples doped to the high concentrations used in this study, scattering by ionized impurities dominates the carrier transport properties of the crystal. Thus, if the extent of the residual damage were a large number of grain boundaries, the carrier mobilities would be determined by the carrier concentration and thus would yield mobility profiles identical to those expected from bulk silicon. The experimentally-determined arsenic activation and the mobility profiles are exactly what one would expect by assuming that the residual damage is caused by random nucleation during the recrystallization of the amorphous layer. When combined with the channeling measurements of the epitaxial regrowth rate of the through-oxide implanted samples, the results of this study lead to a clear and consistent interpretation of the cause of residual damage in through-oxide implanted silicon. Additionally, this study provides the first complete measurement of the effect of residual damage on the electrical properties of through-oxide implanted layers. From these measurements it is seen that the vast crystallographic damage created upon the annealing of through-oxide implanted silicon has no measurable effect on either the activation of the implanted arsenic or the carrier mobilities in the implanted layer.

Thus, while this study has helped to resolve some of the basic difficulties in understanding the residual damage caused by through-oxide arsenic implantations, other questions remain unanswered. For example, while grain boundaries and dislocations have little effect on carrier mobility,

they do have a strong effect on minority carrier lifetimes [82,83].

When these dislocations occur at p-n junction boundaries, they serve as carrier recombination centers under forward bias and carrier generation centers under reverse bias [3], thus increasing reverse leakage. Additionally, it is known that metallic impurities tend to precipitate at dislocations [84,85]. Such precipitates would also increase reverse leakage for p-n junctions. Increased junction leakage would decrease solar cell efficiency, reduce the performance of charge coupled devices, and lower the current gain of bipolar transistors. Since photoluminescence depends strongly on minority carrier lifetime, the lack of photoluminescence for anneals above 600°C tends to indicate that minority carrier lifetimes have not completely recovered even following 1000°C annealing; however, these results should be supplemented by other lifetime measurements.

Because dislocations can have a very strong effect on minority carrier lifetimes, it would be of extreme interest to examine by transmission electron microscopy whether the crystallographic defects caused by annealing high-dose through-oxide implanted samples propagate into the substrate following redistribution by thermal oxidation or whether this defect layer is consumed during the oxidation.

Finally, the above interpretation is dependent on the amorphization of the surface layer. Thus it would be useful to examine junction leakage properties, minority carrier lifetimes, and crystallographic features for through-oxide implanted samples when the total implanted dose does not drive the substrate amorphous.



For these reasons, the following experiments should be performed:

1. A study should be made of the reverse leakage for arsenic-implanted diodes. Results for diodes defined by nearly-vertical openings in the thick  $\text{SiO}_2$  mask should be compared with the results from diodes defined by openings with tapering edges which would allow recoil oxygen implantation at the junction perimeter.
2. Measurements should be made of the minority carrier lifetime for the  $5 \times 10^{15} \text{ cm}^{-2}$  As implants both into bare surface and through  $\text{SiO}_2$  to determine the effect of residual damage on the carrier lifetimes in these layers.
3. Should either of the above experiments indicate a significant difference in the device properties of the recoil-implanted layer, that experiment should be repeated for identical through-oxide implanted samples which had been first subjected to careful gettering to remove metallic impurities before implantation. This last experiment would indicate whether the residual damage in itself was responsible for the decline in device properties, or whether the residual damage was gettering metallic impurities responsible for the decline in device properties.
4. Examinations of the bare surface and through-oxide implanted samples which had been subjected to redistribution by thermal oxidation should be performed by electron diffraction and by transmission electron microscopy to determine whether or not the residual damage propagates during oxide growth.

5. Examinations should also be performed by transmission electron microscopy and by electron diffraction for well-annealed samples that had been implanted through thin oxide layers to fluences above and below the amorphous limit to determine if the sample must be driven amorphous for the residual damage to occur.

In conclusion, the present work has addressed itself to the origin and effects of residual damage in silicon seen following through-oxide arsenic implantation. After firmly establishing the oxygen dependence of one of the luminescence peaks seen from implanted silicon, we have used this luminescence to detect the presence of recoil-implanted oxygen in the silicon substrate. Electrical measurements were performed which showed electrical activation and carrier mobility identical to that seen from bare surface implanted silicon. These measurements were then found to be consistent with the interpretation that the residual damage is caused by reduction in the growth rate of amorphous silicon, favoring the process of homogeneous nucleation due to the presence of the excess recoil implanted oxygen.

## REFERENCES

1. D. H. Lee and J. W. Mayer, "Ion implanted semiconductor devices," Proc. IEEE, vol. 62, pp. 1241-55, 1974.
2. J. Sansbury, "Applications of ion implantation to semiconductor processing," Solid State Technology, pp. 31-43, November 1976.
3. A. S. Grove, Physics and Technology of Semiconductor Devices, New York: Wiley, 1967.
4. T. R. Cass and V. G. K. Reddi, "Anomalous residual damage in silicon after annealing of 'through-oxide' arsenic implantation," Appl. Phys. Lett., vol. 23, pp. 268-70, 1973.
5. W. K. Chu, H. Müller, J. W. Mayer, and T. W. Sigmon, "Residual damage in silicon from oxygen recoils in annealed 'through-oxide' arsenic implants," Appl. Phys. Lett., vol. 25, pp. 297-99, 1974.
6. H. Müller, W. K. Chu, J. Gyulai, J. W. Mayer, T. W. Sigmon, and T. R. Cass, "Crystal orientation dependence of residual disorder in arsenic implanted silicon," Appl. Phys. Lett., vol. 26, pp. 292-4, 1976.
7. R. A. Moline and A. G. Cullis, "Residual defects in silicon produced by recoil implantation of oxygen," Appl. Phys. Lett., vol. 26, pp. 551-3, 1976.
8. A. O. Ewvaraye, "The role of oxygen in irradiated arsenic-doped silicon," Appl. Phys. Lett., vol. 29, pp. 476-8, 1976.
9. P. Sigmund, "Collision theory of displacement damage," Rev. Roum. Phys. vol. 17, pp. 823-70, 969-1000, and 1070-1106, 1972.
10. J. Lindhard, M. Scharff, and H. E. Schiøtt, "Range concepts and heavy ion ranges," Matt. Fys. Medd. Dan. Vid. Selsk., vol. 33, pp. 1-39, 1963.
11. H. Goldstein, Classical Mechanics, New York: Addison-Wesley, 1963.
12. D. Landau and E. M. Lifshitz, Mechanics, New York: Addison-Wesley, 1960.
13. B. Fastrup, G. Herman, and K. J. Smith, "Measurement of inelastic energy loss in atomic collisions of  $\text{Al}^+$ ,  $\text{P}^+$ ,  $\text{S}^+$ ,  $\text{Cl}^+$ ,  $\text{Ar}^+$ ,  $\text{K}^+$ , and  $\text{Mn}^+$  on argon at keV energies and large scattering angles," Phys. Rev. A, vol. 3, pp. 1591-1617, 1971.
14. C. Lehman and G. Liebfried, "Higher order momentum approximation in classical collision theory," Z. Phys. vol. 172, pp. 465-487.

15. H. A. Bethe and R. W. Jackiw, Intermediate Quantum Mechanics, Second Edition, New York: Benjamin, 1968.
16. H. Gombas, "Statistische Behandlung des Atoms," in Encyclopedia of Physics, (S. Flugge, ed.) vol. 36, pp. 109-231, Berlin: Springer-Verlag, 1956.
17. R. P. Marchi and F. T. Smith, "Theory of elastic differential scattering in low-energy  $\text{He}^+ + \text{He}$  collisions," Phys. Rev., vol. A139, pp. 1025-1038, 1965.
18. O. B. Firsov, "A qualitative interpretation of the mean electron excitation in atomic collisions," Sov. Phys. JETP, vol. 36, pp. 1517-1523, 1959.
19. J. F. Gibbons, W. S. Johnson, and S. W. Mylroie, Projected Range Statistics - Semiconductors and Related Materials, 2nd edition, Stroudsburg: Dowden, Hutchinson and Ross, 1975.
20. K. B. Winterbon, " $Z_1$  Oscillations in stopping of atomic particles," Can. J. Phys., vol. 46, pp. 2429-2433, 1968.
21. F. Eisen, "Channeling of medium-mass ions through silicon," Can. J. Phys., vol. 46, pp. 561-572, 1965.
22. H. B. Dietrich and L. E. Plew, " $^{19}\text{F}$  range-energy curve in Si from 100 to 550 keV," Appl. Phys. Lett., vol. 29, pp. 406-408, 1976.
23. D. K. Brice, "Recoil contributions to ion-implanted energy-deposition distributions," J. Appl. Phys., vol. 46, pp. 3385-3394, 1975.
24. J. F. Gibbons, "Ion implantation in semiconductors - Part I: range distribution theory and experiments," Proc. IEEE, vol. 56, pp. 215-319, 1976.
25. G. T. Marcyk and B. G. Streetman, "Boron impurity profile tailoring in Si by ion implantation and measurement by glow discharge optical spectroscopy," J. Electrochem. Soc., vol. 123, pp. 1388-1391, 1976.
26. R. S. Nelson and M. W. Thompson, "The penetration of energetic ions through the open channels in a crystal lattice," Phil. Mag., vol. 8, p. 1667, 1963.
27. J. W. Mayer, L. Eriksson and J. A. Davies, Ion Implantation in Semiconductors, Silicon and Germanium, New York: Academic Press, 1970.
28. P. Blood, G. Dearnaly and M. A. Wilkins, "The origin of nongaussian profiles in phosphorus implanted silicon," J. Appl. Phys., vol. 45, pp. 5123-5128, 1974.



29. B. G. Streetman, Solid State Electronic Devices, New Jersey: Prentiss-Hall, 1970.
30. K. V. Vaidyanathan and G. H. Walker, "The effect of  $\text{Be}^+$  ion implanted exponential and uniform impurity profiles on the electrical characteristics of GaAs solar cells," Conference Records of the Tenth IEEE Photovoltaics Specialists Conference, Palo Alto, 1973.
31. R. A. Moline, G. W. Reutlinger, and J. C. North, "Recoil implantation of  $^{18}\text{O}$  from  $\text{SiO}_2$  by heavy projectiles," in Atomic Collisions in Solids, vol. 1, (S. Datz, B. R. Appleton, and C. D. Moak, eds.), New York: Plenum, 1976.
32. W. K. Chu, B. L. Crowder, J. W. Mayer and J. F. Ziegler, "Range distributions of implanted ions in  $\text{SiO}_2$ ,  $\text{Si}_3\text{N}_4$  and  $\text{Al}_2\text{O}_3$ ," Appl. Phys. Lett., vol. 22, pp. 490-492, 1973.
33. D. M. Smith and J. F. Gibbons "Application of the Boltzmann transport equation to the calculation of range profiles and recoil implantation in multilayered media," Fifth International Conference on Ion Implantation in Semiconductors and Other Materials, August 9-13, 1976, Boulder, Colorado, unpublished.
34. R. J. Spry and W. D. Compton, "Recombination luminescence in irradiated Si," Phys. Rev., vol. 175, pp. 1010-1020, 1968.
35. A. K. Yuknevich, "The structure of the spectrum of the radiative capture of holes by A-centers in silicon," Sov. Phys. Solid State, vol. 7, pp. 259-260, 1965.
36. C. E. Jones, E. S. Johnson, W. D. Compton, J. R. Noonan, and B. G. Streetman, "Temperature, stress, and annealing effects on the luminescence from electron-irradiated silicon," J. Appl. Phys., vol. 44, pp. 5402-5410, 1973.
37. J. R. Noonan, C. G. Kirkpatrick, and B. G. Streetman, "Photoluminescence from Si irradiated with 1.5-MeV electrons at 100°K," J. Appl. Phys. vol. 47, pp. 3010-3015, 1976.
38. J. R. Noonan, C. G. Kirkpatrick, and B. G. Streetman, "Low-temperature photoluminescence from boron implanted Si," Rad. Eff., vol. 21, pp. 225-228, 1974.
39. C. G. Kirkpatrick, J. R. Noonan, and B. G. Streetman, "Recombination luminescence from ion implanted silicon," Rad. Eff., vol. 30, pp. 97-106, 1976.
40. J. R. Haynes, M. Lax, and W. F. Flood, "Analysis of intrinsic recombination radiation from silicon and germanium," J. Phys. Chem. Solids, vol. 8, pp. 393-396, 1959.

41. Y. H. Lee and J. W. Corbett, "EPR studies in neutron-irradiated silicon: a negative charge state of a nonplanar five-vacancy cluster ( $V_5^-$ )," Phys. Rev. B, vol. 8, pp. 2810-2826, 1973.
42. J. R. Noonan, C. G. Kirkpatrick, and B. G. Streetman, "Aluminum and gallium impurity effects on the photoluminescence from electron-irradiated, pulled silicon," Solid State Comm., vol. 15, pp. 1055-9, 1974.
43. C. G. Kirkpatrick, thesis (University of Illinois, 1974), unpublished. "Photoluminescence from ion-implanted silicon," CSL report R-662, available from Defense Doc. Center TISIA, Alexandria, Va. 22314 (unpublished).
44. C. E. Jones and W. D. Compton, "Recombination luminescence in irradiated silicon - effects of uniaxial stress and temperature variation," Rad. Eff., vol. 9, pp. 83-88, 1971.
45. H. J. Stein, "Defects in silicon: Concepts and correlations," in Radiation Effects in Semiconductors, Albany 1970, ed. J. W. Corbett and G. D. Watkins, London: Gordon and Breach, 1971, pp. 125-140.
46. B. Pajot, "Improvement in the detection of oxygen in silicon by infra-red absorption," Solid State Electronics, vol. 12, pp. 923-25, 1969.
47. A. Goetzberger, D. J. Bartelink, J. P. McVittie, and J. F. Gibbons, "MOS measurement of oxygen recoils from As implantations into  $SiO_2$ ," Appl. Phys. Lett., vol. 29, pp. 259-61, 1976.
48. J. M. Morabito, "Selected area and in-depth Auger analysis of thin films," Thin Solid Films, vol. 19, pp. 21-41, 1973.
49. J. E. Greene and J. M. Whelan, "Glow discharge optical spectroscopy for the analysis of thin films," J. Appl. Phys., vol. 44, pp. 2509-2513, 1973.
50. H. Liebl, "Ion probe microanalysis," J. Phys. E., vol. 8, pp. 797-809, 1975.
51. C. A. Evans, Jr., "Surface and thin film compositional analysis: description and comparison of techniques," Analyt. Chem., vol. 47, pp. 818A-829A, 1975.
52. E. H. S. Burhop, The Auger Effect and Other Radiationless Transitions, New York: Cambridge University Press, 1952.
53. C. A. Evans, Jr., "Surface and thin film analysis," Analyt. Chem., vol. 47, pp. 855A-866A, 1975.
54. A. Von Engel, Ionized Cases, second edition, Oxford, London, 1965.



55. J. Comas and C. G. Burleigh, "Mass-spectrometric study of sputtering of single crystals of GaAs by low energy Ar ions," J. Appl. Phys., vol. 38, pp. 2956-2960, 1967.
56. C. A. Evans, Jr. Private communication.
57. J. W. Coburn, "Sputtering in the surface analysis of solids: a discussion of some problems," J. Vac. Sci. Technology, vol. 13, pp. 1037-1044, 1976.
58. G. T. Marcyk, thesis (University of Illinois, 1976), unpublished. "Glow Discharge Optical Spectroscopy for Measurement of Boron Implanted Distributions in Silicon," CSL report R-720, available from Defense Doc. Center TISIA, Alexandria, VA 22314 (unpublished).
59. R. B. Fair and J. C. C. Tasi, "The diffusion of ion-implanted arsenic in silicon," J. Electrochem. Soc., vol. 122, pp. 1689-1696, 1975.
60. W. Kern and D. A. Pontinen, "Cleaning solutions based on hydrogen peroxide for use in silicon semiconductor technology," RCA Review, vol. 31, pp. 187-206, 1970.
61. L. J. Van der Pauw, "A method of measuring specific resistivity and Hall effect of discs of arbitrary shapes," Phillips Res. Reports, vol. 13, pp. 1-9, 1958.
62. M. Hansen and A. Anderko, Constitution of Binary Alloys, New York: McGraw-Hill, 1958.
63. R. Chwang, B. J. Smith, and C. R. Crowell, "Contact size effects in the van der Pauw method for resistivity and Hall coefficient measurement," Solid State Electronics, vol. 17, pp. 1217-27, 1974.
64. W. McLevige, P. K. Chatterjee, and B. G. Streetman, "Versatile double-ac system for profiling impurities in semiconductors," to be published in J. Phys. E.
65. R. L. Petritz, "Theory of an experiment for measuring the mobility and density of carriers in the space-charge region of a semiconductor surface," Phys. Rev., vol. 110, pp. 1254-62, 1958.
66. V. I. Fistul', Heavily Doped Semiconductors, New York: Plenum, 1969.
67. P. W. Chapman, O. N. Tufte, J. D. Zook, and D. Long, "Electrical properties of heavily doped silicon," J. Appl. Phys., vol. 34, pp. 3291-95, 1963.
68. S. Watelski of Texas Instruments, Private communication.

69. S. K. Ghandi, The Theory and Practice of Microelectronics, New York: Wiley, 1968.
70. A. B. Phillips, Transistor Engineering, New York: McGraw-Hill, 1962.
71. G. Nakamura and Y. Yukimoto, "Anomalous annealing behavior of secondary defects in silicon implanted with arsenic ions through a dielectric layer," Proceedings of the Fifth International Conference on Ion Implantation in Semiconductors and Other Materials, August 9-13, 1976, Boulder, Colorado, unpublished.
72. B. L. Crowder, "The influence of the amorphous phase in ion distributions and annealing behavior of Group III and Group V ions implanted into silicon," J. Electrochem. Soc., vol. 118, pp. 943-8, 1971.
73. M. Tamura, N. Yoshino, and T. Ikeda, "Tertiary defects in phosphorous implanted silicon," Appl. Phys. Lett., vol. 27, pp. 427-9, 1975.
74. S. M. Hu, "Diffusion in silicon and germanium," in Atomic Diffusion in Semiconductors, D. Shaw, ed., New York: Plenum, 1973, pp. 217-350.
75. L. Cspregi, J. W. Mayer, and T. W. Sigmon, "Channeling effect measurements of the recrystallization of amorphous Si on crystal Si," Phys. Lett. vol. 54A, pp. 157-8, 1975.
76. L. Cspregi, J. W. Mayer, and T. W. Sigmon, "Regrowth behavior of ion-implanted amorphous layers on  $\langle 111 \rangle$  Si," Appl. Phys. Lett., vol. 29, pp. 94-5, 1976.
77. G. D. Watkins and J. W. Corbett, "Defects in irradiated silicon, I. Electron spin resonance of the Si-A center," Phys. Rev., vol. 121, pp. 1001-14, 1961.
78. W. I. Patrick, "The precipitation of oxygen in silicon and its effect on surface perfection," in Silicon Device Processing, C. P. Marsden, ed. National Bureau of Standards Special Publication 327, 1970.
79. R. Bullough and R. C. Newman, "The interaction of impurities with dislocations in silicon and germanium," in Progress in Semiconductors, vol. 7, Gibson and Burgess, eds. London: Heywood & Co. Ltd., 1963.
80. E. F. Kennedy, L. Cspregi, J. W. Mayer, and T. W. Sigmon, "Dependence of residual damage in 'through-oxide' implants on substrate orientation and anneal sequence," Proceedings of the Fifth International Conference on Ion Implantation in Semiconductors and Other Materials, August 9-13, 1976, Boulder, Colorado, unpublished.
81. P. Aigrain, Electronic Processes in Solids, Cambridge: MIT Press, 1960.

82. A. D. Kurtz, S. A. Kulin, and B. L. Averbach, "Effect of dislocations on minority carrier lifetimes in semiconductors," Phys. Rev., vol. 106, pp. 910-7, 1956.
83. G. Bemski, "Recombination in semiconductors," Proc. IRE, vol. 46, pp. 990-1004, 1958.
84. W. C. Dash, "Birefringence in silicon," Phys. Rev., vol. 98A, p. 1536, 1955.
85. T. E. Seidel, R. L. Meek, and A. G. Cullis, "Direct comparison of ion-damage gettering and phosphorus diffusion gettering of gold in silicon," J. Appl. Phys., vol. 46, pp. 600-9, 1975.

APPENDIX: Evaluation of Carrier Concentrations  
and Mobilities through Differential  
Hall Effect Measurements

To obtain the formulas by which we convert sheet resistivity and sheet Hall coefficient data into carrier concentration and mobility, we begin by considering a structure composed of two distinct layers, each of which is assumed to have uniform carrier concentration and mobility (Figure A1). The surface layer of thickness  $d_1$  has conductivity  $\sigma_1$  and Hall coefficient  $R_{H2}$ . The application of a voltage across the length  $L$  of this structure will produce currents  $I_1$  and  $I_2$  in the respective layers, which will depend on the conductivities and thicknesses of each layer. If a magnetic field  $B$  is now applied perpendicular to the sample, each layer will develop its own Hall voltage, which combine to produce a Hall voltage for the entire sample. This resultant Hall voltage can be determined by examining the equivalent circuit of Figure A1. Here  $G$  represents the conductance of each layer in the direction parallel to the contacts

$$G_1 = \sigma_1 \frac{Ld_1}{w} \quad G_2 = \sigma_2 \frac{Ld_2}{w} \quad (A1)$$

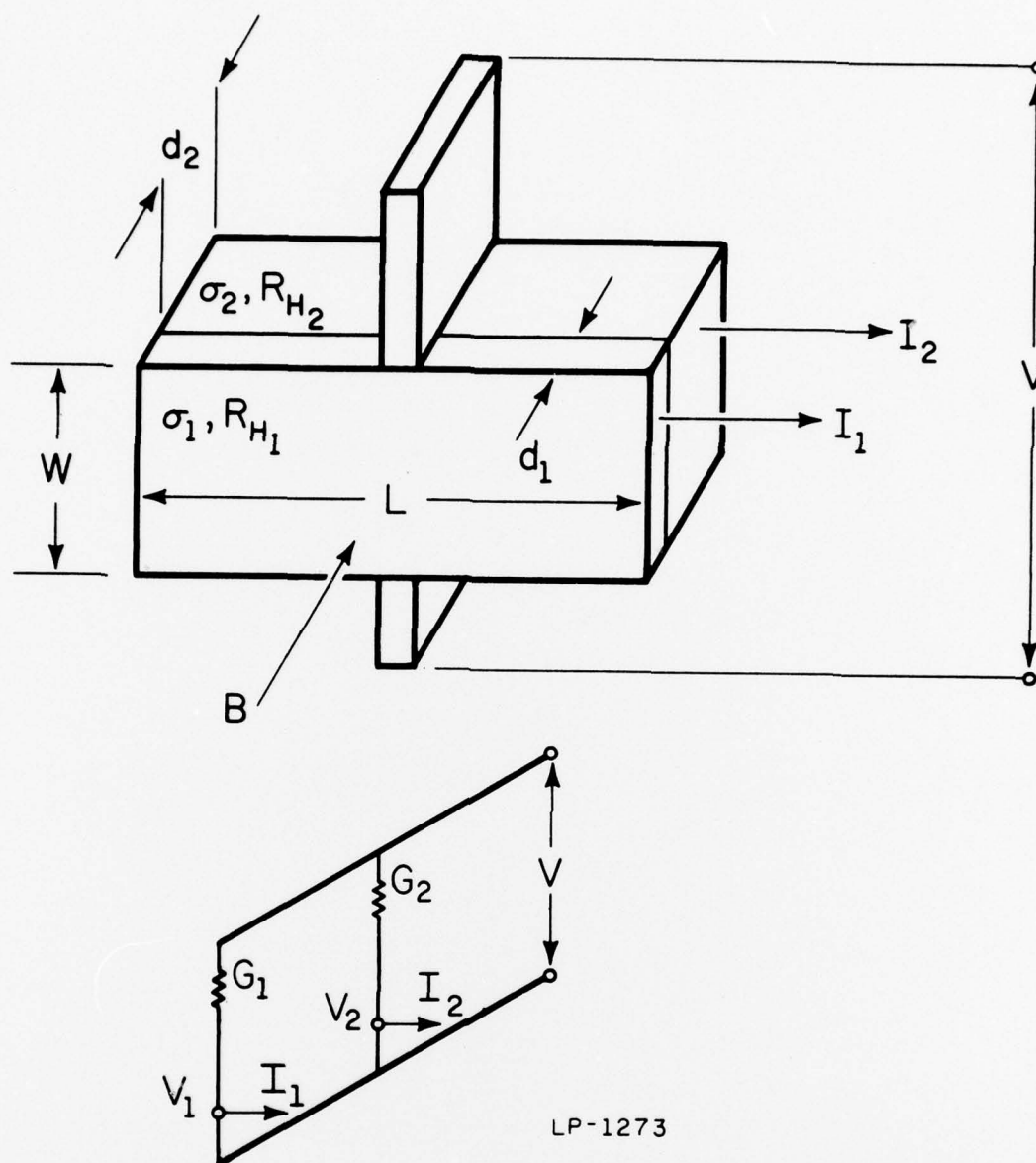
From Kirchoff's laws, the equivalent voltage  $V$  seen at the contacts is then given by

$$V = \frac{V_1 G_1 + V_2 G_2}{G_1 + G_2} \quad (A2)$$

where the Hall voltages are given by

$$V_1 = \frac{I_1 R_{H1} B}{d_1} \quad V_2 = \frac{I_2 R_{H2} B}{d_2} \quad (A3)$$





LP-1273

Figure A.1. Top: Hypothetical two-layer structure used to determine sheet resistivity and sheet Hall coefficient for composite sample.

Bottom: Equivalent circuit used to determine Hall voltage for two-layer structure shown above.

From examining the resistance of each layer in the direction of current flow we see

$$I_1 = \frac{I \frac{L}{\sigma_2 d_2 w}}{\frac{L}{\sigma_1 d_1 w} + \frac{L}{\sigma_2 d_2 w}} = \frac{\sigma_1 d_1 I}{\sigma_1 d_1 + \sigma_2 d_2} \quad (A4)$$

and similarly

$$I_2 = \frac{\sigma_2 d_2 I}{\sigma_1 d_1 + \sigma_2 d_2} \quad (A5)$$

with total sample current  $I$  given by

$$I = I_1 + I_2 \quad (A6)$$

We now define the effective Hall coefficient  $R_H$  for the entire sample according to the form of equation A3:

$$V = \frac{I R_H B}{d} \quad (A7)$$

with  $d = d_1 + d_2$ .

Equating (A2) and (A7) and substituting (A1) and (A3), we obtain

$$\frac{I R_H B}{d} = \frac{\frac{I_1 R_{H1} B}{d} \cdot \frac{\sigma_1 L d_1}{w} + \frac{I_2 R_{H2} B}{d_2} \frac{\sigma_2 L d_2}{w}}{\frac{\sigma_1 L d_1}{w} + \frac{\sigma_2 L d_2}{w}} \quad (A8)$$

Substitution of (A4) and (A5) into (A8) now yields

$$\frac{I B}{d} R_H = \frac{I B \left[ \frac{\sigma_1 d_1 R_{H1} \sigma_1}{\sigma_1 d_1 + \sigma_2 d_2} + \frac{\sigma_2 d_2 R_{H2} \sigma_2}{\sigma_1 d_1 + \sigma_2 d_2} \right]}{\sigma_1 d_1 + \sigma_2 d_2} \quad (A9)$$



$$R_H = d \left[ \frac{\sigma_1^2 d_1 R_{H1} + \sigma_2^2 d_2 R_{H2}}{(\sigma_1 d_1 + \sigma_2 d_2)^2} \right] \quad (A10)$$

Since layers one and two are in parallel in the direction of current flow their conductivities add to give the conductivity of the entire sample

$$\frac{\sigma d L}{w} = \frac{\sigma_1 d_1 L}{w} + \frac{\sigma_2 d_2 L}{w} \quad (A11)$$

or

$$\sigma = \frac{1}{d} (\sigma_1 d_1 + \sigma_2 d_2) \quad (A12)$$

with  $\sigma$  the conductance of the entire sample.

Generalizing the results (A10) and (A12) to a total of  $j$  independent layers, we obtain

$$R_H = \frac{d \sum_{i=1}^j R_{Hi} \sigma_i^2 d_i}{\left( \sum_{i=1}^j \sigma_i d_i \right)^2} \quad (A13)$$

and

$$\sigma = \frac{1}{d} \sum_{i=1}^j \sigma_i d_i \quad (A14)$$

If we now assume that the Hall mobility  $\mu_H$  is equal to the conductivity mobility  $\mu$  and also assume that the currents in each layer are carried by majority carriers only, we then have

$$\sigma_i = n_i q \mu_i \quad \text{and} \quad R_{Hi} = \frac{1}{n_i q} \quad (A15)$$

so that

$$\sigma = \frac{1}{d} \sum_{i=1}^j n_i q \mu_i d_i \quad \text{and} \quad R_H = d \frac{\left[ \sum_{i=1}^j n_i q \mu_i^2 d_i \right]}{\left( \sum_{i=1}^j n_i q \mu_i d_i \right)^2} \quad (\text{A16})$$

with  $q$  equal to the electronic charge ( $1.602 \times 10^{-16}$  coul). The sheet resistivity  $\rho_{s_j}$  for our structure of  $j$  layers is defined by

$$\rho_{s_j} = (\sigma d)^{-1} = \left( \sum_{i=1}^j n_i q \mu_i \right)^{-1} \quad (\text{A17})$$

and the sheet Hall coefficient for our structure of  $j$  layers is

$$R_{s_j} = \frac{R_H}{d} = \frac{\sum_{i=1}^j n_i q \mu_i^2 d_i}{\left( \sum_{i=1}^j n_i q \mu_i d_i \right)^2} \quad (\text{A18})$$

By examining the forms of the above expressions we can see that

$$\frac{R_{s_j}}{\rho_{s_j}^2} = \left[ \frac{\sum_{i=1}^j n_i q \mu_i^2 d_i}{\left( \sum_{i=1}^j n_i q \mu_i d_i \right)^2} \right] \left[ \frac{1}{\left( \sum_{i=1}^j n_i q \mu_i d_i \right)^{-1}} \right]^2 \quad (\text{A19})$$

and

$$\frac{1}{\rho_{s_j}} = \sum_{i=1}^j n_i q \mu_i d_i \quad (\text{A20})$$

From the last two expressions we see that if we measure both the sheet resistivity and sheet Hall coefficient for our structure consisting of  $j$  hypothetically distinct layers and then remove one layer, our structure will

now consist of  $j-1$  layers and have sheet resistivities and sheet Hall coefficients given by

$$\rho_{s_{j-1}} = \frac{j}{\sum_{i=1}^j n_i q \mu_i d_i} \quad (A21)$$

$$R_{s_{j-1}} = \frac{\sum_{i=1}^{j-1} n_i q \mu_i^2 d_i}{\left( \sum_{i=1}^{j-1} n_i q \mu_i d_i \right)^2} \quad (A22)$$

so that the changes in the quantities defined in (A19) and (A20) will become

$$\Delta(R_s / \rho_s^2)_j \equiv \frac{R_{s_j}}{\rho_{s_j}^2} - \frac{R_{s_{j-1}}}{\rho_{s_{j-1}}^2} = \frac{j}{\sum_{i=1}^j n_i q \mu_i^2 d_i} - \frac{j}{\sum_{i=1}^j n_i q \mu_i^2 d_i} = n_j q \mu_j^2 d_j \quad (A23)$$

and

$$\Delta(1/\rho_s)_j \equiv \frac{1}{\rho_{s_j}} - \frac{1}{\rho_{s_{j-1}}} = \frac{j}{\sum_{i=1}^j n_i q \mu_i d_i} - \frac{j-1}{\sum_{i=1}^{j-1} n_i q \mu_i d_i} = n_j q \mu_j d_j \quad (A24)$$

Thus, we obtain the desired results by considering dividing (A23) by (A24) and then using this result in (A24)

$$\mu_j = \frac{\Delta(R_s / \rho_s^2)_j}{\Delta(1/\rho)_j} \quad (A25)$$

and

$$n_j = \frac{\Delta(1/\rho_s)_j}{q d \mu_j} \quad (A26)$$

## VITA

David Richard Myers was born on December 16, 1948 in Harvey, Illinois. He attended the University of Illinois at Chicago Circle, where he received a Bachelor of Science in Engineering with highest honors in June, 1971. Since September, 1971 he has been attending the University of Illinois at Urbana-Champaign. He received a Master of Science degree in Electrical Engineering in September, 1973. Mr. Myers is a member of the Institute of Electrical and Electronics Engineers, the American Physical Society, Phi Eta Sigma, Phi Kappa Phi, and Sigma Xi.